

**STUDY OF INTERACTIONS IN THE
HOFSTADTER REGIME OF THE
HONEYCOMB LATTICE**

By

**Archana Mishra
(PHYS10200904008)**

The Institute of Mathematical Sciences, Chennai

*A thesis submitted to the
Board of Studies in Physical Sciences
In partial fulfillment of requirements
For the Degree of*

DOCTOR OF PHILOSOPHY

of

HOMI BHABHA NATIONAL INSTITUTE



February, 2016

**STUDY OF INTERACTIONS IN THE
HOFSTADTER REGIME OF THE
HONEYCOMB LATTICE**

By

Archana Mishra

(PHYS10200904008)

The Institute of Mathematical Sciences, Chennai

*A thesis submitted to the
Board of Studies in Physical Sciences
In partial fulfillment of requirements
For the Degree of*

DOCTOR OF PHILOSOPHY

of

HOMI BHABHA NATIONAL INSTITUTE



February, 2016

Homi Bhabha National Institute

Recommendations of the Viva Voce Committee

As members of the Viva Voce Committee, we certify that we have read the dissertation prepared by Ms. Archana Mishra entitled “Study of interactions in the Hofstadter regime of the honeycomb lattice” and recommend that it maybe accepted as fulfilling the thesis requirement for the award of Degree of Doctor of Philosophy.

Date: _____

Chairman - Prof. Ramesh Anishetty

Date: _____

Guide/Convener - Prof. Syed R. Hassan

Date: _____

Co-guide - Prof. R. Shankar

Date: _____

Examiner - Prof. Krishnendu Sengupta

Date: _____

Member 1 - Prof. Sibasish Ghosh

Final approval and acceptance of this thesis is contingent upon the candidate's submission of the final copies of the thesis to HBNI.

We hereby certify that we have read this thesis prepared under our direction and recommend that it maybe accepted as fulfilling the thesis requirement.

Date: _____

Place: IMSc, Chennai Co-guide: Prof. R. Shankar Guide: Prof. Syed R. Hassan

STATEMENT BY AUTHOR

This dissertation has been submitted in partial fulfillment of requirements for an advanced degree at Homi Bhabha National Institute (HBNI) and is deposited in the Library to be made available to borrowers under rules of the HBNI.

Brief quotations from this dissertation are allowable without special permission, provided that accurate acknowledgement of source is made. Requests for permission for extended quotation from or reproduction of this manuscript in whole or in part may be granted by the Competent Authority of HBNI when in his or her judgment the proposed use of the material is in the interests of scholarship. In all other instances, however, permission must be obtained from the author.

Archana Mishra

DECLARATION

I, hereby declare that the investigation presented in the thesis has been carried out by me. The work is original and has not been submitted earlier as a whole or in part for a degree / diploma at this or any other Institution / University.

Archana Mishra

List of Publications arising from the thesis

Journal

1. “Topological transitions in a model with Particle-Hole symmetry, Pancharatnam-Berry Curvature and Dirac Points”, P. V. Sriluckshmy, Archana Mishra, S. R. Hassan and R. Shankar, *Physical Review B*, 2014, Vol: 89, p: 045105-1 to 045105-12.
2. “Effects of interaction in the Hofstadter regime of the honeycomb lattice”, Archana Mishra, S. R. Hassan and R. Shankar, *Physical Review B*, 2016, Vol: 93, p: 125134-1 to 125134-8.

Others

1. “Translational symmetry breaking and the disintegration of the Hofstadter butterfly”, Archana Mishra, S. R. Hassan and R. Shankar, arXiv:1605.06307[cond-mat.str-el]. *Communicated to Physical Review B*.

Archana Mishra

Details of the modifications made in the thesis

Below I summarize all the modifications I have made in my thesis “STUDY OF INTERACTIONS IN THE HOFSTADTER REGIME OF THE HONEYCOMB LATTICE” based on the referee reports and suggestions of doctoral committee.

The page numbers given below correspond to the pages of the previous version of the thesis which was sent to the referees for review.

1. Publication list has been updated.
2. In Page 14: A paragraph is added regarding topological transitions in Chern insulators and fractional Chern insulators is added after paragraph 1.
3. In Page 19, paragraph 1: ‘Interaction induced spatial … thus giving examples of interaction induced nematic phases.’ is added as suggested by referee.
4. In Page 73, Fig. 4.3 caption: ‘In this figure the colorbar is restricted to values from 7 to 7 for convenience in plotting’ is changed to ‘In this figure the colorbar is restricted to values from 8 to 8 for convenience in plotting’.
5. In Page 73, paragraph 1: ‘In this figure the colorbar is restricted to values from 7 to 7 … maximum value of q ’ is changed to ‘In this figure the colorbar is restricted to values from 8 to 8 … maximum value of q ’.
6. In Page 75, paragraph 3: ‘In this figure the colorbar is restricted to values from 7 to 7 … bands filled is 18’ is changed to ‘In this figure the colorbar is restricted to values from 8 to 8 … bands filled is 18’.
7. In Page 76, section 4.3: First paragraph is changed.
8. In Page 78, section 4.3.2, paragraph 1: ‘Here we have … interaction strength $V = 1$

... of the form $\phi = 2\pi p/q$ ' is changed to 'Here we have ... interaction strength $V = 1, 2 \dots$ of the form $\phi = 2\pi p/q$ '.

9. In Page 78, section 4.3.2, paragraph 4: ‘The plot for flux per plaquette versus the maximum energy of each band is given by Fig. 4.7a for $V = 1$ and by Fig. 4.6b for $V = 4$. As seen from Fig. 4.7a, . . .’ is changed to ‘The plot for flux per plaquette versus the maximum energy of each band is given by Fig. 4.7a for $V = 1$, Fig. 4.7c for $V = 2$ and Fig. 4.7d for $V = 4$. As seen from Fig. 4.7a and Fig. 4.7b, . . .’.
 10. In Page 80, in Fig. 4.7 energy flux plot is for $V = 1$ and $V = 2$ is added and is mentioned in the caption.
 11. In Page 80, section 4.3.3, paragraph 1: ‘Fig. 4.8a is the Landau fan diagram in the presence of interaction of strength $V = 1$ and Fig. 4.8b is the Landau fan diagram in the presence of interaction of strength $V = 4$.’ is changed to ‘Fig. 4.8a is the Landau fan diagram in the presence of interaction of strength $V = 1$, Fig. 4.8b is the Landau fan diagram in the presence of interaction of strength $V = 2$ and Fig. 4.8c is the Landau fan diagram in the presence of interaction of strength $V = 4$.’.
 12. In Page 81, Fig. 4.8 is removed.
 13. In Page 83, in Fig. 4.9 a Landau fan diagram for interaction strength $V = 2$ is added and is added in caption.

Dedicated to my parents and sister

ACKNOWLEDGEMENTS

I am highly indebted to my supervisor, Prof. S. R. Hassan and co-advisor Prof. R. Shankar, for being the source of great inspiration and motivation throughout my PhD period and giving me continuous support for my research work. I express my sincere gratitude to my advisors for being very patient and helpful whenever I had some doubts or problems in understanding. I am immensely grateful to them for giving me the full freedom to pursue my research and for being always there to help me with their ideas whenever I got stuck in my research problem. Their constant encouragement towards my research work and in general, has made my PhD period one of the best periods of my life. Their immense knowledge, ideas and their excitement and motivation towards research will always be my source of inspiration. I am thankful to my supervisor and co-advisor for providing me continuous guidance and support during my PhD period.

I would like to express my gratitude to Prof. G. Baskaran, Prof. Mukul S. Laad and Dr. R. Ganesh for all the fruitful discussions I had with them which helped me in my research.

My sincere thanks also goes to Prof. Ramesh Anishetty, Prof. Suryanarayan Nemani, Prof. Sibasish Ghosh, Prof. Rahul Sinha, Prof. Sujoy Ashok, Prof. Nita Sinha, Prof. Sanatan Digal, Prof. Ashok Mishra, Prof. Ronojoy Adhikari, Prof. Vani Vemparala Prof. Rajesh Ravindran and Prof. T. R. Govindrajan for teaching me and guiding during my course work period.

I would like to thank everybody at The Institute of Mathematical Sciences (IMSc), Chennai for providing excellent academic atmosphere and computational facilities for doing my research work peacefully. I must also thank all the academic visitors of my advisors, for sparing the time to discuss ideas and giving their insight on many topics.

I am thankful to my best friend Dr. Dibyakrupa Sahoo who has always been a great support in my life. He is always there at the right moment to help me out of any problem,

let it be Latex or general. I am also thankful to Arya S., one of my close friends in IMSc, for being very caring, encouraging and always motivating me during my period of research. Discussions with her on academics have been really fruitful. My life at IMSc was great because of these two persons who are ready to go to any extent to bring a smile on my face.

I must extend my thanks to Dr. Vinu Lukose. Though we interacted only towards the end of my PhD period but those academic discussions have enhanced my understanding on various concepts. His passion to read and know about new arenas in physics motivates me. I am thankful to Abhrajit, Rohan, Tanmay, Nirmalya, Sriluckshmy, Kamalakshya, Ravi, Subhadeep, Tanmoy, Somdeb, Rajeev for all the discussions and in making my days at IMSc pleasant and enjoyable.

I am grateful to Mr. Vishnu Prasad and all administrative staff who were always ready to help me regarding any official issues. Their expert way of handling situations has made my stay in IMSc smooth and peaceful.

Finally, I am grateful to my parents who are the source of positivity in my life. Their encouragement, faith in me and love have helped me overcome any obstacle in my path. I am thankful to my sister for being my support system and motivating me whenever I am upset. Their optimistic attitude is contagious and has helped me to smile even in the worst of my situations. I dedicate this thesis to my parents and sister.

Contents

Synopsis	xxiii
List of Figures	xxx
1 Introduction	1
1.1 Hofstadter regime	2
1.2 Hofstadter Butterfly	3
1.3 Realization of Hofstadter butterfly in physical system	5
1.3.1 Semiconductor superlattice	7
1.3.2 Graphene superlattice	7
1.3.3 Optical lattice	9
1.4 Brief Summary of past theoretical works	10
1.4.1 Quantum geometry	13
1.4.2 Topological Transitions	15
1.4.3 Nematic phases in quantum Hall systems	16
1.5 Motivation behind the research work in the thesis	17
1.6 A preview of the thesis	18
2 Review of the non-interacting model	19
2.1 Description of the non-interacting model	19
2.2 Symmetries of the system	20

2.2.1	Translational symmetry	20
2.2.2	Rotational Symmetries	22
2.2.3	Particle-hole symmetry	23
2.3	Magnetic unit cell	23
2.4	Energy spectrum	24
2.5	Topology of the bands	27
3	Effect of interactions in the Hofstadter regime of the honeycomb lattice	33
3.1	Description of the model	33
3.2	Mean Field Theory	35
3.2.1	Algorithm to solve the self consistency equations	36
3.3	$q = 3$ case	37
3.3.1	Order Parameters	38
3.3.2	Unit cell choices	39
3.4	Results and Analysis	40
3.4.1	Dirac regime: $m = 3$	41
3.4.2	van Hove filling: $m = 2$	42
3.4.3	Fermi regime: $m = 1$	49
3.5	Current on the links and flux per plaquette	49
3.6	Insight to the topological transition	52
3.7	Geometry of the ground state	54
3.7.1	Quantum metric	54
3.7.2	Pancharatnam Berry Curvature	57
4	Fractal nature of the Hofstadter Butterfly in the presence of interactions	59
4.1	Hofstadter butterfly of the non-interacting Honeycomb lattice	60
4.1.1	Energy-flux plot	60

4.1.2	Landau fan diagram	63
4.2	Non-interacting	65
4.2.1	Energy-flux diagram	65
4.2.2	Landau fan diagram	66
4.3	Hofstadter Butterfly in the presence of interactions	67
4.3.1	Hofstadter butterfly in symmetric phase	67
4.3.2	Effect of interactions on the Hofstadter butterfly	68
4.3.3	Effect of interaction on the Landau fan diagram	70
5	Signal of Pancharatnam Berry curvature: Rotating condensates	75
5.1	Probing the PB curvature	76
5.2	Kitaev Hubbard Model	78
6	Summary and Conclusion	85
Appendices		87
A	Dipole moment and Quadrupole moment under the rotational and inversion operators	89
B	Proof of relation between quantum metric and pair correlation function	93
C	Chern numbers at half filling	97
Bibliography		99

SYNOPSIS

Introduction: Two dimensional electron systems in a periodic potential in presence of magnetic field are characterized by two length scales: the periodicity of the potential and the magnetic length. Interplay between these two independent length scales leads to a self similar fractal structure in the energy spectrum vs magnetic flux plot. This structure, which is one of the first quantum fractal structures to be discovered, is called as the Hofstadter butterfly [1]. The recent experimental observations of the fractal structure in graphene superlattices [2-5] and realization of the Hofstadter Hamiltonian in optical lattice [6,7] have motivated us to study the effect of interactions in this Hofstadter system. The interactions can induce charge ordering which can break translational symmetry and lead to various complex phases. Interaction induced translational symmetry breaking phases have been studied in the honeycomb lattice in the absence of magnetic field [8]. Effects of interactions on the Hofstadter butterfly have been discussed previously [9-12]; these works do not consider translational symmetry breaking.

This thesis provides a detailed discussion on the effect of interactions in the Hofstadter regime of the honeycomb lattice. Our studies reveal various interesting phases as the strength of the interaction is increased which break the translational and rotational symmetries of the system. These phase transitions are sometimes accompanied with topological transitions. Further this thesis discusses the effect of interactions on the fractal nature of the Hofstadter butterfly. The thesis also discusses the method we proposed to detect the Berry curvature.

Effect of interactions in Hofstadter regime of the honeycomb lattice: The model we study is spinless fermions on honeycomb lattice with nearest neighbor hopping and nearest neighbor interactions in presence of magnetic field such that the flux passing

through each plaquette is $2\pi/q$ where q is an integer [13]. There are $2q$ bands in the energy spectrum. The energy bands are topologically non-trivial having non-zero Chern number [14]. In the non-interacting model, the filled energy bands can be divided into three regimes depending on the change in Hall conductivity, namely, Fermi regime, van Hove filling and Dirac regime. We introduce nearest neighbor interaction term in the Hamiltonian and solve this interacting problem using mean field approximation. We find various complex phases as the ground state as we vary the interaction strength V from $0 \leq V \leq 10$. The self consistency equations are solved for $q = 3$ where $m = 1$ is in Fermi regime, $m = 2$ is the van Hove filling and $m = 3$ is in the Dirac regime. The phases with broken rotational symmetries are classified according to the charge ordering which in turn is characterized in terms of dipole moment and quadrupole moment. We denote the phase with zero dipole moment but non-zero quadrupole moment as the nematic phase and the phase with both non-zero dipole and quadrupole moment as the ferrielectric phase. At very small interaction values, the ground state wavefunction is same as that of the non-interacting case and hence Hall conductivities for different fillings remain same as the later case. We denote this phase as the symmetric phase.

For filling $m = 3$ i.e. half filling, there is a second order Landau transition from symmetric phase to a charge density wave phase on increasing the interaction strength. In case of van Hove filling, i.e. $m = 2$, there is a first order Landau phase transition from symmetric phase to nematic phase at $V = 2.744$ where the translational and rotational symmetries of the system are broken but the inversion symmetry is still preserved. This transition is accompanied with a change in the Hall conductivity from e^2/h in symmetric phase to zero in nematic phase. Hence, there is a first order topological transition. On further increasing the interaction strength, there is another first order Landau transition at $V = 4.5$ from nematic phase to ferrielectric phase. Here along with translational and rotational symmetries, the inversion symmetry of the system is also broken. The

Hall conductivity in this phase remains zero. In case of lowest band filled, i.e. $m = 1$, there is a first order phase transition from symmetric phase to nematic phase at $V = 5.265$. This Landau transition is also accompanied with a topological transition from Hall conductivity $-e^2/h$ to zero.

Insight to the mechanism of the topological transitions accompanying the Landau transitions can be understood from the bond strength distribution for these phases which indicate that the mean field Hamiltonian resembles that of weakly coupled ribbons, namely quasi 1D systems and the coupling becomes weaker as the interaction strength is increased. In the limit of completely decoupled ribbons, Chern numbers for all the bands should be equal to zero. Thus it seems that the anisotropy of the bond order parameters drives the change of Chern numbers.

We further study the geometry of the ground state and investigate the structure of the anisotropic phases by studying pair correlations from the point of view of the quantum geometric approach to insulating states [15]. We give a relation between the pair correlation function and the quantum metric in the momentum space [15], averaged over the Brillouin zone (BZ). This result relates the momentum space quantum metric of systems in a periodic potential to the real space metric introduced by Haldane [16] in homogeneous quantum Hall systems.

Effect of interactions on the fractal structure of the Hofstadter butterfly: In this thesis, I also solve the self consistency equations for all fluxes of the form $\phi/\phi_0 = p/q$ where p, q are coprime integers and $p < q$ for $q = 3$ to 20 for filled band cases at interaction strength $V = 4$. Comparing the energies of the mean field solutions we find the ground state. In non-interacting case, the r^{th} gap in the Hofstadter butterfly spectrum is characterized by two topological invariants (t_r, s_r) which satisfy a Diophantine equation $r = pt_r + qs_r$ [17,18]. The Hall conductivity of the r^{th} gap is given by $\sigma_H = -\frac{e^2}{h}t_r$; Using the same Diophantine equation for the interacting case we find that s_r is a fraction

and hence the Diophantine equation is no more satisfied. In non-interacting case, in the Landau fan diagram, we can join the points with same Hall conductivity by a straight line which on extrapolating touches at an integer value of r/q . This value is same as s_r . But for interacting case, we cannot join the points with same Hall conductivity in a straight line. The points with same Hall conductivities are scattered. Hence, we conclude that the fractal structure of the Hofstadter butterfly is wiped out in presence of interactions.

Detecting Berry Curvature: We also propose a method to detect the Berry curvature of occupied energy bands corresponding to a lattice and hence understand the topology of the bands [19]. We propose to construct the lattice using ultracold atoms in optical lattice in a harmonic trap. Using time of flight experiment the expansion of the atomic condensate can be studied when both the harmonic trap and the potential forming the lattice is switched off. For bands with zero berry curvature, the atomic condensate will expand and take the shape of the background lattice. On the other hand, in case of bands with non-trivial topology the atomic condensate starts rotating along with expanding and taking the shape of the lattice. This is the signal of presence of Berry curvature.

Conclusion: In summary, we show that interactions can induce charge ordering translational and rotational breaking phases which can sometimes be accompanied with the change in the Hall conductivity. Thus, we show that the first order Landau transition is also accompanied with topological transition. We also study the geometry of these states. Further we look into the effect of interactions on the Hofstadter butterfly and discuss the wipe out of fractal structure as a result of it. We also propose a method to detect the Berry curvature in optical lattice system.

Bibliography

- [1] D. R. Hofstadter *Physical Review B*, vol. 14, no. 6, p. 2239, 1976.
- [2] L. Ponomarenko, R. Gorbachev, G. Yu, D. Elias, R. Jalil, A. Patel, A. Mishchenko, A. Mayorov, C. Woods, J. Wallbank, *et al. Nature*, vol. 497, no. 7451, p. 594, 2013.
- [3] C. Dean, L. Wang, P. Maher, C. Forsythe, F. Ghahari, Y. Gao, J. Katoch, M. Ishigami, P. Moon, M. Koshino, *et al. Nature*, vol. 497, no. 7451, p. 598, 2013.
- [4] B. Hunt, J. Sanchez-Yamagishi, A. Young, M. Yankowitz, B. J. LeRoy, K. Watanabe, T. Taniguchi, P. Moon, M. Koshino, P. Jarillo-Herrero, *et al. Science*, vol. 340, no. 6139, p. 1427, 2013.
- [5] G. Yu, R. Gorbachev, J. Tu, A. Kretinin, Y. Cao, R. Jalil, F. Withers, L. Ponomarenko, B. Piot, M. Potemski, *et al. Nature Physics*, vol. 10, p. 784, 2014.
- [6] M. Aidelsburger, M. Atala, M. Lohse, J. Barreiro, B. Paredes, and I. Bloch *Physical Review Letters*, vol. 111, no. 18, p. 185301, 2013.
- [7] H. Miyake, G. A. Siviloglou, C. J. Kennedy, W. C. Burton, and W. Ketterle *Physical Review Letters*, vol. 111, no. 18, p. 185302, 2013.
- [8] A. G. Grushin, E. V. Castro, A. Cortijo, F. de Juan, M. A. Vozmediano, and B. Valenzuela *Physical Review B*, vol. 87, no. 8, p. 085136, 2013.

- [9] V. Gudmundsson and R. R. Gerhardts, *Physical Review B*, vol. 52, no. 23, p. 16744, 1995.
- [10] H. Doh and S.-H. S. Salk, *Physical Review B*, vol. 57, pp. 1312–1315, Jan 1998.
- [11] K. Czajka, A. Gorczyca, M. M. Maśka, and M. Mierzejewski, *Physical Review B*, vol. 74, no. 12, p. 125116, 2006.
- [12] V. M. Apalkov and T. Chakraborty, *Physical Review Letters*, vol. 112, no. 17, p. 176401, 2014.
- [13] A. Mishra, S. R. Hassan, and R. Shankar, *arXiv: 1512.05224[cond-mat.str-el]*, Dec. 2015.
- [14] Y. Hatsugai, T. Fukui, and H. Aoki *Phys. Rev. B*, vol. 74, p. 205414, 2006.
- [15] R. Resta *The European Physical Journal B-Condensed Matter and Complex Systems*, vol. 79, no. 2, p. 121, 2011.
- [16] F. Haldane, *Physical Review Letters*, vol. 107, no. 11, p. 116801, 2011.
- [17] A. H. MacDonald, *Physical Review B*, vol. 28, pp. 6713–6717, Dec 1983.
- [18] N. Goldman, *Journal of Physics B: Atomic, Molecular and Optical Physics*, vol. 42, no. 5, p. 055302, 2009.
- [19] P. Sriluckshmy, A. Mishra, S. Hassan, and R. Shankar *Physical Review B*, vol. 89, no. 4, p. 045105, 2014.

Publications in Refereed Journal:

a. Published:

- (1) P. V. Sriluckshmy, Archana Mishra, S. R. Hassan and R. Shankar,
“Topological transitions in a model with Particle-Hole symmetry, Pancharatnam-Berry Curvature and Dirac Points”
Physical Review B, Vol: 89, p: 045105 (Jan 2014).
- (2) Archana Mishra, S. R. Hassan and R. Shankar,
“Effects of interaction in the Hofstadter regime of the honeycomb lattice”
Physical Review B, Vol: 93, p: 125134 (Mar 2016).

b. Communicated:

- (1) Archana Mishra, S. R. Hassan and R. Shankar,
“Translational symmetry breaking and the disintegration of the Hofstadter butterfly”,
arXiv:1605.06307[cond-mat.str-el]. *Communicated to Physical Review B.*

Signature of Student:

List of Figures

1.1	Hofstadter butterfly in square lattice	4
1.2	Hofstadter butterfly in honeycomb lattice	5
1.3	Plot for magnetic field vs lattice constant	6
1.4	Honeycomb lattice	11
1.5	Enlarged unit cell in honeycomb lattice	12
2.1	Honeycomb lattice in magnetic field	21
2.2	Magnetic unit cell in honeycomb lattice in magnetic field	24
2.3	Energy spectrum of honeycomb lattice in magnetic field	26
2.4	Density of states of honeycomb lattice with nearest neighbor hopping	30
2.5	Hall conductivity vs Fermi function for $q = 30$	31
3.1	Two types of magnetic unit cell choices for $q = 3$	40
3.2	Energy band diagram of system in the symmetric phase and the nematic phase	43
3.3	Comparison of total energy of two mean field solution	44
3.4	Dipole moment and Quadrupole moment plot	44
3.5	Lattice in the nematic phase	45
3.6	Lattice in the ferrielectric phase	48
3.7	The Chern number distribution of the filled bands for various ranges of interaction strength for $m = 2$.	48

3.8	Phase diagram for $q = 3$	50
3.9	Depiction of current on the links and flux per plaquette in the lattice in the nematic and ferrielectric phase	51
3.10	Bond order distribution on the lattice	53
3.11	Quantum metric plot showing the first order transition	56
3.12	Pair correlation function on the lattice in the symmetric and the nematic phase	57
3.13	Plot for Pancharatnam Berry curvature for the symmetric, nematic and ferrielectric phase	58
4.1	Hofstadter butterfly in honeycomb lattice	61
4.2	Skeleton diagram of Hofstadter butterfly of honeycomb lattice	62
4.3	Landau fan diagram for non-interacting case	64
4.4	Figure showing self similarity of the Hofstadter butterfly	65
4.5	Hofstadter butterfly in symmetric phase	68
4.6	Hofstadter butterfly for the honeycomb lattice in the absence of interaction plotted by taking the maximum energy as the x-axis	69
4.7	Hofstadter butterfly for the honeycomb lattice in the presence of interaction plotted by taking the maximum energy as the x-axis for the flux in the range $(1/20, 19/20)$ for (a) $V = 1$, (c) $V = 2$ and (d) $V = 4$. (b) Hofstadter butterfly for the honeycomb lattice in the presence of interaction plotted by taking the maximum energy as the x-axis for the flux in the range $(1/3, 1/2)$ for $V = 1$. The maximum energy is plotted till half-filling	71
4.8	Landau fan diagram in the presence of interaction	73
4.8	Landau fan diagram in the presence of interaction	74
5.1	Plot for energy $E(k_1, k_2)$ vs k_2 for $t' = 0.5t$.	79

5.2	Plot for energy $E(k_1, k_2)$ vs k_2 for $t' = t$	79
5.3	Particle density plot as a function of R for $t' = 0.5t$ and $t' = t$	80
5.4	(color online) PB phase as a function of R for $t' = 0.5t$ and $t' = t$	81
5.5	PB phase as a function of filling for $t' = 1$. The PB phase is not negative for all values of the filling. For some values it is positive reflecting that the PB curvature of the band takes both positive and negative values.	82
5.6	Velocity vector measured in m/s as a function of X and Y for $t' = 0.5t$ and $t' = t$	82
5.7	Density profiles as a function of X, Y for $t' = t$ at different times. Lines are drawn in the above figures to show the rotation of the cloud as a function of time due to non-zero PB curvatures.	83

Chapter 1

Introduction

For many years now, the two dimensional electron gas (2DEG) has been an arena of research for condensed matter physicists where many novel and interesting physics have emanated. This has paved the way to a completely new zone of physics which includes the quantum Hall effect, the Hofstadter butterfly etc. Two dimensional electron systems, at very low temperatures, when subjected to a magnetic field show quantized plateaus of Hall resistance when plotted as a function of the applied magnetic field. This phenomenal discovery was made in 1980 by Klaus von Klitzing et al. [1] where they observed that the quantization of Hall resistance depends only on the fundamental constants (Planck's constant h and charge of electron e) and is accurate upto one part per billion. This constant is known as the von Klitzing constant and has led to the definition for the standard of resistance. The energy spectrum of electron in the 2D plane changes from a continuous spectrum to discrete Landau levels in the presence of a magnetic field. The Hall conductance is proportional to the Landau level filling. For fully filled Landau levels, the Hall conductance is quantized.

The story becomes even more thrilling when the above system is subjected to a periodic potential. The 2D electron system in the presence of a magnetic field and a periodic potential displays a fractal structure when the flux passing per unit cell is plotted with

respect to the single particle energy spectrum. One of the first quantum fractal structures to be discovered, this is called the Hofstadter butterfly named after Douglas Hofstadter who was the first person to propose this idea[2]. This butterfly diagram is seen when both the independent length scales in the problem: the periodicity of the periodic potential and the magnetic length, are comparable. This regime is called the Hofstadter regime.

1.1 Hofstadter regime

Free electrons in the presence of a magnetic field can be represented by the Hamiltonian

$$\hat{H} = \frac{(\hat{\mathbf{p}} - e\mathbf{A})^2}{2m} \quad (1.1)$$

where $\hat{\mathbf{p}}$ is the momentum operator, e is the charge of the electron and m is the mass of the electron. \mathbf{A} is the vector potential. On solving the Schrodinger equation for this Hamiltonian, the energy levels are quantized and are known as Landau levels [3]. The energy of the n^{th} Landau level is $\epsilon_n = \omega_c(n + 1/2)$ where $\omega_c = eB/m$ is the cyclotron frequency, B is the applied magnetic field and $\hbar = h/2\pi$ is the reduced Planck's constant. The magnetic length $l_c = \sqrt{\hbar/eB}$. Each of these Landau levels are highly degenerate.

Electrons in a periodic potential can be represented by the Hamiltonian

$$\hat{H} = \frac{\hat{\mathbf{p}}^2}{2m} + \hat{U}(\mathbf{r}) \quad (1.2)$$

where $U(r) = U(r + a)$ is the periodic potential and a is the periodicity of the potential. Solving this Hamiltonian, we get Bloch bands with wave functions satisfying Bloch's theorem [4–6].

Interesting and fascinating phenomena are seen when both the length scales: the lattice constant a and the magnetic length l_c , are comparable. Bloch electrons in the pres-

ence of a magnetic field can be represented by the Hamiltonian

$$\hat{H} = \frac{(\hat{\mathbf{p}} - e\mathbf{A})^2}{2m} + \hat{U}(\mathbf{r}) \quad (1.3)$$

Each Bloch band divides further into subbands giving rise to a fractal structure when the energy spectrum is plotted with respect to the magnetic flux passing through the palquette. This fractal structure, first studied and discovered by Douglas Hofstadter in 1976, [2] known as the Hofstadter butterfly is described in the following section.

1.2 Hofstadter Butterfly

Hofstadter in his paper [2], showed that when Bloch electrons are subjected to magnetic field, the energy spectrum versus magnetic flux plot shows a self-similar recursive pattern giving rise to a fractal structure. This feature is observed when the periodicity of the periodic potential is comparable to the magnetic length. The model he considered was that of the two dimensional square lattice in the presence of a perpendicular magnetic field such that magnetic flux passing through each plaquette is $\phi_q = \phi/\phi_0 = p/q$ where ϕ is the magnetic flux and $\phi_0 = h/e$ is the flux quantum.

Hofstadter plotted the flux per unit cell, β , with respect to the energy E as shown in Fig. 1.1 and listed the following properties of the plot:

- The spectrum for β is identical to that of $\beta + N$ where N is an integer.
- The spectrum for β is same as that of $-\beta$.
- If E belongs to the spectrum of β , then $-E$ must also belong to the spectrum of β .

He considered the portion of the graph between successive integers N and $N + 1$ as a unit cell. So, he looked for plot with $\alpha = 0 \leq \beta \leq 1$ which is shown in Fig. 1.1.

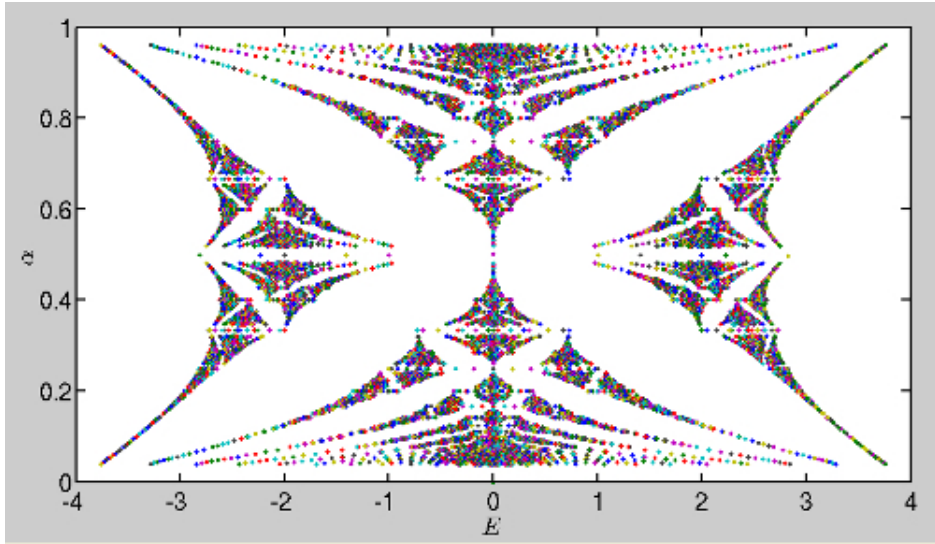


Figure 1.1: The figure shows the plot for α vs E in a unit cell. Here the x-axis is the single particle energy, E and y-axis represents the flux passing per unit cell, α .

This is the first fractal structure predicted in quantum systems. Each Bloch band splits into q bands and the gaps between these bands give a butterfly like pattern and hence known as Hofstadter butterfly. To understand the self similar recursive structure, Hofstadter further divided the unit cell into various subcells and showed that the whole unit cell exists in a compressed form with some rotation inside each of these subcells. These subcells, hence, can be further divided into subsubcells and again the whole unit cell structure is present inside these subsubcells and this continues. Thus, it gives rise to a self similar fractal like pattern.

This fractal structure can be seen in the case of any lattice in the presence of a strong magnetic field. Physicists later studied the Hofstadter butterfly plot for honeycomb lattice [7] which is shown in Fig. 1.2. Further description of the Hofstadter butterfly for honeycomb lattice will be done in Chapter 4.

Being the first fractal structure to be discovered in quantum physics, it has intrigued theorists and experimentalists alike. In the following section, we discuss the obstacles faced by the experimentalists in realizing this phenomenon in physical systems and the

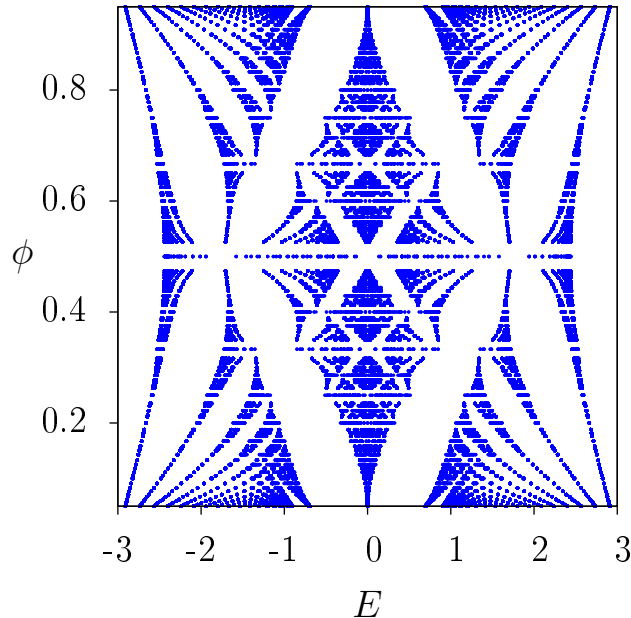


Figure 1.2: Hofstadter butterfly in honeycomb lattice. E is the energy eigenvalue and ϕ is the flux passing per unit cell.

various attempts to overcome these hurdles.

1.3 Realization of Hofstadter butterfly in physical system

The beautiful fractal structure predicted by Hofstadter was just a theoretical concept. There was no experimental evidence for the same. To realize this fractal structure, the first place to look is any physical system like say, graphene. To observe the fractal structure, the flux passing per plaquette should be high, almost equal to flux quantum.

The magnetic flux in a unit cell is $\phi = BA$ where B is the magnetic field and A is the area of the unit cell. In the case of graphene, area $A = 3\sqrt{3}a^2$. Here $a = 0.3$ nm is the nearest neighbor distance in graphene. The maximum magnetic field currently achievable in laboratory is around 80 T. So, the magnetic flux achievable in graphene is

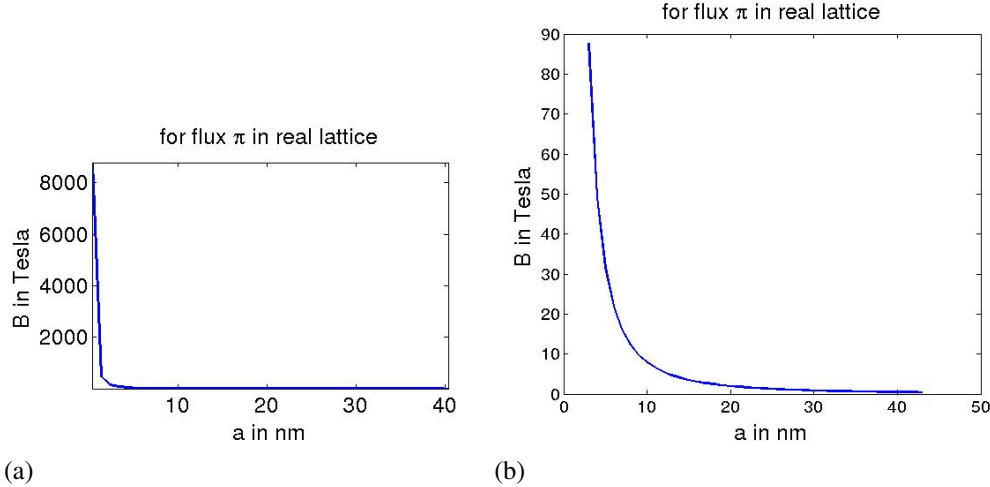


Figure 1.3: (a) Plot for magnetic field vs a such that flux passing per plaquette is π i.e. $q = 2$. (b) Zoomed in plot of (a)

$2\pi/322$ or less. Fig. 1.3 shows the plot for B vs a such that flux passing per plaquette is π . We see that for $a = 0.3$ nm, the magnetic field required for π flux passing through the plaquette is 8×10^3 T which is very high and out of reach in the laboratories in the present situation. Hence, it is impossible at present stage to see Hofstadter butterfly in any physical system as any atomic lattice has a very small lattice constant and thus the magnetic flux per plaquette is very small.

As can be seen from Fig. 1.3, to realize the Hofstadter butterfly experimentally, the lattice constant should be much larger than the atomic lattice system. The solution to this problem has in artificial lattice systems some of which are:

- Semiconductor superlattice
- Graphene superlattice
- Optical lattice

Many experiments have been done in these systems to realize the Hofstadter butterfly [8–16]. We will briefly discuss these systems below.

1.3.1 Semiconductor superlattice

Alternate layers of two different semiconductor materials form a semiconductor superlattice [17]. These two materials have different band gaps leading to formation of quantum wells. Periodicity of around 100 nm is created in this superlattice structure. Hence the magnetic field required for π flux is around 0.1 T which is easily achievable in laboratories. The first indication of the Hofstadter spectrum in an artificial semiconductor superlattice was given by Schlosser et al. [8]. The splitting of Landau levels was revealed by magnetoresistance oscillations. Although the manifestation of the Landau subbands was observed experimentally, a detailed view of the fractal structure of the Hofstadter butterfly became difficult in semiconductor superlattices because of the interplay of magnetic field dependent screening and the superlattice effects. The effective superlattice potential and thus the Landau level splitting reduces on increasing the magnetic field for enhancing the splitting. Hence, the splitting of Landau levels is very fragile and is visible for a narrow window in the values of the magnetic field. Inhomogeneities can also lead to Landau level broadening. In order to get a proper view of Hofstadter butterfly, high mobility homogeneous samples are required where the periodicity of the periodic potential is comparable to the magnetic unit length and creating such samples has been a challenge to the experimental community. Though more better and high quality samples and Hall measurements have further resolved the minigaps in the Hofstadter butterfly [9, 10], the ability to tune the carrier densities being limited and the restriction on reaching the full quantum Hall regime have been some constraints in observing the full spectrum of the Hofstadter butterfly.

1.3.2 Graphene superlattice

This is the place where the Hofstadter butterfly structure was actually seen for the first time. Recent experimental observations [11–14, 18] in moiré pattern in the graphene

superlattice have revealed the beautiful fractal structure of the Hofstadter butterfly. As in the semiconductor superlattice, we realize that the heterostructure created from alternating stacking of two different materials in many layers can lead to the modulation of the periodicity. Here in the case of these experiments in the graphene superlattice, graphene on hexagonal boron nitride (hBN) leads to a periodic moiré pattern. The moiré wavelength is proportional to the lattice constant mismatch between these two materials and the angle of rotation between these two lattices. The maximum moiré wavelength obtained through this method is approximately 14 nm when there is almost zero angle mismatch. With this lattice constant, the magnetic field required to have magnetic flux per plaquette of the order of the flux quantum is approximately 20 T.

The advantage of using hBN as the substrate for the graphene superlattice is that the lattice mismatch between these two lattices is around 1.8 which is less compared to other materials and thus the graphene superlattice can have a higher lattice constant. hBN also acts as an ideal substrate for the high mobility graphene device which is essential for high resolution quantum Hall measurements.

In these experiments, the magnetotransport measurements are done at high magnetic fields and they [11, 12] observe the evolution of the longitudinal and the Hall resistance for magnetic fields upto 31 T. The important insight used here to realize the Hofstadter butterfly is that each spectral gap in the fractal structure is characterized by two topological invariants (t_r, s_r) which satisfy a simple Diophantine equation

$$n/n_0 = t_r \phi/\phi_0 + s_r. \quad (1.4)$$

where n is the density of charge carriers and n_0 is the number of electron states per unit area when one band is filled such that $n_0 = 1/A$, here A is the area of the unit cell of the periodic potential. Hence, n/n_0 is the number of particles per unit cell. The Hall resistance plotted with respect to this normalized density n/n_0 and flux ϕ/ϕ_0 gives rise to

Chapter 1. Introduction

a fan like diagram known as the Landau fan diagram. In general quantum Hall systems, the Landau fan diagram exhibits straight lines whose slope gives the Hall conductivity equal to the Landau level filling fraction. Thus the diagram tracks the plateaus in the Hall resistance. These lines converge to the origin. But in case of Hofstadter system, the Landau fan diagram has straight lines whose slope gives the Hall conductivity but this is not equal to the filling fraction. These straight lines converge at various other values of n/n_0 . These intercept values are equal to s_r . Hence, in this system the ground states are characterized in terms of an integer valued intercept s_r and an integer valued slope t_r . The fractal structure in the Hofstadter butterfly is reflected in the Landau fan diagram which was probed experimentally in [11, 12].

Thus, these experiments confirm that the energy spectrum for electrons in the presence of a magnetic field and periodic potential can be described by the Diophantine equation involving two integer topological invariants. The ability to tune the periodicity of the potential and the amount of flux passing through each unit cell by the moiré pattern generated by graphene on hBN has made the complex physics of the Hofstadter spectrum experimentally accessible.

1.3.3 Optical lattice

Recent experiments using ultracold atoms in the optical lattice [15, 16] have been successful in realizing the Harper Hamiltonian whose spectrum is the Hofstadter butterfly. The optical lattice system is a very good arena to experimentally study the model Hamiltonians in condensed matter system in a clean disorder free and controlled environment. The charge neutrality of the atoms in the optical lattice was the main hindrance in studying the lattice in a magnetic field using ultracold atoms. Many ways have been devised to overcome this limitation like Coriolis force in a rotating atomic gas which is equivalent to the Lorentz force but this is equivalent to realizing the limit of weak magnetic

field. Another way devised out of this problem is using Raman lasers for inducing Berry phases. Engineering synthetic gauge potentials has been the recent topic of research in cold atom systems. Recent papers [15, 16] have successfully generated optical lattice in large tunable artificial magnetic fields achievable by synthetic gauge potentials using laser assisted tunneling and thus the realization of the Harper Hamiltonian has been made possible in ultracold systems.

These recent experimental results showing the accessibility of the Hofstadter butterfly has motivated us to understand the effect of interactions on it. We now give a review of past theoretical works that has motivated the work in this thesis and other topics related to the thesis work.

1.4 Brief Summary of past theoretical works

Interaction induced translational symmetry breaking phases have been studied previously by Castro et. al. [19, 20] in the honeycomb lattice in the absence of a magnetic field. To understand their model, we first describe the honeycomb lattice.

Honeycomb lattice is a 2D non-Bravais lattice with two basis atoms per lattice site. We can consider the honeycomb lattice to be made up of two interpenetrating triangular lattices. Thus, an unit cell of honeycomb lattice has two sublattices denoted as *A* and *B* shown by red and blue spheres respectively in Fig. 1.4. The basis vectors are \hat{e}_1 and \hat{e}_2 where,

$$\hat{e}_1 = a\hat{x} \quad \hat{e}_2 = -a\frac{1}{2}\hat{x} + a\frac{\sqrt{3}}{2}\hat{y} \quad (1.5)$$

where \hat{x} and \hat{y} are the unit vectors of the Cartesian coordinates. a is the lattice constant. The reciprocal lattice vectors are $\mathbf{G}_1 = \frac{2\pi}{\sqrt{3}a}(\sqrt{3}, 1)$, $\mathbf{G}_2 = \frac{4\pi}{\sqrt{3}a}(0, 1)$. There are three nearest neighbor atoms to each basis atom.

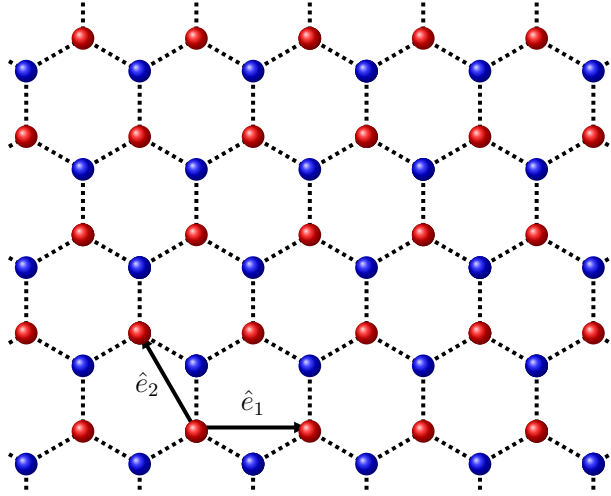


Figure 1.4: The figure shows a honeycomb lattice structure. The red balls represent A sublattice and the blue balls represent the B sublattice. \hat{e}_1 and \hat{e}_2 are the basis vectors of the lattice.

The Hamiltonian for this lattice with nearest neighbor hopping is

$$H = t \left(\sum_{\langle ij \rangle} c_i^\dagger c_j + h.c. \right) \quad (1.6)$$

where t is the hopping element, c_i and c_i^\dagger are respectively the annihilation and creation operators at site i . $\langle ij \rangle$ denotes i, j as nearest neighbors.

The key feature in the paper by Castro et. al. [19,20] was considering an enlarged unit cell consisting of six sites per unit cell ($A_1, B_1, A_2, B_2, A_3, B_3$), as shown in Fig. 1.5, relaxing the translational symmetry of the honeycomb lattice. The basis vectors for this system are $\mathbf{a}_1 = \hat{e}_2 - \hat{e}_1$ and $\mathbf{a}_2 = 2\hat{e}_1 + \hat{e}_2$. They considered spinless fermions on the honeycomb lattice with nearest neighbor hopping and nearest neighbor and next nearest neighbor interactions. The Hamiltonian for this system is

$$H = t \left(\sum_{\langle ij \rangle} c_i^\dagger c_j + h.c. \right) + V_1 \sum_{\langle ij \rangle} n_i n_j + V_2 \sum_{\langle\langle ij \rangle\rangle} n_i n_j, \quad (1.7)$$

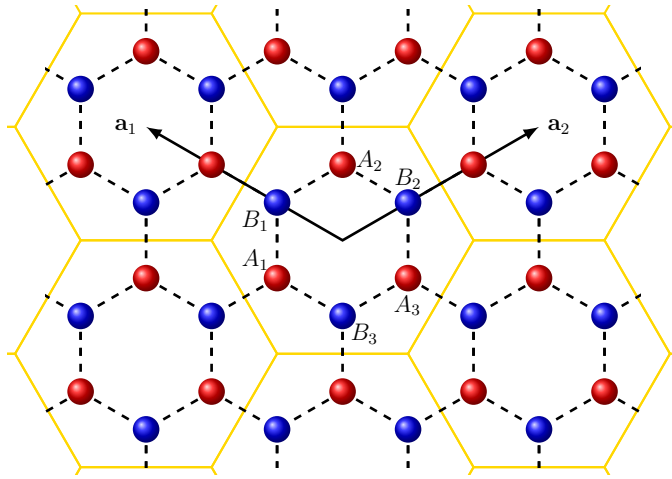


Figure 1.5: The enlarged unit cell considered by Castro et. al. [19, 20] consisting of six sublattices ($A_1, B_1, A_2, B_2, A_3, B_3$). $\mathbf{a}_1, \mathbf{a}_2$ are the basis vectors of this enlarged unit cell.

where V_1 and V_2 are the nearest neighbor and the next nearest neighbor repulsive interaction strengths respectively. Both these quantities and t are taken to be real. The number density operator at site i is denoted as n_i . $\langle\langle ij \rangle\rangle$ denotes i, j to be next nearest neighbors. This Hamiltonian was solved using mean field approximation where both bond order and charge order decoupling were allowed. The self consistency equations are solved for the half filled to the fully filled case with interaction strength varying in the range $0 \leq V_1, V_2 \leq 8$. In the parameter range, the interactions induce various complex phases like Kekule distortion, Pomeranchuk instabilities and reduced symmetry phases [20]. Near the van Hove singularity, the interaction induces spontaneous time reversal breaking phases with non-zero current on the links and charge ordering which spontaneously breaks the translational symmetry. The time reversal symmetry breaking results in non-zero Berry curvature of the bands leading to the anomalous Hall effect [21, 22]. This motivates us to realize the effect of interactions in the presence of a magnetic field where the time reversal symmetry is already broken by the magnetic field. In the presence of a magnetic field, due to magnetic translations the unit cell gets enlarged to a magnetic

Chapter 1. Introduction

unit cell. We would like to know how the charge ordering due to the interactions affect the symmetries of the lattice in the presence of a strong magnetic field and its effect on the already present non-trivial topology of the bands.

Interaction induced topological phases and phase transitions have also been studied in past. Haldane model, a Chern insulator, in presence of onsite interaction, shows phase transition from topological band insulator to topological antiferromagnetic insulator and topologically trivial band insulator. Topological transitions from quantum Hall phase with Chern no. $C = 2$ to $C = 1$ has also been observed in the Haldane-Hubbard model. Further the realization of the fractional quantum Hall state as the ground state in the interacting Chern insulator has led to the introduction of fractional Chern insulators.

The model we study is that of spinless fermions on the honeycomb lattice with nearest neighbor hopping and nearest neighbor interactions in the presence a of magnetic field. In the presence of interactions, charge ordering is induced which breaks the symmetries of the system and various complex phases like nematic phase, ferrielectric phase with Landau phase transitions are seen. Some of these first order Landau transitions are accompanied with topological transitions. These anisotropic ground states are further studied from the point of view of the quantum geometric approach.

The following section introduces the quantum geometric tensor, topological transitions and provides a review on the nematic state seen in the quantum Hall systems.

1.4.1 Quantum geometry

There is a growing realization that quantum geometry is a useful way of characterizing many body ground states of interacting fermions in a periodic potential [23, 24]. The physical states of any quantum system are the set of rays in a Hilbert space. The inner-product defines a natural geometry on the space of rays. It defines a distance between every pair and a geometric phase associated with every triplet of rays in the space[25,26].

For non-interacting systems, the ground state is specified by the eigenstates $\psi^n(\mathbf{k})$ of the single-particle Hamiltonian $H(\mathbf{k})$.

$$H(\mathbf{k})\psi^n(\mathbf{k}) = E^n(\mathbf{k})\psi^n(\mathbf{k}) \quad (1.8)$$

These states can be labeled by the conserved quasi-momenta (\mathbf{k}) which take values in the Brillouin zone (BZ). The geometry on the space of rays of the single-particle Hilbert space induces a geometry on the BZ. This is characterized by the quantum geometric tensor (QGT), $Q_{\mu\nu}(\mathbf{k})$, which is defined as the overlap between the covariant derivatives of the wave functions.

$$Q_{\mu\nu}(\mathbf{k}) = \langle D_\mu \psi(\mathbf{k}) | D_\nu \psi(\mathbf{k}) \rangle = \mathcal{G}_{\mu\nu}(\mathbf{k}) + i\mathcal{F}_{\mu\nu}(\mathbf{k}) \quad (1.9)$$

where the covariant derivative $D_\mu = \partial_\mu - i\mathcal{A}_\mu$. $\mathcal{A}_\mu = -i\langle \psi(\mathbf{k}) | \partial_\mathbf{k} \psi(\mathbf{k}) \rangle$ is the Berry connection. $Q_{\mu\nu}(\mathbf{k})$ is Hermitian and consists of a symmetric part, the quantum metric $\mathcal{G}_{\mu\nu}(\mathbf{k})$ and an anti-symmetric part, the Pancharatnam-Berry curvature (PBC) $\mathcal{F}_{\mu\nu}(\mathbf{k})$. [23, 27–29].

$$\mathcal{G}_{\mu\nu}(\mathbf{k}) = \text{Re.}(\langle \partial_\mu \psi | \partial_\nu \psi \rangle) - \mathcal{A}_\mu \mathcal{A}_\nu \quad \mathcal{F}_{\mu\nu}(\mathbf{k}) = \partial_\mu \mathcal{A}_\nu - \partial_\nu \mathcal{A}_\mu \quad (1.10)$$

The QGT characterizes the way in which the constituent particles are organized in the ground state.

A physical manifestation of the PBC is the anomalous component of the fermion velocity (perpendicular to the acceleration) resulting in a Hall current [30]. This leads to the identification of the quantized Hall conductivity with the integral of the PBC over the BZ, the Chern invariant [31–33] which is a topological invariant. The PBC can occur even without an external magnetic field if time reversal symmetry is broken. This leads to topological Fermi liquids and Chern insulators [21, 22]. The Z_2 invariant of topological

insulators can also be described in terms of the PBC of pairs of bands related by time reversal symmetry [34].

The quantum metric was shown to provide a natural variational parameter for the anisotropic fractional quantum Hall states [23]. It plays a central role in the geometric theory of the insulating state [24] since the average of the metric over the BZ has been identified with the localization tensor [24, 29, 35].

1.4.2 Topological Transitions

The phases of topological orders are identified by universal quantum numbers or topological invariants which are robust against arbitrary perturbations. The phases with the same topological invariants can be grouped into a single class and smoothly changed into one another. The observables corresponding to these topological invariants can take a discrete set of values for different classes of topological phases. Some other examples of such observables apart from the Hall conductivity are charges and statistics of the quasi-particles in the fractional quantum Hall systems with Z_n -like quantum numbers as the topological invariants [36], the spin and statistics of quasi-particles in spin systems with Z_2 as one of the topological invariants and the parity of the number of Dirac cones on the surface of topological insulators which are described by the Z_2 topological invariant [37].

Topological invariants do not change when the state changes continuously. Hence, if there is a transition between two topologically different states when the Hamiltonian parameters (coupling constants) are varied continuously, then either the topology must become ill defined for some region (which could be a single point) in the parameter-space or the state should change discontinuously as in a first order quantum phase transition.

Many examples of the former case have been discussed in the literature [21],[38, 39]. In the Haldane model[21], the Chern number becomes ill defined when the bands touch

at Dirac points. This occurs at the transition point when the Chern number changes from 0 to ± 1 . Examples of the change in topology without the gap closing have been given in some recent papers [38, 39]. These are the cases of symmetry protected topologies and involves going through a region where the protecting symmetry is broken and hence the topology is ill defined.

Though not common, first order topological transitions without closing of the gap have also been studied recently [40, 41] in the presence of strong electron-electron interaction. The phase transition seen in this thesis are also accompanied by first order topological transition.

The quantum Hall transitions we find are very different from the plateau transitions of standard integer quantum Hall effect (IQHE) which are driven by the physics of Anderson localization in the presence of magnetic fields [42]. When the filling factor is in the plateau region, the longitudinal conductivity is zero due to the mobility gap. There is no energy gap in the system. The mobility gap closes at the transition point causing the longitudinal conductivity to diverge (at zero temperature). In contrast, the model discussed in this thesis has no disorder. The transitions are interaction driven. The longitudinal conductivity is zero due to the energy gap. At the transition point, the energy gap does not close and hence the longitudinal conductivity remains zero.

1.4.3 Nematic phases in quantum Hall systems

Nematic phases in homogeneous quantum Hall systems have previously been theoretically studied [43–46] and experimentally observed [47–49] in fractional quantum Hall systems. 2D electron gas in the presence of a magnetic field occupy quantized degenerate Landau levels (LL). For weak magnetic field, the degeneracy of the LLs decreases and higher LLs are occupied. For partially filled Landau levels, $N \geq 2$, the longitudinal resistance exhibits strong anisotropy at low temperatures. Past works have shown

Chapter 1. Introduction

[43, 50–53] that when the Fermi level lies in the half filled higher Landau levels, the rotational symmetry of the system is broken. These nematic fluids have no quantized Hall current. But recent works have shown nematic phases with quantized Hall plateaus in fractional quantum Hall states under the application of a tilted magnetic field with non-zero $B_{||}$ [48, 49]. Interaction induced spatial symmetry breaking in fractional filled Chern bands with Chern number $C > 1$ has been studied by Kumar et. al. They have studied repulsively interacting fermions near half filling in square lattice models with $C = 2$ flat Chern band and a wide band gap. In this case, both the on-site interaction U and nearest neighbor interaction V are taken into consideration. By exact diagonalization method, they show that for $V \gg U$, the sublattice symmetry of the system is spontaneously broken and the ground state has a Hall conductivity of e^2/h at $T- > 0$. This can be generalized to higher Chern number bands which will lead to the breaking of sublattice/translational and rotational symmetries of the system, thus giving examples of interaction induced nematic phases.

In this thesis, we show that these nematic phases occur in the Hofstadter regime also.

1.5 Motivation behind the research work in the thesis

These recent experimental results showing accessibility of realizing the Hofstadter butterfly have motivated us to understand the effect of interactions in the Hofstadter regime. The interactions are expected to induce charge ordering in the ground state which may spontaneously break the translational symmetry of the system. Consequently, one of the length scales, namely the periodicity, can change. This could change the fractal structure. Therefore, we investigate translational symmetry breaking in the Hofstadter system. Interaction induced translational symmetry breaking phases have been studied in the honeycomb lattice in the absence of a magnetic field [19, 20, 54]. Effects of interactions on the Hofstadter butterfly have been discussed previously [55–61]. However these works

do not consider translational symmetry breaking.

The following section gives a preview of the thesis.

1.6 A preview of the thesis

This introductory Chapter is followed by 5 Chapters. The second Chapter is the review of the non-interacting case of the model considered and the topology of the bands. Addition of interactions in the the non-interacting system, introduces many interesting and complex phases which are described and discussed in Chapter 3. How the topology and the geometry of the ground state is affected by the presence of the interactions is also described in this Chapter. The effect of interactions on the fractal structure of the Hofstadter butterfly is elaborated in Chapter 4. Chapter 5 explicitly describes a method we have proposed to detect the PBC of bands by using ultracold atoms in an optical lattice.

This is followed by the conclusion in Chapter 6.

I lie within me

within I in me

Scale me up, scale me down

I am me, me am I

I replicate, repeat me

When huge, when tiny to see.

— the way fractal introduced itself to the author of
the thesis.

Chapter 2

Review of the non-interacting model

This Chapter elaborates on the non-interacting physics of our model as mentioned in Chapter 1. The non-interacting problem of the honeycomb lattice in magnetic field has been studied earlier [7, 62–64]. In this section, we briefly review some of the features of this problem that are relevant to this thesis. We discuss the symmetries of the non-interacting Hamiltonian and present the energy spectrum. The topology of the bands is also discussed further in this chapter.

2.1 Description of the non-interacting model

The non-interacting case of the model we study is basically a model of spinless fermions on the honeycomb lattice with nearest neighbor hopping in the presence of magnetic field.

$$H_0 = -t \sum_{\langle ij \rangle} \left(c_i^\dagger e^{i \frac{e}{\hbar} A_{\langle ij \rangle}} c_j + \text{h.c.} \right), \quad (2.1)$$

where $c_i (c_i^\dagger)$ is the annihilation (creation) operator for electrons at site i of the honeycomb lattice, t is the nearest neighbor hopping matrix element. h.c. stands for hermitian conjugate. $A_{\langle ij \rangle}$ is the vector potential on the link connecting i, j sites. The magnetic

field is applied in the z direction i.e. perpendicular to the plane of the lattice. We can represent the position of the site i as (m, n, a) where m, n are integers and denote the position of the unit cell along \hat{e}_1, \hat{e}_2 directions respectively. $a \in (A, B)$ is the sublattice index in the unit cell. The Hamiltonian can be written as

$$H_0 = -t \sum_{m,n} (c_{m,n,A}^\dagger c_{m,n,B} + c_{m,n,A}^\dagger e^{i \frac{e}{\hbar} A_{(m,n)(m,n+1)}} c_{m,n+1,B} + c_{m,n,A}^\dagger c_{m-1,n,B} + \text{h.c.}) \quad (2.2)$$

where the gauge fields are on the z links (as shown in Fig. 2.1), denoted as $A_{\langle ij \rangle}$, such that the magnetic flux passing through each plaquette is $\phi_q = \frac{1}{q} \frac{h}{e}$ where q is an integer. In Fig. 2.1, we depict the system with $q = 3$ and the flux passing per plaquette, $\phi_q = h/3e$. A and B are the sublattices of the honeycomb lattice. We denote the two basis vectors of the underlying triangular Bravais lattice by $\hat{e}_{1,2}$. x, y, z links are the nearest neighbor links to a sublattice as shown in Fig. 2.1.

2.2 Symmetries of the system

The symmetries under which this Hamiltonian remains invariant are translational, rotational and particle hole symmetries.

2.2.1 Translational symmetry

In the presence of a constant magnetic field, translation symmetry is implemented projectively [65], namely, translation is accompanied by a gauge transformation. These translational operators are known as magnetic translational operators. We denote the generators of unit translations in the \hat{e}_1 and \hat{e}_2 directions, Fig. 2.1, as τ_1 and τ_2 and operation of these

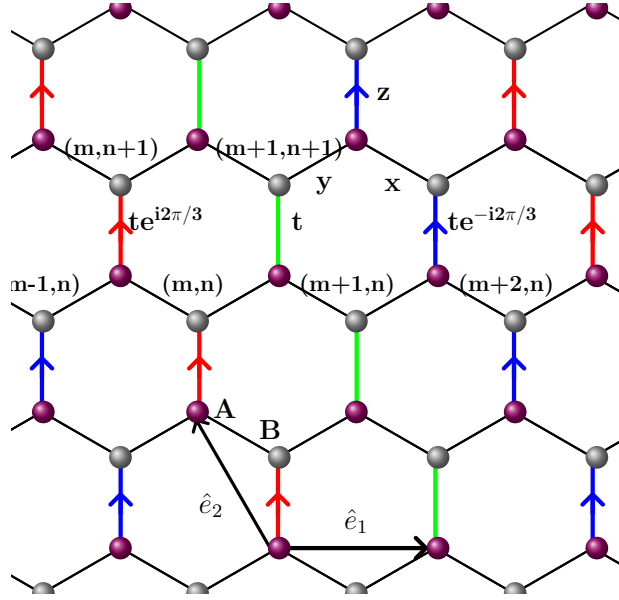


Figure 2.1: Honeycomb lattice in magnetic field with flux $\phi_q = \frac{h}{3e}$ passing through each plaquette. A and B are the two sublattices. The hopping parameter along the red lines are $t e^{i2\pi/3}$, along blue lines are $t e^{-i2\pi/3}$ and along green and black lines are t . \hat{e}_1 and \hat{e}_2 represent the basis vectors of the lattice. x, y, z are the nearest neighbor links.

translational operators on the fermionic operators are:

$$\tau_1 c_{m,n,a} \tau_1^\dagger = e^{i n \frac{e}{h} \phi_q} c_{m+1,n,a}, \quad \tau_2 c_{m,n,a} \tau_2^\dagger = c_{m,n+1,a}. \quad (2.3)$$

$$\tau_1 c_{m,n,a}^\dagger \tau_1^\dagger = e^{i n \frac{e}{h} \phi_q} c_{m+1,n,a}^\dagger, \quad \tau_2 c_{m,n,a}^\dagger \tau_2^\dagger = c_{m,n+1,a}^\dagger. \quad (2.4)$$

where $a \in A, B$. The Hamiltonian is invariant under these magnetic translational operators and commutes with these operators.

$$\tau_1 H \tau_1^\dagger = H, \quad \tau_2 H \tau_2^\dagger = H. \quad (2.5)$$

However, these magnetic translational operators τ_1 and τ_2 do not commute with each other and satisfy the relation,

$$(\tau_1 \tau_2 \tau_1^{-1} \tau_2^{-1}) c_{m,n} (\tau_2 \tau_1 \tau_2^{-1} \tau_1^{-1}) = e^{i \frac{e}{\hbar} 2\pi \phi_q} c_{m,n}. \quad (2.6)$$

rather $(\tau_1)^q$ and τ_2 commute with each other,

$$[(\tau_1)^q, \tau_2] = 0 \quad (2.7)$$

2.2.2 Rotational Symmetries

The honeycomb lattice has six-fold rotation symmetry about the center of a plaquette and three-fold rotation symmetry about any lattice site. It also has two-fold rotation (inversion) symmetry about the center of the links. The transformations of the fermion operators corresponding to the six fold rotation symmetry about center of any plaquette is,

$$\begin{aligned} R_6 c_{m,n,A} e^{in(n-1)\frac{e}{\hbar} \phi_q/2} R_6^\dagger &= c_{m-n,m,B} e^{im(m-1)\frac{e}{\hbar} \phi_q/2}, \\ R_6 c_{m,n,A}^\dagger e^{in(n-1)\frac{e}{\hbar} \phi_q/2} R_6^\dagger &= c_{m-n+1,m,B}^\dagger e^{im(m-1)\frac{e}{\hbar} \phi_q/2}. \end{aligned} \quad (2.8)$$

and

$$[H, R_6] = 0 \quad (2.9)$$

The transformations of the fermion operators corresponding to the three fold rotation symmetry about any sublattice A is,

$$\begin{aligned} R_3 c_{m,n,a} e^{in(n-1)\frac{e}{\hbar} \phi_q/2} R_3^\dagger &= c_{n-m,-m,a} e^{-im(-m-1)\frac{e}{\hbar} \phi_q/2}, \\ R_3 c_{m,n,a}^\dagger e^{in(n-1)\frac{e}{\hbar} \phi_q/2} R_3^\dagger &= c_{n-m-1,-m,a}^\dagger e^{-im(-m-1)\frac{e}{\hbar} \phi_q/2}. \end{aligned} \quad (2.10)$$

where $a \in [A, B]$ and

$$[H, R_3] = 0. \quad (2.11)$$

From here onwards, we address the 3-fold rotational symmetry as the rotational symmetry. The action of inversion symmetry operators on the fermion operators is,

$$\begin{aligned} Ic_{m,n,A}e^{in(n-1)\frac{e}{\hbar}\phi_q/2}I^\dagger &= c_{-m,-n,B}e^{-in(-n-1)\frac{e}{\hbar}\phi_q/2}, \\ Ic_{m,n,A}^\dagger e^{in(n-1)\frac{e}{\hbar}\phi_q/2}I^\dagger &= c_{-m,-n,B}^\dagger e^{-in(-n-1)\frac{e}{\hbar}\phi_q/2}. \end{aligned} \quad (2.12)$$

and

$$[H, I] = 0 \quad (2.13)$$

2.2.3 Particle-hole symmetry

The Hamiltonian is invariant under particle-hole symmetry which is an anti-unitary transformation in the many-particle Hilbert space. The transformation of the fermion operators under this symmetry is

$$Pc_{m,n,A}P^{-1} = c_{m,n,A}^\dagger, \quad Pc_{m,n,B}P^{-1} = -c_{m,n,B}^\dagger, \quad PiP^{-1} = -i. \quad (2.14)$$

As particle hole symmetry exists only for half filling, the Hamiltonian given by Eq. (2.2) is invariant under particle hole transformation for the half filling case.

2.3 Magnetic unit cell

As seen from Eqs. (2.6) and (2.7), τ_1 and τ_2 do not commute with each other and τ_1^q and τ_2 commute with each other. There can be many unit cell choices. We consider here a new unit cell, the basis vector in the \hat{e}_1 direction is q times the basis vector in the original unit cell while the basis vector along \hat{e}_2 direction is the same as the original unit cell in

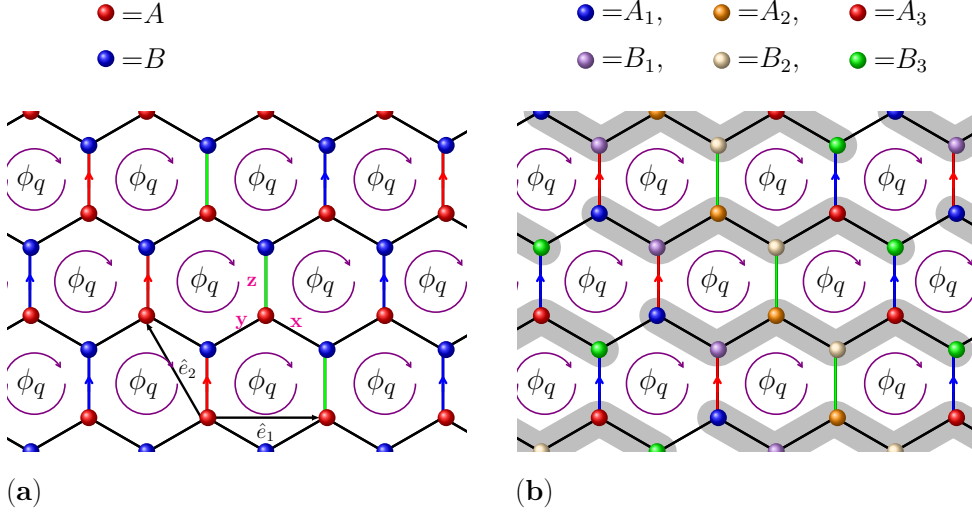


Figure 2.2: Honeycomb lattice in magnetic field with flux $\phi_q = \frac{h}{3e}$ passing through each plaquette. A and B are the two sublattices. The hopping along the red lines are $te^{i2\pi/3}$, along blue lines are $te^{-i2\pi/3}$ and along green and black lines are t . \hat{e}_1 and \hat{e}_2 represent the basis vectors of the lattice. x , y , z are the nearest neighbor links. (b) Honeycomb lattice showing magnetic unit cells. Here three original unit cells form a single magnetic unit cell as shown in the shaded area. A_1 , B_1 , A_2 , B_2 , A_3 , B_3 are sublattices of this magnetic unit cell.

absence of magnetic field. This enlarged unit cell is known as the magnetic unit cell. This magnetic unit cell consists of $2q$ sublattices. Fig. 2.2 shows the magnetic unit cell in the honeycomb lattice for flux $h/e3$. The shaded region shows the magnetic unit cell consisting of 6 sublattices i.e. $(A\alpha, B\alpha)$, $\alpha = 1, \dots, 3$.

Similarly, the Brillouin zone reduces and the reciprocal lattice vectors are now $\mathbf{G}_1 \in (-\pi/qa, \pi/qa)$ and $\mathbf{G}_2 \in (-\pi/a, \pi/a)$. This Brillouin zone is called the magnetic Brillouin zone or reduced Brillouin zone.

2.4 Energy spectrum

In the magnetic unit cell, we define the fermionic annihilation (creation) operators as $\psi_{I\alpha a}$ ($\psi_{I\alpha a}^\dagger$) which represents an electron annihilated (created) at sublattice $a \in A, B$ in

Chapter 2. Review of the non-interacting model

α^{th} position representing the original unit cell in I^{th} magnetic unit cell. As each magnetic unit cell contains q original unit cells, so, $\alpha = 1, \dots, q$. The Fourier transform of the fermion operator in momentum space is defined as, $\psi_{k_1, k_2, \alpha a} = \sum_I e^{i\mathbf{k} \cdot \mathbf{R}_I} \psi_{I\alpha a}$ where, \mathbf{R}_I is the position of I^{th} magnetic unit cell and \mathbf{k} is a vector in the reduced BZ.

The non-interacting Hamiltonian in the magnetic BZ is given by

$$H_0 = \sum_{k_1, k_2} \psi_{\mathbf{k}}^\dagger h_0(\mathbf{k}) \psi_{\mathbf{k}}, \quad (2.15)$$

where $h_0(\mathbf{k})$ is the single particle $2q \times 2q$ Hamiltonian matrix given by

$$h_0(\mathbf{k}) = \begin{pmatrix} 0_{q \times q} & F(\mathbf{k}) \\ F^\dagger(\mathbf{k}) & 0_{q \times q} \end{pmatrix}, \quad (2.16)$$

where $0_{q \times q}$ denotes a zero matrix of dimension $q \times q$ and F_k is a $q \times q$ matrix whose non-zero elements are

$$F_{\alpha, \alpha}(\mathbf{k}) = t(1 + e^{i2\pi\alpha/q} e^{ik_2})$$

,

$$F_{1, q}(\mathbf{k}) = t e^{-iqk_1}$$

,

$$F_{\alpha-1, \alpha}(\mathbf{k}) = t$$

for $\alpha = 2, \dots, q$. The eigenvalue equation can be written as

$$h_0(\mathbf{k}) \Phi_{\mathbf{k}}^m = \epsilon_{\mathbf{k}}^m \Phi_{\mathbf{k}}^m \quad (2.17)$$

where m is the band index, $\epsilon_{\mathbf{k}}^m, \Phi_{\mathbf{k}}^m$ are the eigenvalue and eigenfunction respectively.

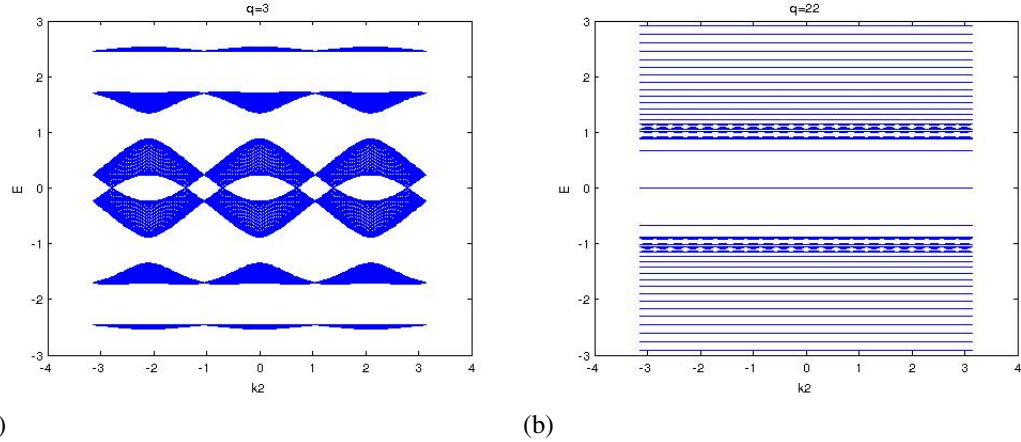


Figure 2.3: Energy spectrum for (a) $q = 3$ showing 6 bands and (b) $q = 22$ showing 44 bands.

As the single particle Hamiltonian at every \mathbf{k} is a $2q \times 2q$ matrix, we have $2q$ number of energy bands. Fig. 2.3 shows the energy spectrum for the values of the flux $h/3e$ and $h/22e$.

From the energy spectrum we can infer the following points:

- For the value of flux $2\pi/q$, there are $2q$ degeneracies in each energy band i.e. $E_{k_1, k_2} = E_{k_1, k_2 + 2\pi/q}$ which is the result of the system being invariant under the magnetic translational symmetry.
- At half filling, these degeneracies are found to be Dirac points as the energy dispersion is linear near these points. Hence, for flux $2\pi/q$, there are $2q$ Dirac points [66].
- On increasing the value of q i.e. decreasing the flux, the bandwidth of the bands decreases.
- A consequence of the decreasing bandwidth and the increasing number of degenerate points on decreasing the value of flux is that at energy $E = 0$, we see a flat band which is doubly degenerate when q is very large i.e. flux is very small.

- Apart from the $E = 0$ band, the bands around this $E = 0$ band are almost doubly degenerate for small flux passing through the plaquette. These bands are exactly doubly degenerate when $q \rightarrow \infty$.

2.5 Topology of the bands

The energy bands for the non-interacting model have non-trivial topology i.e. they have non-zero Hall conductivity, σ_H . Past works [31, 32, 67, 68] have shown that the Hall conductivity, when the Fermi level lies in n^{th} gap, is proportional to a topological number called the Chern number.

$$\sigma_H = \frac{e^2}{h} c_{tot} \quad (2.18)$$

where c_{tot} is the total Chern number of the filled bands which is an integer. Hence, the Hall conductivity is a topological quantity. This Chern number is calculated from the Berry potential in the BZ which is equivalent to a vector potential but in the momentum space [69]. This Berry gauge potential gives rise to Pancharatnam Berry curvature [70, 71] which acts like the magnetic field in the momentum space and is a gauge invariant quantity.

For the cases where the energy bands are well separated, we have an Abelian Berry potential which is calculated from the wave function of the Hamiltonian [64, 69] and is given as

$$\mathcal{A}_{\mathbf{k}}^m = i \langle \Phi_{\mathbf{k}}^m | \nabla_{\mathbf{k}} | \Phi_{\mathbf{k}}^m \rangle \quad (2.19)$$

where m is the band index. The Pancharatnam Berry curvature is given as

$$\mathcal{B}_{\mathbf{k}}^m = \nabla_{\mathbf{k}} \times \mathcal{A}_{\mathbf{k}}^m \quad (2.20)$$

and the Berry flux is

$$\tilde{\phi}_{\mathbf{k}}^m = \frac{1}{2\pi} \int_S \mathcal{B}^m \cdot dk_1 \wedge dk_2 = \oint \mathcal{A}^m \cdot d\mathbf{k} \quad (2.21)$$

where the integral is over the filled regions in the BZ. For completely filled bands, this Berry flux is an integer and is known as the Chern number. The Hall conductivity at m^{th} gap is the sum of the Chern number of the m filled bands.

When the energy bands are degenerate, the Berry potential is non-Abelian and is a matrix with the components

$$\mathcal{A}_{\mathbf{k}}^{mm'} = \langle \Phi_{\mathbf{k}}^m | \nabla_{\mathbf{k}} | \Phi_{\mathbf{k}}^{m'} \rangle \quad (2.22)$$

and the Chern number is given as

$$\tilde{\phi}_{\mathbf{k}}^m = \frac{1}{2\pi} \int Tr d\mathcal{A} \quad (2.23)$$

Numerically, the Chern number can be calculated by a lattice gauge theory technique [64, 72] where the Hamiltonian is diagonalized and the eigenfunction is computed on a discrete BZ with $\mathbf{k} = \mathbf{k}_r \equiv (k_{j1}, k_{j2})$ being the discrete points in the BZ such that $k_{j1} = 2\pi j_1 / (qN_1)$ along k_1 direction and $k_{j2} = 2\pi j_2 / (N_2)$ along the k_2 direction and $r = 1, \dots, N_1 N_2$, $j_\mu = 0 \dots N_\mu - 1$ with N_μ being the number of grid points along the k_μ direction. The periodic boundary condition is imposed on the wave function $\Phi_{k_l}^\mu = \Phi_{k_l + N_\mu \hat{\mu}}^\mu$ where $\hat{\mu} = (2\pi/qN_1, 2\pi/N_2)$. For the m^{th} filled band where the Fermi level lies in the m^{th} gap, a $U(1)$ link can be defined as

$$U_\mu(\mathbf{k}_r) = \frac{\det U_\mu(\mathbf{k}_r)}{|\det U_\mu(\mathbf{k}_r)|} \quad (2.24)$$

where $U_\mu^{mm'} = \langle \Phi_{k_l}^m | \Phi_{k_l + \hat{\mu}}^{m'} \rangle$. $\det U_\mu(\mathbf{k}_r)$ is zero at singular points and hence the link

Chapter 2. Review of the non-interacting model

variable is well defined at all points except these singular points. These points can be avoided from the mesh with an infinitesimal shift and the gauge invariant lattice field strength is

$$\mathcal{B}_{12}(\mathbf{k}_r) = \ln U_1(\mathbf{k}_r)U_2(\mathbf{k}_r + \hat{k}_1)U_1(\mathbf{k}_r + \hat{k}_2)^{-1}U_2(\mathbf{k}_r)^{-1} \quad (2.25)$$

The Chern number is

$$c_{tot} = \frac{1}{2\pi i} \sum_r \mathcal{B}_{12}(\mathbf{k}_r) \quad (2.26)$$

It has been shown [64] that the non-interacting theory has three regimes of electron densities. The dilute limit is called the Fermi regime where each filled band has Hall conductivity, $\sigma_H = -e^2/h$. Thus, $\sigma_H = -me^2/h$ when m bands are filled as is the case for non-relativistic systems in the continuum. At a certain filling, m^* , there is a band with a very large Chern number where the Hall conductivity changes sign when this band is completely filled. This band lies in the energy region of the van Hove singularity of the system in the absence of a magnetic field (Fig. 2.4). We refer to the m^* filling as the van Hove filling. Pairs of bands get degenerate on further filling. The Hall conductivity changes in steps of $2e^2/h$ when the Fermi level lies in the gap. This regime is called the Dirac regime. Fig. 2.5 shows the Hall conductivity as a function of Fermi energy E_F for $q = 30$ which illustrates the aforementioned regimes.

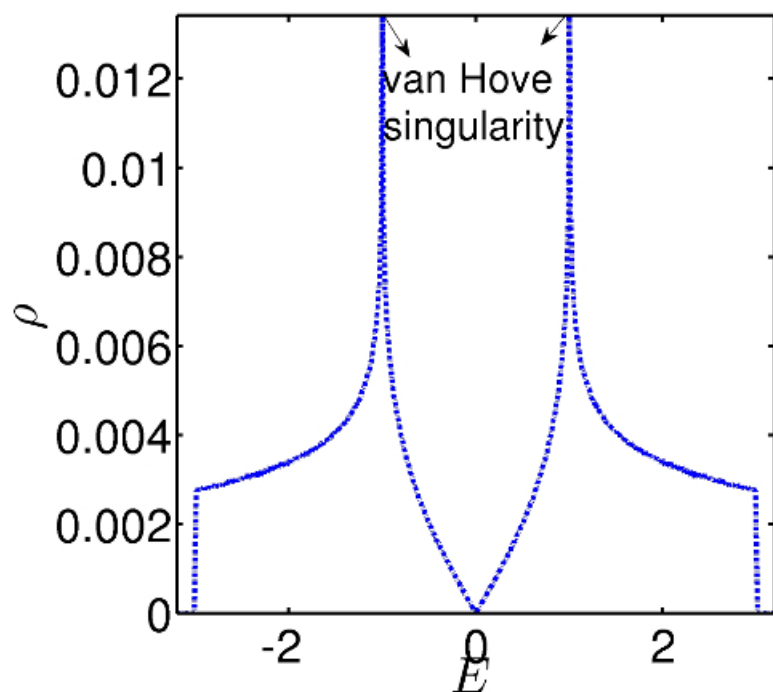


Figure 2.4: Density of states of electrons on the honeycomb lattice with nearest neighbor hopping plotted as a function of the energy in absence of magnetic field showing the van Hove singular points.

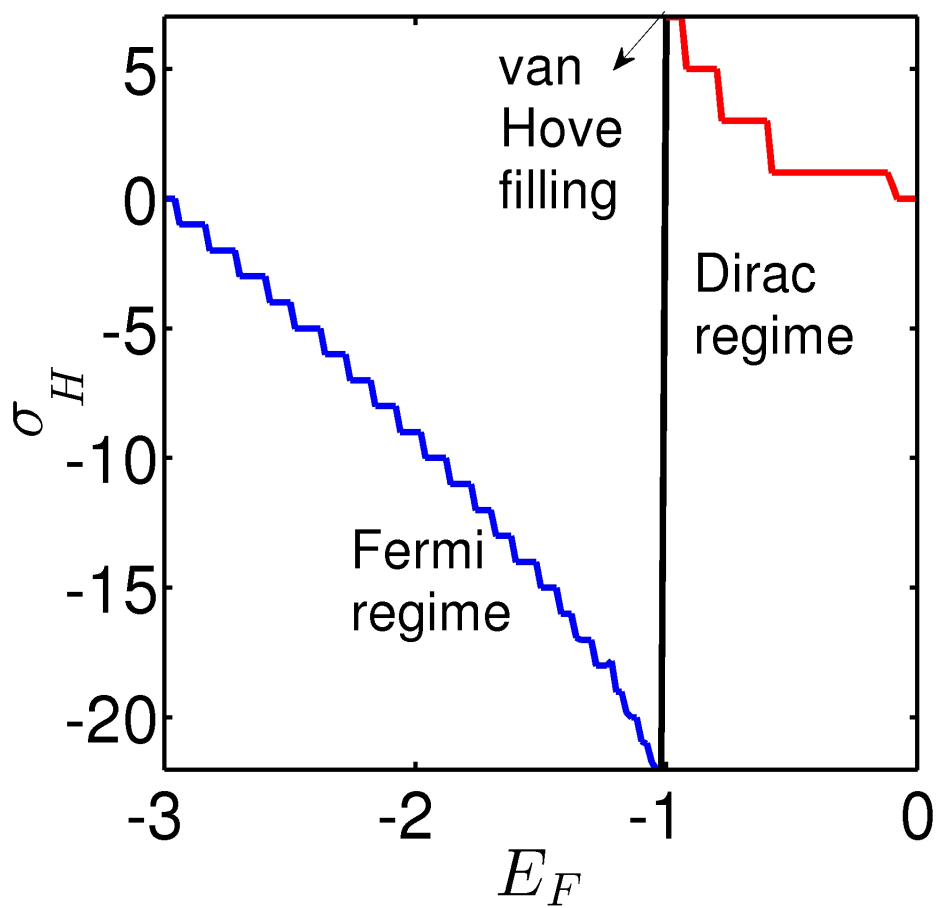


Figure 2.5: Hall conductivity as a function of the Fermi energy E_F till half filling for $q = 30$. The plot shows the Fermi regime, van Hove filling and the Dirac regime.

Chapter 3

Effect of interactions in the Hofstadter regime of the honeycomb lattice

As mentioned in the Chapter 1, the honeycomb lattice in a magnetic field giving rise to the Hofstadter fractals has gained a lot of attention with recent experimental observations. Interactions are always present in real systems, hence we would like to study the effects of interactions on this lattice in the Hofstadter regime. This Chapter describes this model in the presence of repulsive interactions, the method used to solve this problem and results we obtain.

3.1 Description of the model

We consider the Hofstadter system for spinless electrons in honeycomb lattice with nearest neighbor hopping and nearest neighbor interactions in the presence of magnetic field described by the following Hamiltonian,

$$H = -t \sum_{\langle ij \rangle} \left(c_i^\dagger e^{i \frac{e}{\hbar} A_{\langle ij \rangle}} c_j + \text{h.c.} \right) + V \sum_{\langle ij \rangle} n_i n_j, \quad (3.1)$$

where V is the nearest-neighbor interaction strength. Here onwards we consider $t = 1$ and write the interaction V in terms of t .

The Hamiltonian given in Eq. (3.1) still preserves the magnetic translational, 6-fold rotational, 3-fold rotational and inversion symmetries described in Chapter 2.

As discussed in the previous Chapter, in the presence of a magnetic field, we can consider a new unit cell called the magnetic unit cell. This unit cell choice is not unique as we can have various choices of the magnetic unit cell whose basis vectors can be written as $\mathbf{a}_1 = m_1\hat{e}_1 + n_1\hat{e}_2$ and $\mathbf{a}_2 = m_2\hat{e}_2 + n_2\hat{e}_1$ where m_1, n_1, m_2, n_2 are integers. The magnetic unit cell is chosen such that an integer amount of flux passes through the whole magnetic unit cell.

This magnetic unit cell can be visualized as a cluster and the lattice can thus be realized in terms of clusters. The Hamiltonian can be divided into intracluster and intercluster hopping and intracluster and intercluster interactions. Each cluster consists of $2q$ lattice sites. Hence we change our notation to include this feature in our Hamiltonian. Now each site is labeled by I, α, a where I labels the cluster position, α the original honeycomb unit cell inside a cluster such that $\alpha = 1, \dots, q$ and $a \in A, B$ denotes the sublattices. We define our fermionic operators in this magnetic unit cell/cluster as $\psi_{I,\alpha,a}$. So, the Hamiltonian can be rewritten in the language of clusters as

$$H = - \sum_{\langle I, \alpha, a, J, \beta, b \rangle} \left(\psi_{I,\alpha,a}^\dagger e^{i \frac{e}{\hbar} A_{\langle I, \alpha, a, J, \beta, b \rangle}} \psi_{J,\beta,b} + \text{h.c.} \right) + V \sum_{\langle I, \alpha, a, J, \beta, b \rangle} n_{I,\alpha,a} n_{J,\beta,b}, \quad (3.2)$$

The BZ is the set of wave vectors $\mathbf{k} = k_1 \mathbf{G}_1 + k_2 \mathbf{G}_2$, where $\mathbf{G}_{1,2}$ are the reciprocal lattice vectors of the reduced BZ. The Fourier transforms of the fermion operators in the momentum space are defined as, $\psi_{k_1, k_2, \alpha, a} = \sum_I e^{i \mathbf{k} \cdot \mathbf{R}_I} \psi_{I, \alpha, a}$ where, \mathbf{R}_I is the position of the I^{th} magnetic unit cell.

We solve this interacting problem using mean field approximation which is described in the following section.

3.2 Mean Field Theory

The interaction term is quartic and hence difficult to solve. To solve this problem, we use mean field approximation where we reduce the quartic term to quadratic terms by assuming Wick's decomposition and rewrite the interacting Hamiltonian in terms of the mean field single particle Hamiltonian.

Performing the mean field decomposition,

$$n_i n_j \approx \left((\bar{\rho} + \Delta_i) c_j^\dagger c_j + (\bar{\rho} + \Delta_j) c_i^\dagger c_i \right) - \chi_{\langle ij \rangle} c_i^\dagger c_j - \chi *_{\langle ij \rangle} c_j^\dagger c_i - \frac{1}{V} \left((\bar{\rho} + \Delta_i)^2 + (\bar{\rho} + \Delta_j)^2 - |\chi_{\langle ij \rangle}|^2 \right), \quad (3.3)$$

$$\frac{1}{V} \chi_{\langle ij \rangle} = \langle c_j^\dagger c_i \rangle_{MF}, \quad \frac{1}{V} \Delta_i = \sum_{j(i)} \langle c_j^\dagger c_j \rangle_{MF} - \bar{\rho}, \quad (3.4)$$

and hence the mean field Hamiltonian is

$$H_{MF} = \sum_{i(j)} (\bar{\rho} + \Delta_i) c_i^\dagger c_i + \sum_{\langle ij \rangle} \left(- (c_i^\dagger e^{i \frac{e}{\hbar} \mathcal{A}_{ij}} c_j + \text{h.c.}) - (\chi_{\langle ij \rangle} c_i^\dagger c_j + \text{h.c.}) \right) - \frac{1}{V} \sum_{\langle ij \rangle} \left((\bar{\rho} + \Delta_i)^2 - |\chi_{\langle ij \rangle}|^2 \right). \quad (3.5)$$

with the self consistency equations given as

$$\chi_{\langle ij \rangle} = V \langle c_j^\dagger c_i \rangle_{MF}, \quad \Delta_i = V \langle c_j^\dagger c_j \rangle_{MF} - \bar{\rho} \quad (3.6)$$

where Δ_i is the charge order parameter at site i and $i(j)$ represents the nearest neighbor sites of i and $\bar{\rho}$ is the uniform charge density. $\chi_{\langle ij \rangle}$ are the bond link operators. The self consistency equations Eq. (3.6) have to be solved keeping the number density fixed.

3.2.1 Algorithm to solve the self consistency equations

The single particle mean field Hamiltonian in the momentum space is the $2q \times 2q$ matrix $h_{MF}(\mathbf{k}) = h_0(\mathbf{k}) + h_F(\mathbf{k}, \Delta, \chi)$ where h_0 is the single particle non-interacting part of the Hamiltonian and h_F represents the interaction with the mean field parameters; \mathbf{k} takes values in the reduced (magnetic) BZ. There are $2q$ real charge density order parameters represented by $\Delta_{(\alpha,a)}$ and $3q$ complex bond order parameters represented by $\chi_{\langle(\alpha,a)(\beta,b)\rangle}$ where α, β label the original unit cells in the magnetic unit cell and a, b label the two sublattices of the honeycomb lattice. Our mean field ansatz allows the breaking of the translational, rotational and inversion symmetries of the system.

The complex bond order parameters $\chi_{\alpha,x}, \chi_{\alpha,y}, \chi_{\alpha,z}$ and the real charge order parameters $\Delta_{\alpha,a}$ are solved by an iterative method using the self consistency equations, Eq. (3.6), at a given filling and V for a particular value of flux per plaquette. The algorithm used is summarized here

1. Start the iteration with a random initial guess of $\chi_{\alpha,x}, \chi_{\alpha,y}, \chi_{\alpha,z}$, and $\Delta_{\alpha,a}$,
2. Diagonalize H_{MF} using $\chi_{\alpha,x}, \chi_{\alpha,y}, \chi_{\alpha,z}$, and $\Delta_{\alpha,a}$,
3. Calculate the expectation value of the link operators and the number operators on each site in a magnetic unit cell and using this compute $\chi_{\alpha,x}, \chi_{\alpha,y}, \chi_{\alpha,z}$ and $\Delta_{\alpha,a}$ from Eqs. (3.6).
4. The whole process in steps 2 and 3 is repeated until the difference between the calculated values of these order parameters for iteration $n + 1$ and n is below a given tolerance value.

We repeat this process for various initial guesses and often find different mean field solutions. Comparing the energies of these solutions, we pick up the lowest energy state as the ground state of the interacting Hamiltonian. Mean field approximation is a good

approximation when the Fermi level lies in the energy band gap. In the case of the honeycomb lattice in the Hofstadter regime, the energy spectrum has well separated energy bands with band gaps for flux $\phi/\phi_0 = 1/3$ or less and we solve the self-consistency equations for fully filled bands. Hence, we expect the mean field approximation to be a good approximation here.

Here in this chapter, we solve the self consistency equations for a value of flux per plaquette $\phi/\phi_0 = 1/3$ and in the next chapter, we solve the self consistency equations for a value of flux per plaquette $\phi/\phi_0 = p/q$.

3.3 $q = 3$ case

In this section, we describe the analysis for a value of flux per plaquette $\phi/\phi_0 = 1/3$ with $q = 3$ and $p = 1$ for filling $m = 1, 2, 3$ and elaborate the various complex phases we get by solving the self consistency equations in the following section. Here, the self consistency equations are solved by fixing the number of particles per unit cell, $n = \frac{1}{N^2} \sum_{k,m} n_F[\epsilon_{\mathbf{k},\mu}^m]$ where $N \times N$ is the lattice size, $n_F[\epsilon_{\mathbf{k}}^m, \mu]$ is the Fermi distribution function with $\epsilon_{\mathbf{k}}^m$ being the single particle mean field energy and μ is the chemical potential. As we solve the problem for the zero temperature case, numerically the temperature we use in the Fermi distribution function is 10^{-4} . Due to particle hole symmetry, we get the same phase diagram for filling $m = 6, 5, 4$ respectively.

In this case, there are 6 real charge order parameters and 9 complex bond order parameters. These order parameters are solved by using self consistency equations for a magnetic lattice of 150×150 . The tolerance value discussed in item 4 in the algorithm of the mean field approximation is considered to be 10^{-6} here. We analyze the various phases and the phase transitions as a function of the interaction strength. We discuss the topology and the geometry of these phases for further understanding these phases.

3.3.1 Order Parameters

The phases are characterized by the mean field order parameters Δ and χ and the quantities derived from these order parameters. The derived quantities we study are:

1. Dipole moment (described below)
2. Quadrupole moment (described below)
3. Magnitude of the bond order parameters.
4. Current on the links given by $-t\langle\psi_{I\alpha a}^\dagger e^{i\frac{e}{\hbar}A_{(I\alpha a, J\beta b)}}\psi_{J\beta b}\rangle - h.c.$
5. Flux in the plaquette (discussed later).

Non-uniform charge distribution can lead to charge density order on the lattice. If there is a staggered charge distribution between the A and B sublattices, then we get a charge density wave. In this case, only the inversion symmetry of the system is broken, the rotational and translational symmetries remain intact. We can also have charge distribution such that the rotational symmetries of the system are broken. We choose the dipole moment (P^μ) and quadrupole moment ($Q^{\mu\nu}$), of the single particle density, to be the order parameters that characterize the breaking of the rotational and inversion symmetries of the system. These are defined as,

$$P^\mu \equiv \frac{1}{N} \sum_i R_i^\mu (\Delta_i - \bar{\rho}), \quad (3.7)$$

$$Q^{\mu\nu} \equiv \frac{1}{N} \sum_i (2R_i^\mu R_i^\nu - \delta^{\mu\nu} \mathbf{R}_i \cdot \mathbf{R}_i) (\Delta_i - \bar{\rho}) \quad (3.8)$$

where R_i^μ , $\mu = 1, 2$ are the components of the position vector \mathbf{R}_i at the i^{th} site, $\bar{\rho}$ is the uniform charge density and N is the total number of original unit cells in the lattice.

$Q^{\mu\nu}$ can be non-zero only if the 3-fold rotational symmetry is broken and P^μ can be non-zero only if both, the 3-fold rotational and inversion symmetries are broken A.

We name the phase with zero dipole moment and non-zero quadrupole moment as the nematic phase and the phase with non-zero dipole moment and quadrupole moment as the ferrielectric phase which will be described explicitly in the following Chapter.

Apart from the mean field order parameters, we can also analyze the ground states from the topological and geometrical points of view which is discussed further in this chapter. For the $q = 3$ case i.e. flux $1/3$, the Hamiltonian is a 6×6 matrix and hence we have six bands. In the non-interacting case, when the lowest band is filled i.e. $m = 1$, the Hall conductivity, $\sigma_H = -e^2/h$. For $m = 2$, $\sigma_H = e^2/h$ and $m = 3$ i.e. at half-filling $\sigma_H = 0$. Due to particle-hole symmetry, the upper half bands behave similar to the lower half bands. As can be seen, the $m = 1$ band is in the Fermi region, $m = 2$ is the van Hove filling and $m = 3$ is the Dirac regime (see Chapter 2). Due to particle-hole symmetry, $m = 4$ filling lies in the Dirac regime while $m = 5$ is van Hove filling and $m = 6$ band is in the Fermi regime. We solve the self-consistency equations for $m = 1, 2, 3$ fillings as the upper half bands behave in a similar fashion as lower bands.

3.3.2 Unit cell choices

As discussed before in Chapter 2, the Hamiltonian is invariant under magnetic translations, τ_1 and τ_2 which are along \hat{e}_1 and \hat{e}_2 . These magnetic translation operators do not commute with each other, $\tau_1\tau_2\tau_1^{-1}\tau_2^{-1} = e^{i\frac{2\pi}{3}}$. Thus, we need to choose a magnetic unit cell consisting of three original unit cells to implement Bloch theory. In this case, there are two ways of doing this:

1. the linear unit cell denoted as unit cell choice I with basis vectors $3\hat{e}_1$, \hat{e}_2 as shown by the rectangular region shaded in gray in Fig. 3.1.
2. the hexagonal unit cell denoted as unit cell choice II with basis vectors $\hat{e}_2 - \hat{e}_1$, $\hat{e}_2 + 2\hat{e}_1$ as shown by the hexagonal region shaded in yellow in Fig. 3.1.

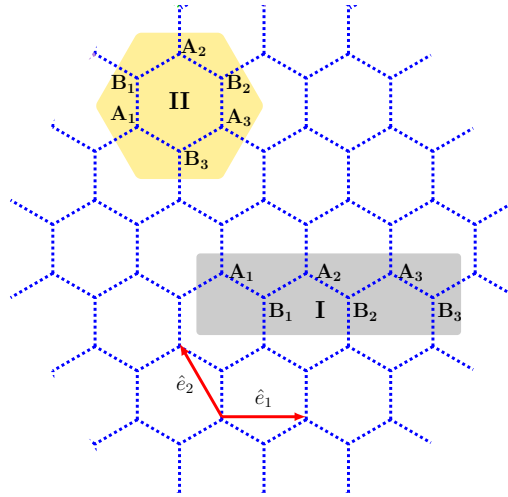


Figure 3.1: Honeycomb lattice in magnetic field with flux $\phi = \frac{h}{3e}$ passing through each plaquette. A and B are the two sublattices. We consider two possible choices of unit cell: linear choice (I) shown in gray rectangle and hexagonal choice (II) shown in yellow hexagon. $(A_1, B_1, A_2, B_2, A_3, B_3)$ are sublattices of these magnetic unit cells. \hat{e}_1 and \hat{e}_2 represent the basis vectors of the lattice.

Both these enlarged unit cells contain six sites $A_1, B_1, A_2, B_2, A_3, B_3$.

In this case there are 9 complex bond order parameters, $\chi_{1x}, \chi_{1y}, \chi_{1z}, \chi_{2x}, \chi_{2y}, \chi_{2z}, \chi_{3x}, \chi_{3y}, \chi_{3z}$, and 6 real charge order parameters, $\Delta_{1A}, \Delta_{2A}, \Delta_{3A}, \Delta_{1B}, \Delta_{2B}, \Delta_{3B}$.

Unit cell choice **II** is a rotationally symmetric choice where each sublattice is surrounded with three different sublattices unlike unit cell choice **I**. For non-interacting case, the ground states for both the choices are same but for mean field states, these ground states are different from each other.

3.4 Results and Analysis

In this section, we discuss the results and analyze the phases obtained by solving the self consistency solutions for $m = 1, 2, 3$ fillings.

For any value of V , there is always a scaled solution of the self consistency equations where the magnitude of the bond order parameters χ are of the form $\lambda(V)$ and the charge

density on each sublattice is the same and is equal to the uniform charge density $\bar{\rho}$. Here λ is a scaling factor which depends on the interaction strength, V . Thus, the hopping on the lattice is just scaled and hence, the mean field ground state is the same as that of the non-interacting ground state and the kinetic energy scales linearly for this mean field solution. Therefore, the total energy, E in this phase, can be written as

$$E = E_0(t - \lambda(V)t) + \sum_{bonds} \frac{\lambda^2(V)t^2}{V} - V \frac{m}{3} - \sum_{sites} \frac{|\Delta + \bar{\rho}|^2}{V}. \quad (3.9)$$

where m is the number of bands filled. Minimizing the energy with respect to $\lambda(V)$, we get $\lambda(V) = \frac{E_0 V}{18}$ where E_0 is the total energy of the non-interacting system. Similarly, minimizing the energy with respect to $\Delta(V)$, we get $\Delta(V) = -\bar{\rho}$ thus showing that there is no charge ordering. These values of χ and Δ satisfy the self consistency equations when checked numerically. This is the only solution for small values of the interaction strength, V , for all fillings and is the ground state of the system. In this phase all the symmetries of the system are preserved. We name this phase as the symmetric phase (S). As the ground state of the system is unchanged, the topology of the bands in the symmetric phase is the same as that of the non-interacting case.

At larger values of V , other mean field solutions are also present and comparing the energies of these mean field solutions, we obtain the ground state of the system.

3.4.1 Dirac regime: $m = 3$

At half filling ($m = 3$, Dirac regime), for both the choices of unit cells, there is a continuous transition from the symmetric phase to a charge density wave (CDW) phase at $V = 0.45$. This phase preserves all but the inversion symmetry of the system. The charge distribution in the unit cell is shown in Fig. 3.8. The dipole moment and quadrupole moment remain zero in this phase. As V is increased, the CDW strengthens but there are no other transitions for $V \leq 10$. The Hall conductivity remains zero and the Chern number

distribution in the bands remains unaltered and is similar to the S phase.

3.4.2 van Hove filling: $m = 2$

This filling is the van Hove filling as this band lies near the van Hove singularity of the energy spectrum in the absence of a magnetic field. The Hall conductivity, σ_H , for the non-interacting case for $m = 2$ filling is e^2/h . For the van Hove filling, the energy of the mean field solution for the unit cell **I** is always lower in energy than that of **II** for the range of V considered here.

Here on varying the interaction strength, we get three different phases with two phase transitions. These phases are described below:

Symmetric Phase

As described before, for small values of V the system is in the symmetric phase. The energy band diagram in this phase is shown in Fig. 3.2a. There is no charge ordering or bond ordering in this phase. As the wave function is the same as the non-interacting case, so the Hall conductivity is the same as that of the non-interacting case i.e. $\sigma_H = e^2/h$.

Nematic Phase

On increasing the interaction strength, there is a first order phase transition at a critical value $V = V_{c1} = 2.744$ from the S phase to an anisotropic phase which we denote as the nematic phase which is discussed in the next subsection. At V_{c1} , both the phases coexist i.e. the energy of the mean field solutions for both the symmetric and the nematic phases are the same and the order parameters change discontinuously at the phase transition point. Hence, it is a first order Landau transition. For $V > V_{c1}$ the nematic phase has an energy lower than that of the symmetric phase as can be seen from Fig. 3.3.

In this phase, the rotational and the translational symmetries of the system are bro-

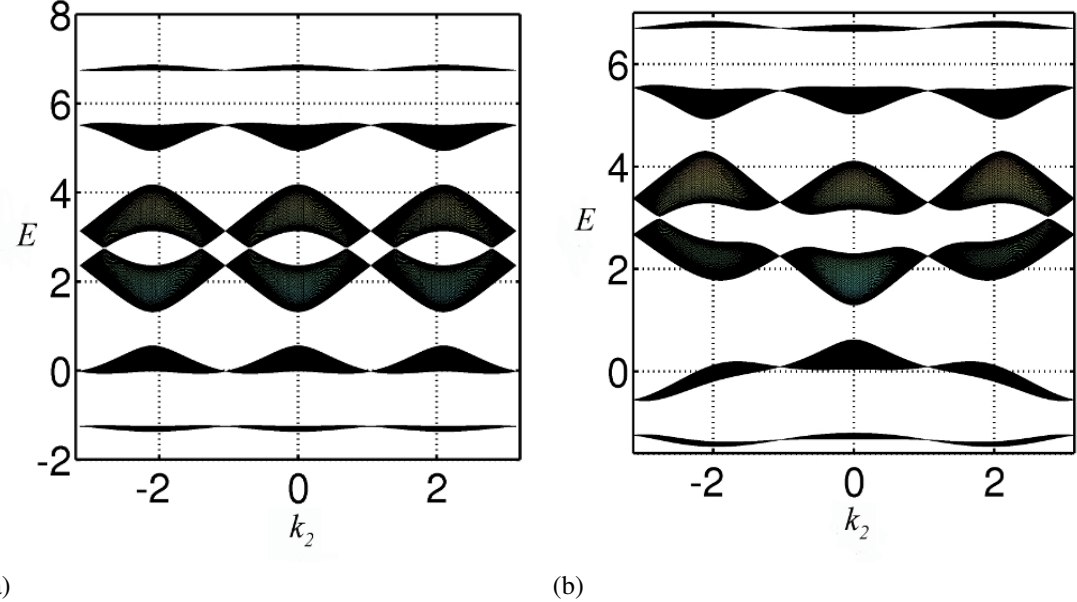


Figure 3.2: Energy band diagram w.r.t k_2 for (a) $q = 3$ in the symmetric phase for $m = 2$ at $V = 2.744$, (b) $q = 3$ in the nematic phase for $m = 2$ at $V = 2.744$. The energy band diagrams are plotted by diagonalizing the mean field Hamiltonian using the order parameters obtained by solving the self consistency equations for $m = 2$ and $q = 3$.

ken but the inversion symmetry of the system is preserved. This anisotropic phase has zero dipole moment but non-zero quadrupole moment and so the phase is denoted as the nematic phase (Fig. 3.4). Quadrupole moment is a 2×2 traceless matrix. In Fig. 3.4, we plot the magnitude of the eigenvalue of the quadrupole moment denoted as $|r|$. The blue line represents the plot for the magnitude of the dipole moment per original unit cell varying as a function of V .

The energy spectrum for the nematic phase at the transition point $V_{c1} = 2.744$ is plotted in Fig 3.2b. Comparing Fig. 3.2a and Fig. 3.2b, we see that in Fig. 3.2a, $E_{k_1, k_2} = E_{k_1, k_2 + 2\pi/3}$ which is the result of the system being invariant under translational symmetry unlike in the nematic phase where translational symmetry is broken which is reflected in the energy band diagram, Fig. 3.2b, where $E_{k_1, k_2} \neq E_{k_1, k_2 + 2\pi/3}$. Hence, in the latter case, the length scale, the periodicity of the mean field Hamiltonian, is now the same

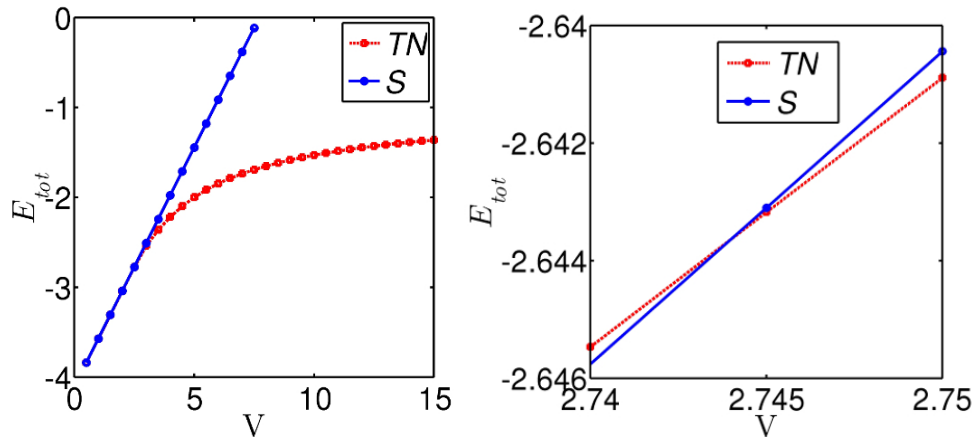


Figure 3.3: Energy comparison of the two mean field solutions for symmetric phase and nematic phase. At $V = 2.744$ both the energies values are same.

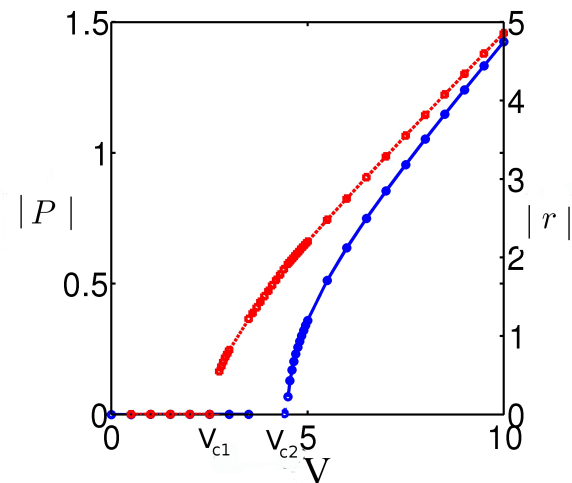


Figure 3.4: The quadrupole and dipole moments as a function of V in the three phases for $m = 2$. The blue line represents the polarization (i.e. dipole moment per original unit cell) and the red line represents the magnitude of the eigenvalue of the quadrupole moment matrix per original unit cell, $|r|$.

as that of the periodicity of the magnetic unit cell. As seen in Fig. 3.2a and Fig. 3.2b, there is always a band gap between the filled bands and the first excited band (i.e. band gap between second and third bands). The pictorial representation of the lattice in this phase is shown in Fig. 3.5. The bond parameters χ with different magnitudes are shown with different colors. The bonds depicted by thicker line are comparatively more stronger than the ones shown by thinner lines. Different color spheres represent different charge density. The size of the sphere depicts the magnitude of the charge density at a site where the biggest sphere represents the largest charge density in the lattice. From Fig. 3.5 we

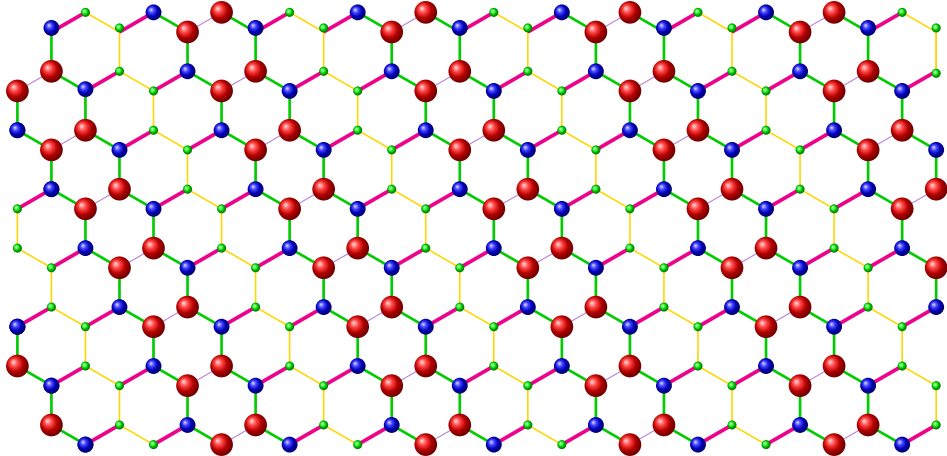


Figure 3.5: Pictorial representation of lattice structure in nematic phase showing the magnitude of bond order parameters and the charge ordering on the lattice.

see that

- The magnitude of the bond parameters, $|\chi_4| = |\chi_7|$ (magenta) $> |\chi_1| = |\chi_2| = |\chi_8| = |\chi_9|$ (green) $> |\chi_5| = |\chi_6|$ (yellow) $> |\chi_3|$ (lavender). χ_3, χ_5, χ_6 decrease as V is increased from V_{c1} to V_{c2} . Magnitude of other bond parameters increases with the increase of V in the nematic phase.
- The charge order parameters $\Delta_{A1} = \Delta_{B3}$ are illustrated by red spheres, $\Delta_{A2} = \Delta_{B2}$ are illustrated by green spheres and $\Delta_{A3} = \Delta_{B1}$ are illustrated by blue spheres. $\Delta_{A1} = \Delta_{B3}$ are positive and the largest in magnitude. All other charge

orders are negative with $\Delta_{A2} = \Delta_{B2} < \Delta_{A3} = \Delta_{B1}$.

- The total charge densities over A and B sublattices in a magnetic unit cell separately are zero i.e. $\Delta_{A1} = -(\Delta_{A2} + \Delta_{A3})$, $\Delta_{B3} = -(\Delta_{B2} + \Delta_{B1})$. The magnitude of each of the charge order parameters increases with increase in V .
- There is a preserved inversion symmetry if we consider a plane in y - axis passing through the link connecting the stars and a plane in x -axis crossing this link in between the adjacent stars i.e. a 2-fold rotation about the point in the middle of the bond connecting the two stars.

For example: For $V = 4$, $|\chi_1| = |\chi_2| = |\chi_8| = |\chi_9| = 1.7288$, $|\chi_4| = |\chi_7| = 2.4314$, $|\chi_5| = |\chi_6| = 1.3161$ and $|\chi_3| = 1.1134$. $\Delta_{A1} = 1.4258 = \Delta_{B3}$, $\Delta_{A2} = -0.4875 = \Delta_{B2}$ and $\Delta_{A3} = -0.9384 = \Delta_{B1}$.

This first order Landau transition from the symmetric phase to the nematic phase is accompanied by a change in the Hall conductivity of the system from e^2/h in the symmetric phase to zero in the nematic phase. Hence, we have a first order topological transition. Though the Hall conductivity, $\sigma_H = c_F e^2/h = 0$ in the nematic phase, but the individual occupied bands have non-zero Chern number. Here c_F is the total Chern number of the occupied bands. In the symmetric phase, the Chern number of the lowest band is -1 and of that of the second band is 2 . So, $c_F = 1$ and hence $\sigma_H = e^2/h$. But, for nematic phase, the Chern number of the lowest band is -1 and that of the second band is 1 (Fig. 3.7) and the total Chern number is zero giving rise to zero Hall conductivity. Hence we denote this nematic phase as the topological nematic phase (TN).

On further increasing the interaction strength, there is another first order Landau transition from the topological nematic phase to the ferrielectric phase which is explicitly described below.

Ferrielectric Phase

In this phase the translational, rotational and inversion symmetries of the system are broken. Here both the dipole moment and quadrupole moment are non-zero as shown in Fig. 3.4. Hence, we name this phase as the ferrielectric phase. The lattice picture of the system in this phase is shown in Fig. 3.6. From Fig. 3.6 we see that

- The magnitude of the bond parameters, $|\chi_4|$ (blue) $> |\chi_7|$ (pink) $> |\chi_8| = |\chi_9|$ (red) $> |\chi_1| = |\chi_2|$ (yellow) $> |\chi_5| = |\chi_6|$ (green) $> |\chi_3|$ (lavender).
• χ_3 and χ_7 decreases as V is increased from V_{c2} . Magnitude of the other bond parameters increase with the increase of V in the ferrielectric phase.
- The charge order parameters are all different at different sites of the magnetic unit cell which are denoted by different colors. Δ_{B3} (red spheres), Δ_{B2} (white spheres) and Δ_{A1} (magenta spheres) are positive in value. Δ_{B3} (red spheres) has the largest magnitude and Δ_{B2} (white spheres) has the lowest magnitude. All other charge orders are negative with Δ_{A2} (black spheres), Δ_{A3} (blue sphere), Δ_{B1} (green spheres) being almost the same in magnitude.
- The total charge densities over the A and B sublattices together in a magnetic unit cell is zero. The magnitude of each of the charge order parameters increases with an increase in V .

For example: $V = 7$, $|\chi_4| = 4.25559 > |\chi_7| = 2.1752 > |\chi_8| = |\chi_9| = 1.8914 > |\chi_1| = |\chi_2| = 1.7837 > |\chi_5| = |\chi_6| = 1.2959 > |\chi_3| = 1.0509$. $\Delta_{A1} = 1.5655$, $\Delta_{B1} = -2.0202$, $\Delta_{A2} = -2.0662$, $\Delta_{B2} = 0.4112$ and $\Delta_{A3} = -2.0844$, $\Delta_{B3} = 4.1939$.

In this phase the Hall conductivity remains zero. For the interaction strength $V_{c2} \leq V < 5.41$, the Chern number distribution of the occupied bands is the same as that of the nematic phase. Hence we denote this ferrielectric phase as the topological ferrielectric phase. At $V = 5.41$, both the occupied bands touch each other and there is a redistribu-

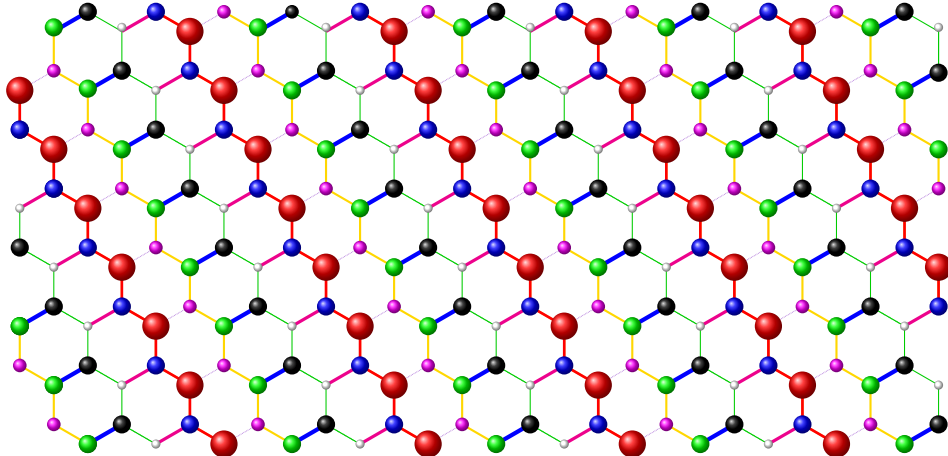


Figure 3.6: Pictorial representation of lattice structure in ferrielectric phase showing the absolute value of the bond kinetic energy and site charge order.

bution of the Chern numbers between these bands. Then for $V > 5.41$, though the Hall conductivity still remains zero but the Chern number of each of the occupied bands is now zero. This is clear from Fig. 3.7. Hence, this phase is just called as the ferrielectric phase.

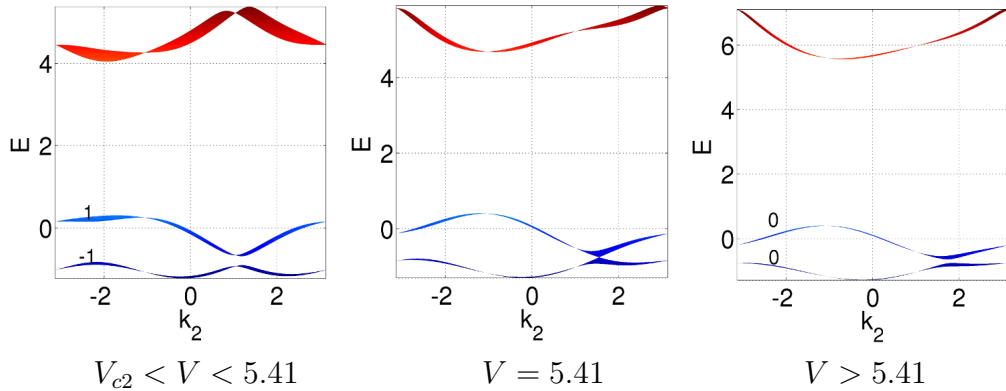


Figure 3.7: The Chern number distribution of the filled bands for various ranges of interaction strength for $m = 2$.

3.4.3 Fermi regime: $m = 1$

This filling is in the Fermi regime. Here the Hall conductivity for the non-interacting case is $-e^2/h$. In the presence of interactions, on solving the self consistency equations for both the choices of the unit cell, we find that the unit cell choice **II** has lower energy compared to that of **I**. Here, we find a first order transition from the symmetric phase to a nematic phase (N) (Fig. 3.8), at $V = 5.265$. The charge distribution has no dipole moment but has non-zero quadrupole moment in the nematic phase. The Hall conductivity changes from $\sigma_H = -e^2/h$ to zero at this transition. Thus, this is also a first order Landau transition accompanied by a topological transition.

All the phases at various fillings can be summarized in a diagram shown in Fig. 3.8. The phases with broken symmetry, their charge ordering and Hall conductivities, discussed above, are depicted in this figure. Here, the charge distribution is shown in a magnetic unit cell. In a particular phase, the sites with the same charge are represented by spheres of the same color. The magnitude of the charge density is indicated by the size of the spheres. Sphere with bigger size has higher magnitude of charge density. The Chern number distribution for all the filled bands in each filling is given in the bracket. The left most number in the bracket represents the Chern number for the lowest band and next number is for the next filled band. The right most number in the bracket gives the Chern number of the highest band filled.

3.5 Current on the links and flux per plaquette

The bond order parameters also acquire anisotropic phases which manifest as circulating currents. There is no current on the links in the symmetric phase and the charge density wave phase. Fig. 3.9 shows the current on the links on the lattice in the nematic and the ferri-electric phases. In the nematic phase, currents of equal magnitude flow on the links

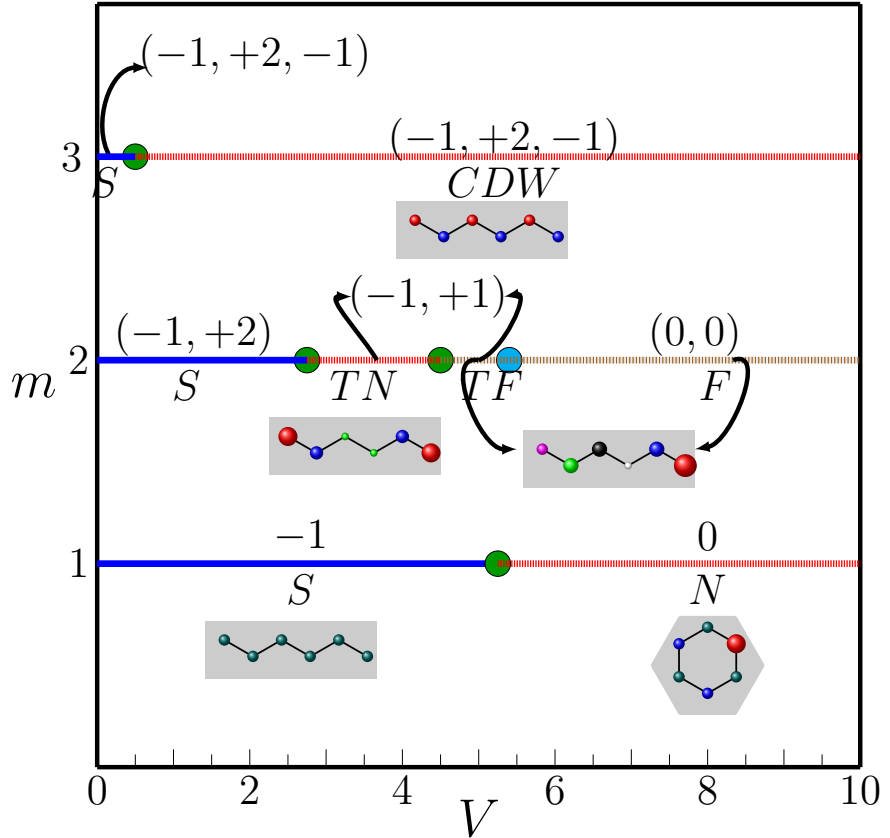


Figure 3.8: Phase diagram for $m = 1, 2, 3$ fillings as V is varied. The charge distribution in each phase is shown by the unit cell whose repetition gives the full lattice picture of the ground state. The Chern number distribution of the filled bands is given in bracket. For example in the $m = 2$ case, the left number in bracket is for the lowest band and the next number is for the second band. The green circle is the transition point. The blue circle is the point where the Chern numbers of the filled bands change without any change in the Hall conductivity.

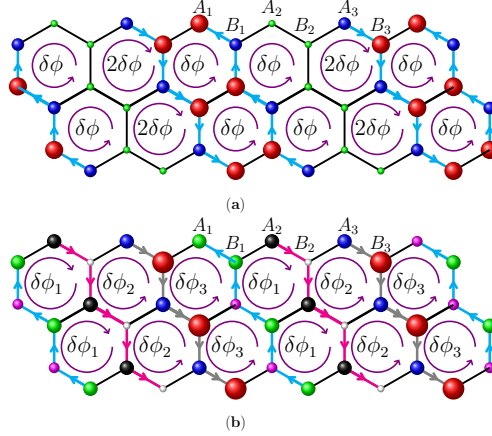


Figure 3.9: Flux in the plaquette and the current flowing on the links on the lattice for $m = 2$ in (a) the nematic phase (b) the ferri-electric phase. The flux distribution is shown after subtracting out the background flux $2\pi/3$. In ferri-electric phase, $\delta\phi_1 = \delta\phi_3 + \delta\phi_2$. The bonds with arrows are the links on which there is non-zero current. Links with the same color represents the same magnitude of current.

A_1B_1 and A_3B_3 (links with arrows) but in opposite directions (as shown in Fig. 3.9a) such that the inversion symmetry (about the A_2B_2 link) of the system is preserved. There is no current on the A_2B_2 links. In the ferri-electric phase, the current flows on the links A_1B_1 , A_2B_2 and A_3B_3 (Fig. 3.9b)) such that the total current on the links in the magnetic unit cell is zero. The current distribution shows that the inversion symmetry of the system along with the rotational symmetry is broken.

This figure also gives the distribution of the flux in the plaquettes of the system in the nematic and the ferri-electric phases. In Fig. 3.9 the flux distribution is shown after subtracting out the background flux $2\pi/3$. As seen in Fig. 3.9a, the staggered flux in the nematic phase is distributed in a way that the inversion symmetry of the lattice is preserved unlike that in the ferri-electric phase where the flux distribution shows inversion symmetry breaking (Fig. 3.9b). In both the cases the total flux in the magnetic unit cell is zero.

Comparing these staggered flux patterns in the lattice with the flux pattern discussed in the paper by Castro et al. [19] for the two phases with broken time reversal symme-

try: **T-I** (TRS and inversion symmetry both broken) and **T-II** (TRS broken but inversion symmetry preserved) phases, we see that the flux pattern for the nematic phase is similar to that of the **T-II** phase in [19] and in both these cases the inversion symmetry of the system is preserved. The staggered flux pattern in the ferrielectric phase shows inversion symmetry breaking in the system as is the case for **T-I** phase in [19]; but in the ferrielectric phase every plaquette has non-zero flux passing through it and the staggered flux in all the three plaquettes forming the magnetic unit cell have different magnitude unlike the **T-I** phase.

There is no current flowing on the link or any staggered flux passing per plaquette for the nematic phase in $m = 1$ case.

3.6 Insight to the topological transition

Insight to the mechanism of the topological transitions accompanying the Landau transitions can be achieved by studying the pattern of the anisotropic magnitudes of these bond order parameters shown in Fig. 3.10. The bond strength distribution for the TN , TF and F phases indicate that the mean-field Hamiltonian resembles that of weakly coupled ribbons (Fig. 3.10a), namely a quasi-1d system. The coupling becomes weaker as the interaction strength is increased. In the limit of completely decoupled ribbons, Chern numbers for all the bands should be equal to zero and this happens for $V > 5.41$. Thus it seems that the anisotropy of the bond order parameters drives the change of Chern numbers. The N phase at $m = 1$ is similar except that it tends to a system of weakly coupled clusters as shown in Fig. 3.10b.

However, while we believe that there is some truth to the argument given above, there are some caveats. Firstly, the transitions need not happen at a finite value of V but could happen only at $V = \infty$. Secondly when the system gets decoupled, the Chern numbers of the individual bands can get ill-defined due to degeneracies. Both these issues can be

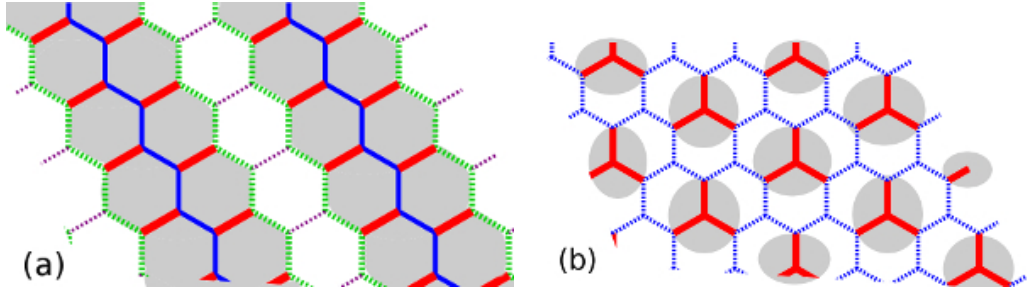


Figure 3.10: (a) Bond order parameter strengths for $m = 2$ broken symmetry phases. The red bonds are the strongest and the dotted violet bonds the weakest. (b) Bond order parameters for the $m = 1$ broken symmetry phase. The red bonds are stronger than the dotted blue bonds.

illustrated in the half-filled case of $m = 3$. As shown in Fig. 3.8, the Chern numbers in this case remain unchanged throughout the range, $0 \leq V \leq 10$. We now show that this is true for arbitrary V . As mentioned earlier, the single particle mean field Hamiltonian is of the form, $h_{MF}(\vec{k}) = h_0(\vec{k}) + h_F(\vec{k}, \chi, \Delta)$ For the half filled case, the system is isotropic and the bond order parameters simply scales $h_0(\vec{k})$ and the charge modulation is $\pm\Delta$ for the two sublattices. Since $h_0(\vec{k})$ does not couple the two sublattices, we can write $\vec{h}_{MF}(\vec{k})$ as,

$$h_{MF}(\vec{k}) = \begin{pmatrix} \Delta & F(\vec{k}) \\ F^\dagger(\vec{k}) & -\Delta \end{pmatrix} \quad (3.10)$$

It can be proved, as we do in Appendix C, that the Chern numbers of the above Hamiltonian are independent of Δ . As $V \rightarrow \infty$ we also have $\Delta \rightarrow \infty$. In the limit, there are two degenerate ground state corresponding to all the particles occupying one of the sublattices. However, all the the negative energy single particle states are degenerate and thus the three lower bands are completely degenerate. Thus the individual Chern numbers are ill-defined at $V = \infty$. At $\Delta = 0$ (the symmetric phase), the middle band Chern numbers are ill-defined due to the Dirac points. However, the system is particle-hole symmetric

in this phase and the Chern numbers get fixed by demanding that the sum of the Chern numbers, which is proportional to the Hall conductivity, is zero. Thus the Chern numbers in the half filled case are unchanged in the range $0 \leq V < \infty$.

3.7 Geometry of the ground state

The geometry of the ground state is characterized by the quantum geometric tensor (QGT) discussed in Chapter 1. Here, we analyze our ground state in terms of the symmetric part (quantum metric) and the antisymmetric part (PBC) of the QGT. We study the pair correlation function and its relation with the quantum metric in order to analyze the anisotropic phases in the system. [24].

3.7.1 Quantum metric

The structure of incompressible liquids is described by the pair correlation function. For our system it is defined as,

$$\Gamma_{\alpha a, \beta b} (\mathbf{R}_I - \mathbf{R}_J) = \langle c_{Ia\alpha}^\dagger c_{Jb\beta}^\dagger c_{Jb\beta} c_{Ia\alpha} \rangle \quad (3.11)$$

where $\mathbf{R}_I, \mathbf{R}_J$ represent the position of the I^{th} and J^{th} magnetic unit cell respectively. The anisotropic state of the system can be understood in terms of this pair correlation function. The nematic order parameter has been related to the quantum metric [44, 46]. In this section, we would therefore like to study the pair correlation function in the light of quantum geometry described by the quantum metric. The relationship between the momentum space quantum metric [24] averaged over the BZ, $\bar{g}^{\mu\nu}$, and the structure factor has been shown by Resta in his paper [73]. Here, we give an alternate proof of this relationship in the lattice picture in the appendix B. The structure factor is $S_{\alpha a, \beta b} (\mathbf{R}_I - \mathbf{R}_J) = \langle c_{Ia\alpha}^\dagger c_{Ia\alpha} \rangle \langle c_{Jb\beta}^\dagger c_{Jb\beta} \rangle - \Gamma_{\alpha a, \beta b} (\mathbf{R}_I - \mathbf{R}_J)$.

On very general grounds, the average of the momentum space quantum metric over the BZ for interacting systems has been identified with the localization tensor [24], $\bar{g}^{\mu\nu} = \langle \hat{R}^\mu \hat{R}^\nu \rangle - \langle \hat{R}^\mu \rangle \langle \hat{R}^\nu \rangle$ where \hat{R}^μ are the components of the position operator. In our case we have

$$\hat{R}^\mu = \sum_{I,\alpha,a} (R^\mu - R_0^\mu)_{I\alpha a} c_{I\alpha a}^\dagger c_{I\alpha a} \quad (3.12)$$

where \mathbf{R}_0 is the position vector of the center of mass of the lattice which we consider as the origin and hence $\mathbf{R}_0 = (0, 0)$. Using the expression in Eq. (3.12) we can write

$$\bar{g}^{\mu\nu} = \frac{1}{L^2} \sum_{I\alpha a, J\beta b} (R_{I\alpha a}^\mu - R_{J\beta b}^\mu) (R_{I\alpha a}^\nu - R_{J\beta b}^\nu) S_{\alpha a, \beta b} (\mathbf{R}_I - \mathbf{R}_J), \quad (3.13)$$

This relation is the lattice version of the relation between localization tensor and the structure factor shown by Resta [73].

Thus $\bar{g}^{\mu\nu}$ is the second moment of the structure factor. It therefore characterizes the shape of the pair correlation function just as the real space metric introduced by Haldane [44] for homogeneous quantum Hall systems. To obtain a more precise relation between the two, we need to examine the weak field (large q) limit which we have not analyzed in the thesis.

The metric is a second rank symmetric tensor and has three independent components. These can be taken to be the orientation of the principle axis, θ and the two eigenvalues g_1, g_2 . Eq. (3.13) shows that the spread of the pair correlation function in the directions along and normal to the principal axis is given by $\sqrt{g_1}$ and $\sqrt{g_2}$. Therefore, the areal extent of the correlations $\sim \sqrt{g_1 g_2} \equiv l_g^2$, the square root of the determinant of the $\bar{g}^{\mu\nu}$. The ratio of the two eigenvalues $\gamma = g_1/g_2$ is a measure of its anisotropy. l_g^2 and γ are plotted as a function of the interaction strength in Fig. 3.12. l_g^2 decreases while the anisotropic parameter γ increases on increasing V .

The structure function reflects the symmetry (or the lack of it) of the ground state.

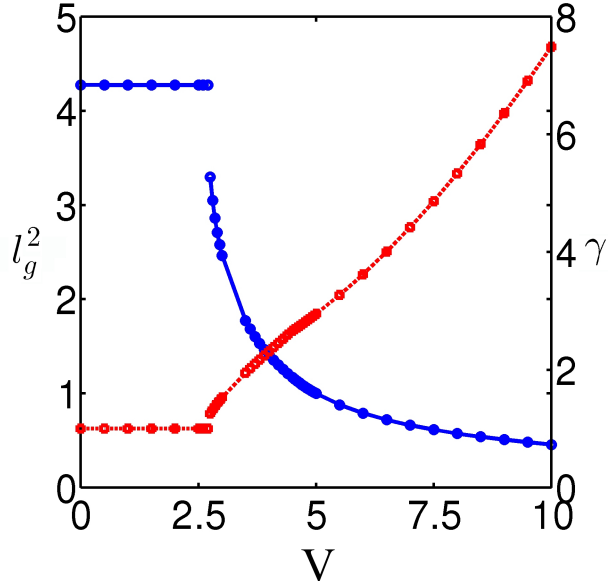


Figure 3.11: $l_g^2 = \sqrt{g_1 g_2}$ and γ vs V for $m = 2$. The blue line represents l_g and the red line represents γ . The discontinuity in the plot shows the first order nature of the phase transition.

Fig. 3.12a shows the structure function plotted in the real space for symmetric phase for $m = 2$. R_x and R_y give the position of the lattices in the real space in Cartesian coordinates. We see that, in this plot the pair correlation function is invariant under $2\pi/3$ rotation since the symmetric phase preserves the rotational symmetry of the system. Fig. 3.12b shows the structure function plotted in the real space for the nematic phase for $m = 2$. In this plot, the structure function is not invariant under $2\pi/3$ rotation since in the nematic phase the rotational symmetry is broken.

The average metric is a multiple of identity in the symmetric phase. In the nematic and the ferri-electric phases it becomes anisotropic, with its principal axis aligned with one of the basis vectors.

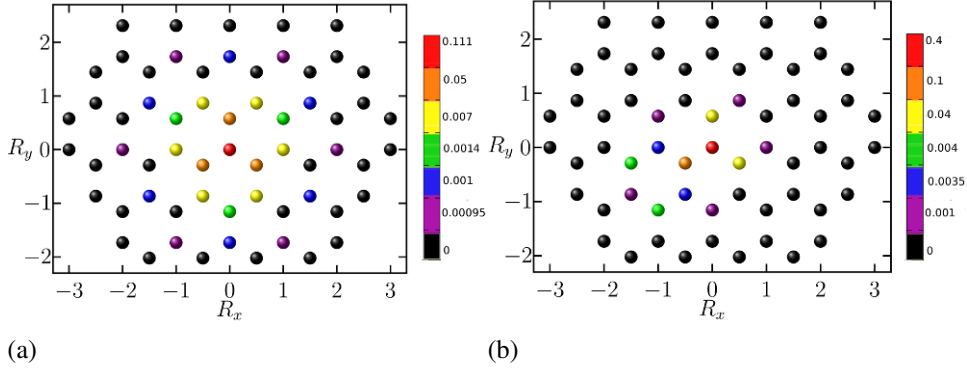


Figure 3.12: Pair correlation function on the lattice in (a) the symmetric phase showing $2\pi/3$ rotation preserved, (b) the nematic phase for $m = 2$ showing $2\pi/3$ rotation broken.

3.7.2 Pancharatnam Berry Curvature

Further, the PBC in the BZ shows the symmetry breaking of the ground state and hence characterizes the phases. The magnetic translation symmetry implies that PBC, $\mathcal{B}_{\mu\nu}(k_1, k_2) = \mathcal{B}_{\mu\nu}(k_1, k_2 + 2\pi/q)$. This feature can be seen in the S phase but is absent in the nematic and the ferrielectric phase, thus reflecting the breaking of the translational symmetry in latter cases. The preservation of inversion symmetry implies $\mathcal{B}_{\mu\nu}(-k_1, -k_2) = \mathcal{B}_{\mu\nu}(k_1, k_2)$. This feature is seen in the symmetric and the nematic phase while is absent in the ferrielectric phase suggesting breaking of the inversion symmetry in the latter case. We plot the PBC in the BZ for $q = 3$ in Fig 3.13, showing the spontaneous breaking of the translational and rotational symmetries for the nematic and the ferrielectric phases and the breaking of inversion symmetry in nematic phase.

Hence, the interaction induced charge ordering leads to various complex phases which break the symmetries of the system. Some of these first order Landau transitions are accompanied by a change in the Hall conductivity. In the following chapter we will discuss the effect of interaction on the Hofstadter butterfly.

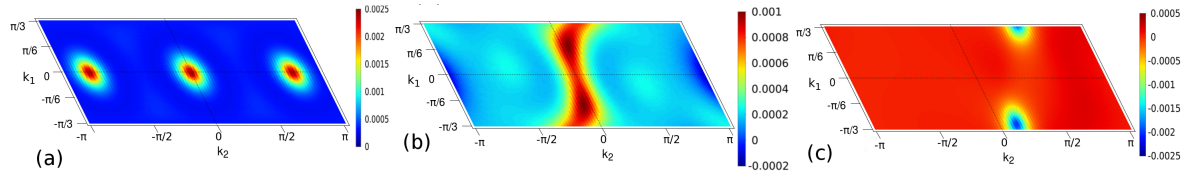


Figure 3.13: Plots for $\mathcal{B}(k_1, k_2)$ in the Brillouin zone for (a) $V = 2 < V_{c1}$ (i.e. S phase) (b) $V_{c1} < V = 3 < V_{c2}$ (i.e. nematic phase) and (c) $V = 7 > V_{c2}$ (i.e. ferrielectric phase). In the symmetric phase, we see $\mathcal{B}_{\mu\nu}(k_1, k_2) = \mathcal{B}_{\mu\nu}(k_1, k_2 + 2\pi/3)$ thus preserving the translational symmetry here which is absent in the nematic and the ferrielectric phase. $\mathcal{B}_{\mu\nu}(-k_1, -k_2) = \mathcal{B}_{\mu\nu}(k_1, k_2)$ for the symmetric phase and nematic phase thus preserving the inversion symmetry here which is absent in the ferrielectric phase.

Chapter 4

Fractal nature of the Hofstadter Butterfly in the presence of interactions

In this Chapter, we discuss the effect of the interactions on the fractal nature of the Hofstadter butterfly [7, 62, 74, 75]. Here we consider all values of flux of the form $\phi/\phi_0 = p/q$ where p, q are integers and are coprime to each other for $q = 3, \dots, 20$. As seen from the previous chapter, for the case where the flux per plaquette is $1/3$, interactions can lead to phases with broken translational symmetry which modify the energy spectrum and change the bandwidth and the band gap. Some of these transitions are also accompanied by the change in the topology of the bands. Here in this chapter, we study the effect of interactions for the cases with values of flux per plaquette of the form p/q and analyze whether such transitions are restricted to $\phi/\phi_0 = 1/3$ or extend to other values of flux. We also study the effects of the interaction induced transition to symmetry broken phases on the fractal structure of the Hofstadter butterfly. This chapter also includes the description of the Landau fan diagram in the presence of interactions and the effect of the topological transitions on it. These analyses are done in order to attempt to answer the question of the effects of interaction on the fractal structure of the Hofstadter butterfly.

To solve this interacting problem, we use mean field approximation discussed in

Chapter 2 and solve the self-consistency equations for a lattice with 30×30 magnetic unit cells by fixing the number of particles. We solve these self consistency equations for the cases of filled bands only.

In this Chapter, we first elaborate on the non-interacting Hofstadter butterfly and then illustrate the effect of interactions on it.

4.1 Hofstadter butterfly of the non-interacting Honeycomb lattice

The fractal structure of the Hofstadter butterfly is a consequence of the combined effect of both the magnetic field and the periodic potential on a 2D electron system such that the two independent length scales: the lattice periodicity and the magnetic length, are comparable. This phenomenon has already been discussed in Chapter 1. The fractal structure of the Hofstadter butterfly is seen when the flux per plaquette is plotted with respect to the single particle energy spectrum of the lattice in the presence of a magnetic field. Fig. 4.1 shows the Hofstadter butterfly for the honeycomb lattice in the absence of interactions. This Hofstadter butterfly can be considered to have two important aspects: the self similarity of the Hofstadter butterfly diagram and the topology at each of the fractal gaps of the Hofstadter butterfly satisfying the Diophantine equation. These topological invariants when plotted with respect to the number of particles per unit cell and magnetic flux per plaquette give the Landau fan diagram. We explain both the plots explicitly below.

4.1.1 Energy-flux plot

The Hofstadter butterfly can be divided into many regions so as to understand its recursive self-similar pattern [62, 66] as done by Hofstadter on the square lattice [2]. For the non-interacting case, the energy spectrum, for any value of flux per plaquette, lies in the range

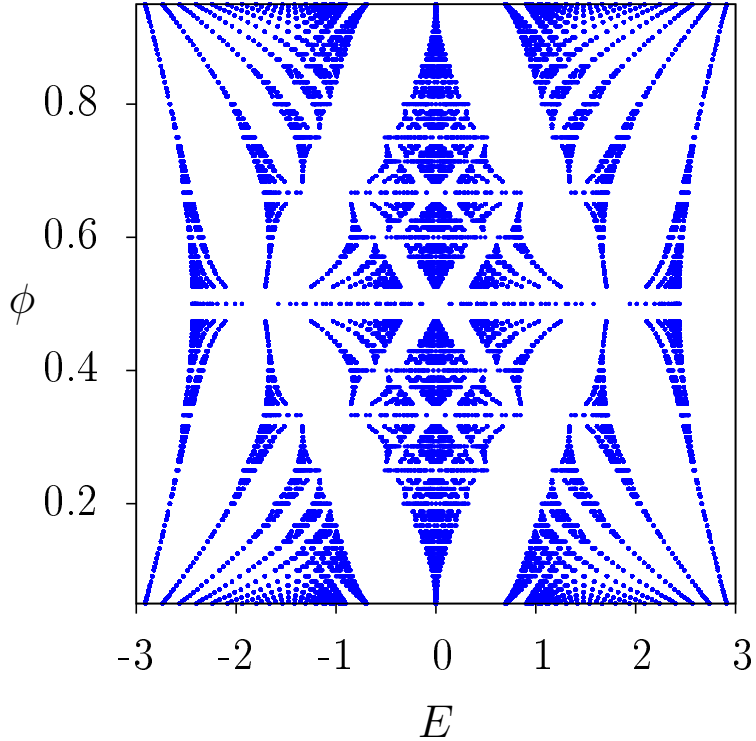


Figure 4.1: Hofstadter butterfly for the honeycomb lattice. Here the x-axis represents the single particle energy E and y-axis is the magnetic flux per plaquette ϕ of form p/q . In this plot $q \leq 20$.

$E \in (-3, 3)$. We consider the plot in Fig. 4.1 as the unit cell.

The unit cell is divided into two regions: the central block denoted C and the side block labeled D , as shown in Fig. 4.2. The block D can be further divided into two blocks M and L . Any portion of the butterfly diagram outside these blocks are the gaps in the energy spectrum and hence there are no states corresponding to these gaps. In Fig. 4.2, we show the subcells in the C block, for example: C block has $\dots, C_{-1}, C_0, C_1, \dots$ subcells. We will see that the whole unit cell lies in each of these subcells of the C block.

To explain this skeleton diagram, we consider values of ϕ of the form $1/q$ and $1 - 1/q$ for $q \geq 2$ as ‘pure cases’ . Here q is an integer. The skeleton of the Hofstadter butterfly, shown in Fig. 4.2, is constructed by joining the energy spectrum corresponding to these particular values of flux per plaquette. The description of the skeleton is given below:

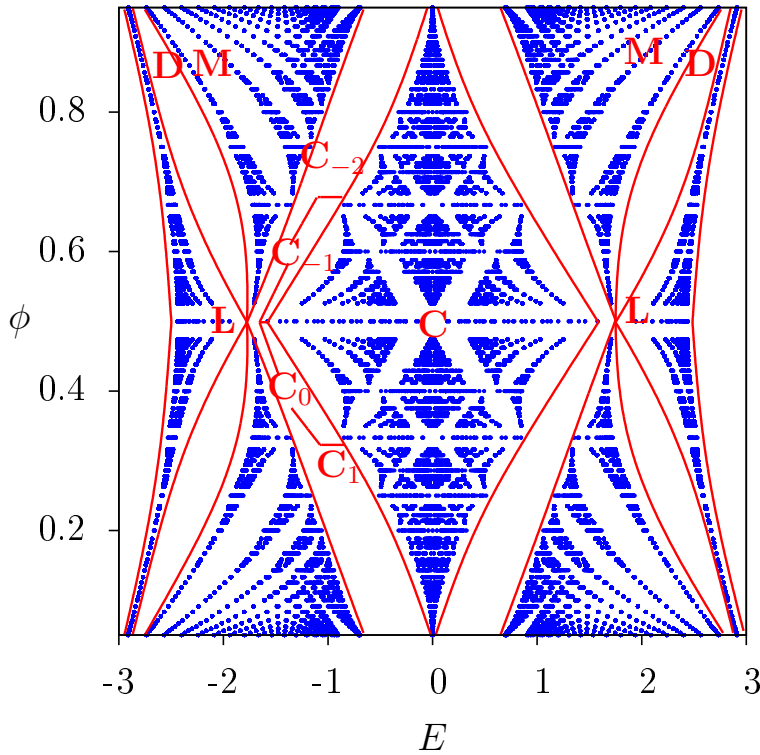


Figure 4.2: The skeleton diagram showing blocks C and D consisting of energy spectrum apart from the central portion. The subcells in the central portion are denoted as $\dots, C_{-1}, C_0, C_1, \dots$.

- Connect the outer edges of q^{th} and $(q + 1)^{th}$ band of neighboring pure cases for $q \leq 2$. This forms a huge box. This box is denoted as the C block.
- Connect the right outer edges of $q - 1^{th}$ band of neighboring pure cases and the left outer edges of the lowest band of neighboring pure cases for $q \leq 2$. This forms a huge box. This box is denoted as the D block.

The whole unit cell in a compressed form and with some rotation is present inside each of the C subcells which can be further divided into subsubcells and again the whole unit cell structure is present inside these subsubcells and this continues. Thus, it gives rise to a self similar fractal like pattern.

We can further find the recursive relation describing the recursive pattern in these subcells. In each of these subcells, there is a local variable defined in terms of the variable

of the parent cell. This local variable behaves like ϕ in the unit cell and the energy spectrum of the unit cell is repeated in these subcells. Therefore, each subcell behaves in the same way as the unit cell and thus the D and C blocks can be constructed in each of these subcells.

Let ϕ be the variable of the parent cell and ϕ' be the local variable in a subcell. Assuming that $\phi \leq 1/2$ and defining N as $N = [1/\phi]$ where $[x]$ stands for the greatest integer less than or equal to x , the recursive relation between ϕ and ϕ' is given by

- $\phi = \frac{1}{N + \phi'}$, in C chain for $\phi \leq 1/2$,
- $1 - \phi = \frac{1}{N + \phi'}$, in C chain for $\phi \geq 1/2$,

Thus, even the local variable ϕ' has values in $[0, 1]$ like the flux in the unit cell.

4.1.2 Landau fan diagram

As mentioned earlier in Chapter 1, each gap in the Hofstadter butterfly can be characterized by two topological invariants (t_r, s_r) which are integers. As per Eq. (1.4), these integers satisfy the Diophantine equation [74, 76]

$$n/n_0 = t_r \phi / \phi_0 + s_r. \quad (4.1)$$

We can also write the Diophantine equation in terms of the r^{th} gap.

$$r = t_r p + s_r q. \quad (4.2)$$

Here r labels the gap and the flux passing per plaquette is $\phi/\phi_0 = p/q$. Number of particles per unit cell, $n/n_0 = r/q$ (see Chapter 1). $t_r e^2/h = -\sigma_H$ where σ_H is the Hall conductivity at the r^{th} gap and s_r is the change in the electron density when there is an adiabatic change in the periodic potential [76]. The plot of the Hall conductivity

with respect to the number of particles per unit cell and the magnetic flux passing per plaquette is called the Landau fan diagram. Fig. 4.3 shows the Landau fan diagram for the non-interacting case.

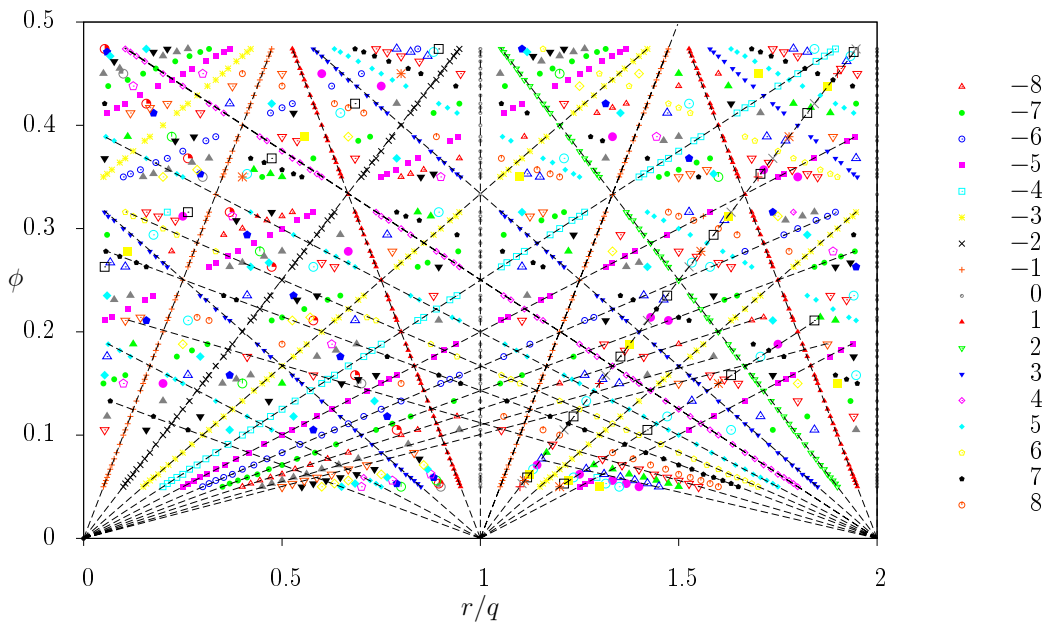


Figure 4.3: Landau fan diagram for the non-interacting case. In this figure the colorbar is restricted to values from -8 to 8 for convenience in plotting. This Landau fan diagram is for $q \leq 20$.

In Fig. 4.3, the points with the same Hall conductivities can be joined to give a straight line which when extrapolated meets the x-axis at an integer point. This intercept which is an integer gives the value of s_r whereas the slope gives the value of t_r . In this figure the colorbar is restricted to values from -8 to 8 for convenience in plotting though the maximum value of Chern number can be very high depending on the maximum value of q .

4.2 Non-interacting Hofstadter butterfly for

$$q \leq 20$$

We have solved the interacting problem for $q \leq 20$. In this section, we will show that this range of q in the non-interacting case is sufficient enough to have a basic idea of the fractal structure of the Hofstadter butterfly and see the self similarity in the plot atleast for one recursion.

4.2.1 Energy-flux diagram

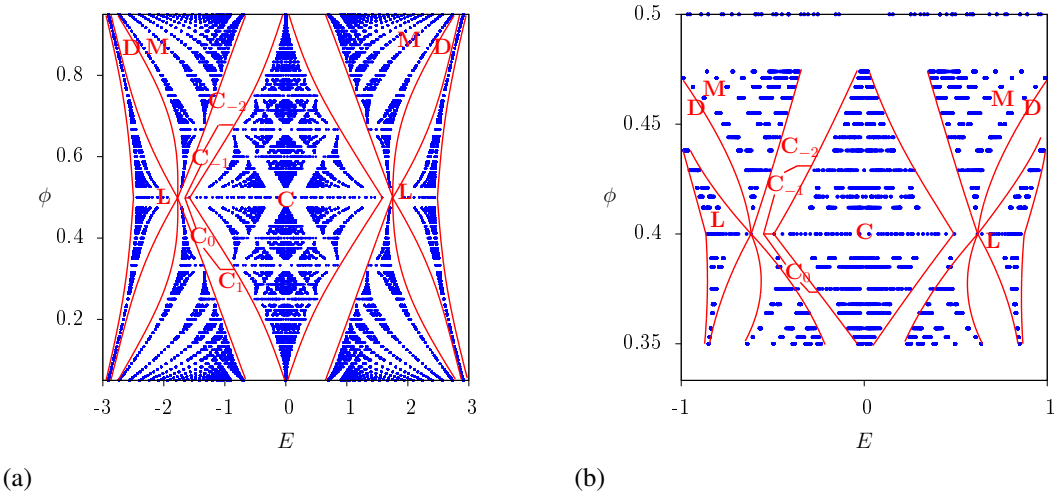


Figure 4.4: Hofstadter butterfly for the honeycomb lattice where the energy spectrum is plotted for the flux per plaquette in the range (a) $(0, 1)$ and (b) $(1/3, 1/2)$. Fig. 4.4b is the plot of the Hofstadter butterfly in C_0 subcell.

To further understand the self-similarity of the Hofstadter butterfly, let us consider the C_0 subcell with flux ϕ in the range $(1/3, 1/2)$. In this subcell, we can construct C block and the side block D of the energy bands as can be seen in Fig. 4.4b. Fig. 4.4a is the Hofstadter plot for the flux per plaquette of form p/q and $q \leq 20$ showing the C block and the side block D . Fig. 4.4b shows the Hofstadter plot in the C_0 subcell of Fig. 4.4a with the flux per plaquette in the range $(1/3, 1/2)$ showing the C block and the side block

D. Here, using the recursive relations discussed for C block, we see that inside the C_0 subcell, $\phi'/\phi_0 \in (0, 1)$. For example, for $\phi = 2/5$, $\phi' = 1/2$; $\phi = 3/7$, $\phi' = 1/3$; $\phi = 3/8$, $\phi' = 2/3$ and so on. In Fig. 4.4b, we see that in the C_0 subcell, the energy spectrum has four bands for flux $\phi'/\phi_0 = 1/2$, six bands for flux $\phi'/\phi_0 = 1/3$ and so on for other values of flux ϕ'/ϕ_0 . The band gaps are positioned in a similar fashion as the unit cell in Fig. 4.4a. Hence, the energy spectrum of the unit cell can be seen to be repeating in the subcell. To further seeing the recursion inside these subcells and finding the whole unit cell inside the subcell, we need to plot the Hofstadter butterfly for even lower values in flux per plaquette with larger value of q . For the limit of flux considered with $q \leq 20$, the Hofstadter butterfly diagram gives the basic idea that the recursive relation is valid and we get a self-similar fractal structure.

4.2.2 Landau fan diagram

The second aspect of the Hofstadter butterfly i.e. the topological invariants characterizing the fractal and obeying the Diophantine equation can easily be seen for any value of q . Fig. 4.3, shows the non-interacting Landau fan diagram for $q \leq 20$.

Here as discussed before, the slope of the straight lines give the value of t_r . The intercepts of these lines are integers which give the values of s_r . In this figure the colorbar is restricted to values from -8 to 8 for convenience in plotting though the maximum value of total Chern number of bands filled is 18 . Hence, $q \leq 20$ is enough to show and analyze the Landau fan diagram and realize that these topological invariants indeed satisfy the Diophantine equation.

4.3 Hofstadter Butterfly in the presence of interactions

The interacting problem, as mentioned earlier, is solved using mean field approximation here. As seen in previous Chapter, there are two types of magnetic unit cell choices for $q = 3$. On increasing q , the number of magnetic unit cell choices increases and hence is difficult to consider all the choices and solve the self consistency equations for $q \leq 20$. For the non-interacting case, when the translation symmetry is not broken, the choice of unit cell is irrelevant. For the interacting case, the choice of unit cell matters. It determines the pattern of the translation symmetry breaking. With increasing q , the number of distinct magnetic unit cell choices increase and it is not feasible to solve all the possibilities numerically. Here we assume the unit cell choice to be the linear choice i.e. unit cell choice **I** and solve the self consistency equations for this choice for the cases of fully filled bands. There could be phases with other patterns of translation symmetry breaking with lower energy and they could appear at lower values of the interaction strength. Our analysis thus underestimates the effects of the interactions.

4.3.1 Hofstadter butterfly in symmetric phase

As discussed before, there is always a scaling solution satisfying the self consistency equations and when the energy of this mean field solution is the lowest, we find the system in the symmetric phase. Fig. 4.5 shows the Hofstadter butterfly in the symmetric phase when the energy is restricted to half-filling. Due to particle hole symmetry, the other half of the energy- flux plot is just the mirror reflection of this plot. In this phase, the single particle energies just get scaled. But, these scalings are not uniform and depend on the bands filled. However, the band gap never closes and from Fig. 4.5 we see that the whole fractal structure of the Hofstadter butterfly remains intact. The recursive relations for the non-interacting case still remain valid for the symmetric phase. The plot can be divided into subcells in the C and D blocks in the energy spectrum in a similar

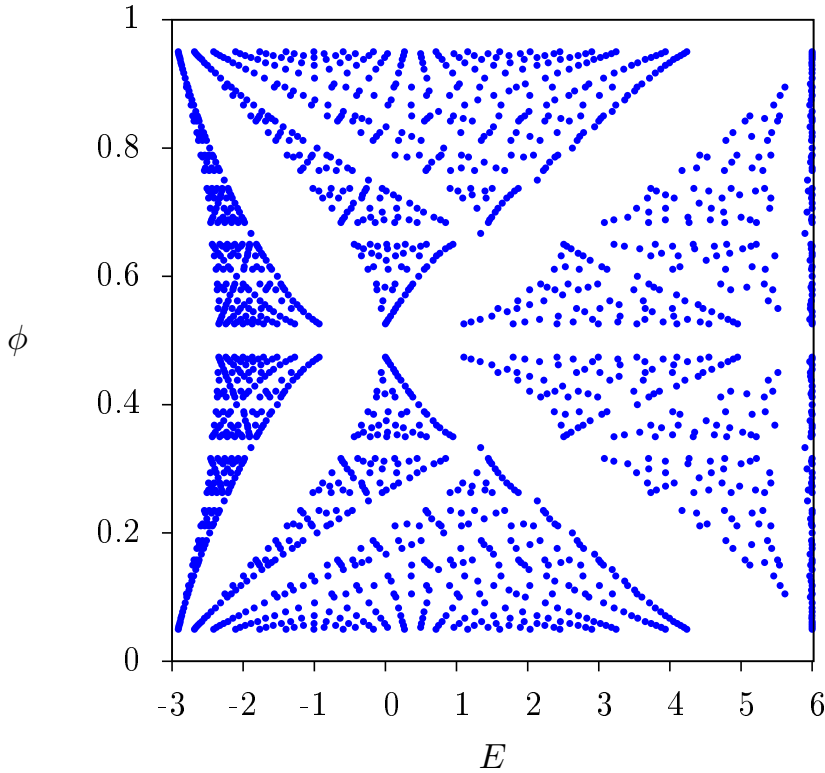


Figure 4.5: Hofstadter butterfly for the honeycomb lattice in the symmetric phase. Here the energy spectrum is plotted only till half filling.

fashion as discussed in the non-interacting case. The recursive relation in the C block is $\phi = \frac{1}{N + \phi'}$ for $\phi \leq 1/2$, and the C block is $\phi = \frac{1}{N + \phi'}$ for $\phi \geq 1/2$. The energy spectrum similar to the unit cell in the Hofstadter plot is seen in each of the subcells of the Hofstadter butterfly for the symmetric phase.

As the ground state of the symmetric phase is same as that of the non-interacting case, the Hall conductivity at each fractal gap is the same as that of the non-interacting case. Therefore, the Landau fan diagram remains completely unchanged in the symmetric phase.

4.3.2 Effect of interactions on the Hofstadter butterfly

Here we have solved the self consistency equations for the interaction strength $V = 1, 2$ and $V = 4$ and find the ground state of the system with different values of flux per

plaquette of the form $\phi = 2\pi p/q$.

As we solve the self consistency equations only for the cases of filled bands, to understand the effect of the interactions on the Hofstadter butterfly, we must plot the magnetic flux per plaquette with respect to the maximum energy of the band for the non-interacting case and if this plot shows the self-similar structure then we can compare it with the interacting case and study the effect of the interactions on the fractal structure of the Hofstadter butterfly. The self consistency equations are solved only for filled bands upto half filling since the remaining empty bands in the upper half when filled will give the same solutions for the self consistency equations as the lower half due to particle hole symmetry.

Fig. 4.6a is the plot for flux per plaquette versus the maximum energy of each band for the non-interacting case. The plot is restricted to half-filling here. As can be seen

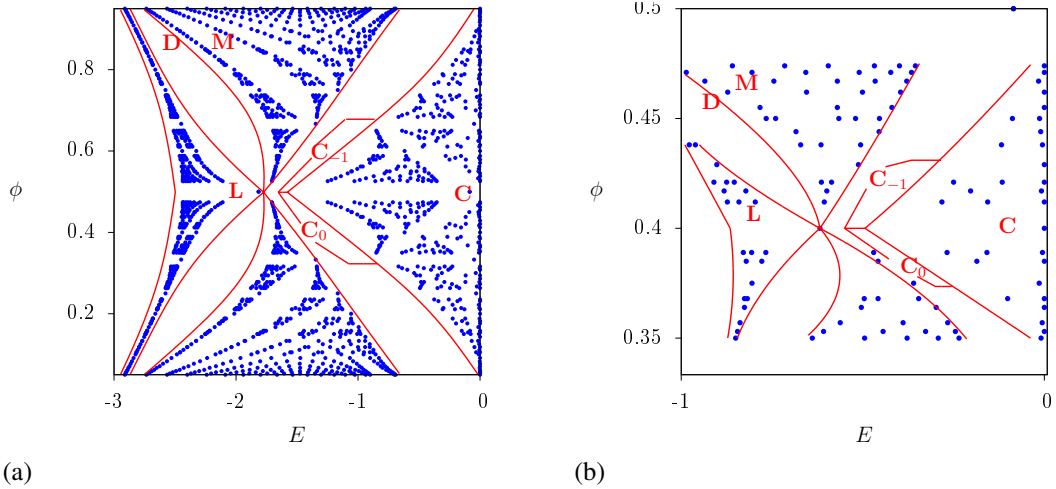


Figure 4.6: Hofstadter butterfly for the honeycomb lattice in the absence of interaction plotted by taking the maximum energy as the x-axis instead of the whole energy spectrum for (a) flux in the range $(0, 1)$ and the maximum energy plotted till half-filling. (b) flux in the range $(1/3, 1/2)$ and maximum energy in the range $[-1, 1]$.

from Fig. 4.6a, the recursive relation for the non-interacting case with the full energy spectrum is also valid for the Hofstadter butterfly plot with maximum energy. Fig. 4.6b is the plot of the Hofstadter butterfly in the absence of interaction for the flux in the range $(1/3, 1/2)$ in the C_0 of the C block. We see that the unit cell of the Hofstadter butterfly

with C and D blocks are reflected here.

Now we study the effect of the interaction on Fig. 4.6a. The plot for flux per plaquette versus the maximum energy of each band is given by Fig. 4.7a for $V = 1$, Fig. 4.7c for $V = 2$ and Fig. 4.7d for $V = 4$. As seen from Fig. 4.7a and Fig. 4.7b, for $V = 1$, the fractal structure is almost preserved except at the end of the plot. But for $V = 4$, a larger portion of the fractal structure has been destroyed compared to $V = 1$ as seen from Fig. 4.7d. The fractal nature of the Hofstadter butterfly disintegrates and we don't find any self-similar recursive relation in Fig. 4.7. In the presence of interactions, we see that the recursive relation valid for non-interacting case is no more valid. Hence, the fractal nature of the Hofstadter butterfly diagram is erased out.

The disintegration of the fractal structure can be understood as a result of the transition to the phases with broken translational symmetry. The bandgap and the bandwidth change and hence is reflected in the change in the positions of the fractal gaps in the Hofstadter butterfly. As the interaction strength increases more number of phase transitions are seen and hence larger amount of the fractal structure is erased out. This results in the non-validity of the recursive relation in Fig. 4.7.

4.3.3 Effect of interaction on the Landau fan diagram

Further, the effect of these phase transitions due to the interaction can be studied from the Landau fan diagram shown in Fig. 4.8. Fig. 4.8a is the Landau fan diagram in the presence of interaction of strength $V = 1$, Fig. 4.8b is the Landau fan diagram in the presence of interaction of strength $V = 2$ and Fig. 4.8c is the Landau fan diagram in the presence of interaction of strength $V = 4$. In Fig. 4.8a, though most of the points with the same Hall conductivities can be joined in a straight line but there are some points in this line which have different Hall conductivities. But in Fig. 4.8c, the points with the same Hall conductivities cannot be joined to form a straight line as most of the points are

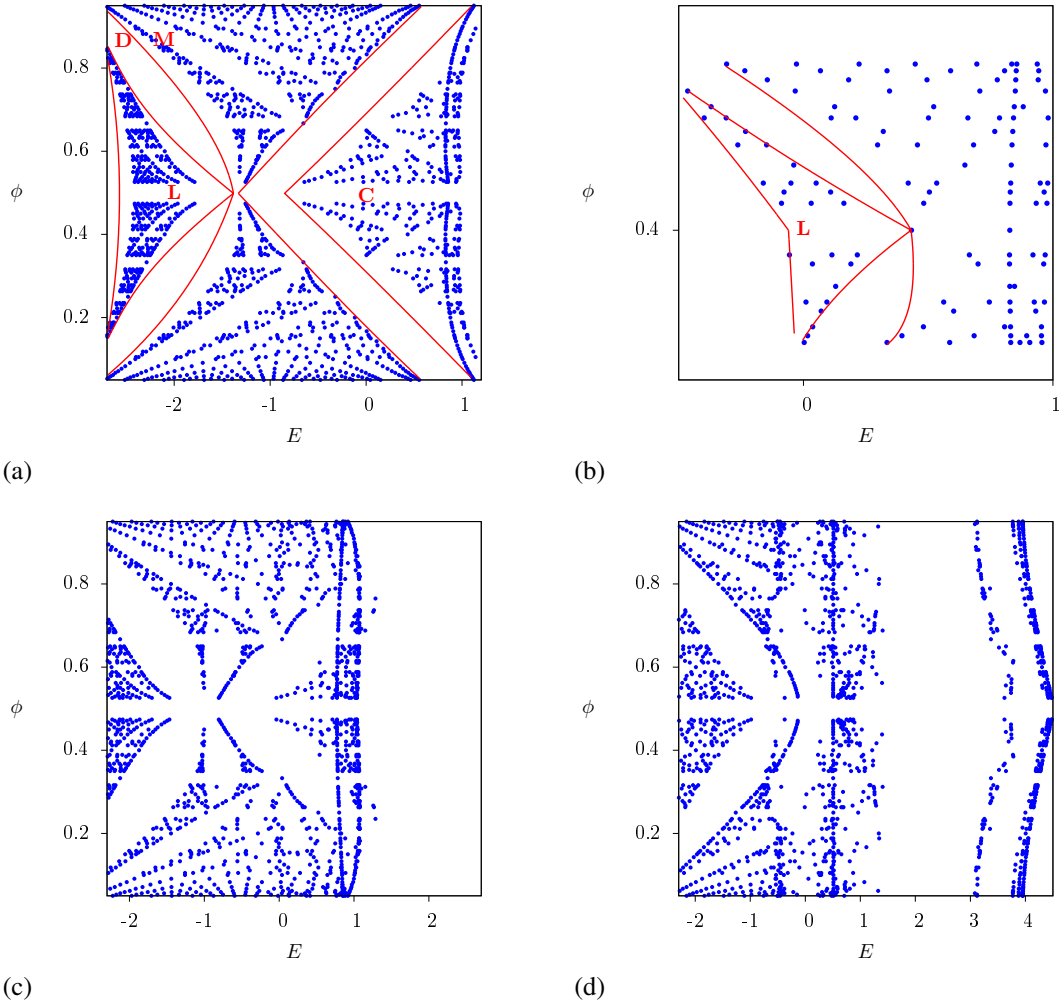


Figure 4.7: Hofstadter butterfly for the honeycomb lattice in the presence of interaction plotted by taking the maximum energy as the x-axis for the flux in the range $(1/20, 19/20)$ for (a) $V = 1$, (c) $V = 2$ and (d) $V = 4$. (b) Hofstadter butterfly for the honeycomb lattice in the presence of interaction plotted by taking the maximum energy as the x-axis for the flux in the range $(1/3, 1/2)$ for $V = 1$. The maximum energy is plotted till half-filling

scattered. This is due to the topological transition accompanied with the Landau phase transitions. Thus, Fig. 4.8 suggests that more number of topological transitions are seen as the interaction strength is increased. The maximum value of the Hall conductivity considering all filled bands for all values of flux per plaquette of the form p/q with $q \leq 20$, decreases with the increase of interaction strength. For example, in the absence of interactions, the maximum value of the Hall conductivity is $18e^2/h$, while for case of

$V = 1$ it is $15e^2/h$ and for $V = 4$ the maximum value of the Hall conductivity is $8e^2/h$.

Here we just plot the Hall conductivities for bands with non-trivial topology i.e. removing the points with zero Hall conductivity. We can see that most of the region near half filling have a topological transition as shown in Fig. 4.8. From Fig. 4.8, we see that the portion of the Landau fan diagram with zero Hall conductivity increases with increase in the interaction strength. Hence, from Fig. 4.8, it is clear that the region of the fractal structure erased out increases as the interaction strength is increased i.e. more number of phase transitions to translational and rotational symmetry broken phases is seen as the interaction strength is increased. These Landau transitions are accompanied by topological transitions suggesting the absence of the signal of fractal structure in the Landau fan diagrams. In addition, on using the same Diophantine equation as for the non-interacting case, s_r no longer remains an integer. For example, for $V = 4$ and $r = 2$, $t_2 = 0$, so $s_2 = 2/3$. Hence, the Diophantine equation used for the non-interacting case is no more valid in the presence of interactions.

Thus, we see that the phase transition to a translational and rotational symmetry broken phase is not just restricted to the flux $1/3$ rather is present for other rational values of the flux too. The translational and rotational symmetry breaking leads to variation in the energy spectrum of the system by changing the band gap and band width. This change in the energy spectrum is reflected in the Hofstadter butterfly where the recursive relations are no longer valid and the fractal structure disintegrates gradually as the interaction strength is increased. Many of these phase transitions are also accompanied with the change in topology which is reflected in the Landau fan diagram. Therefore, both the energy-flux plot and the Landau fan diagram suggest that the fractal structure gets erased out gradually in the presence of interactions and the amount of the fractal structure erased increases with the interaction strength.

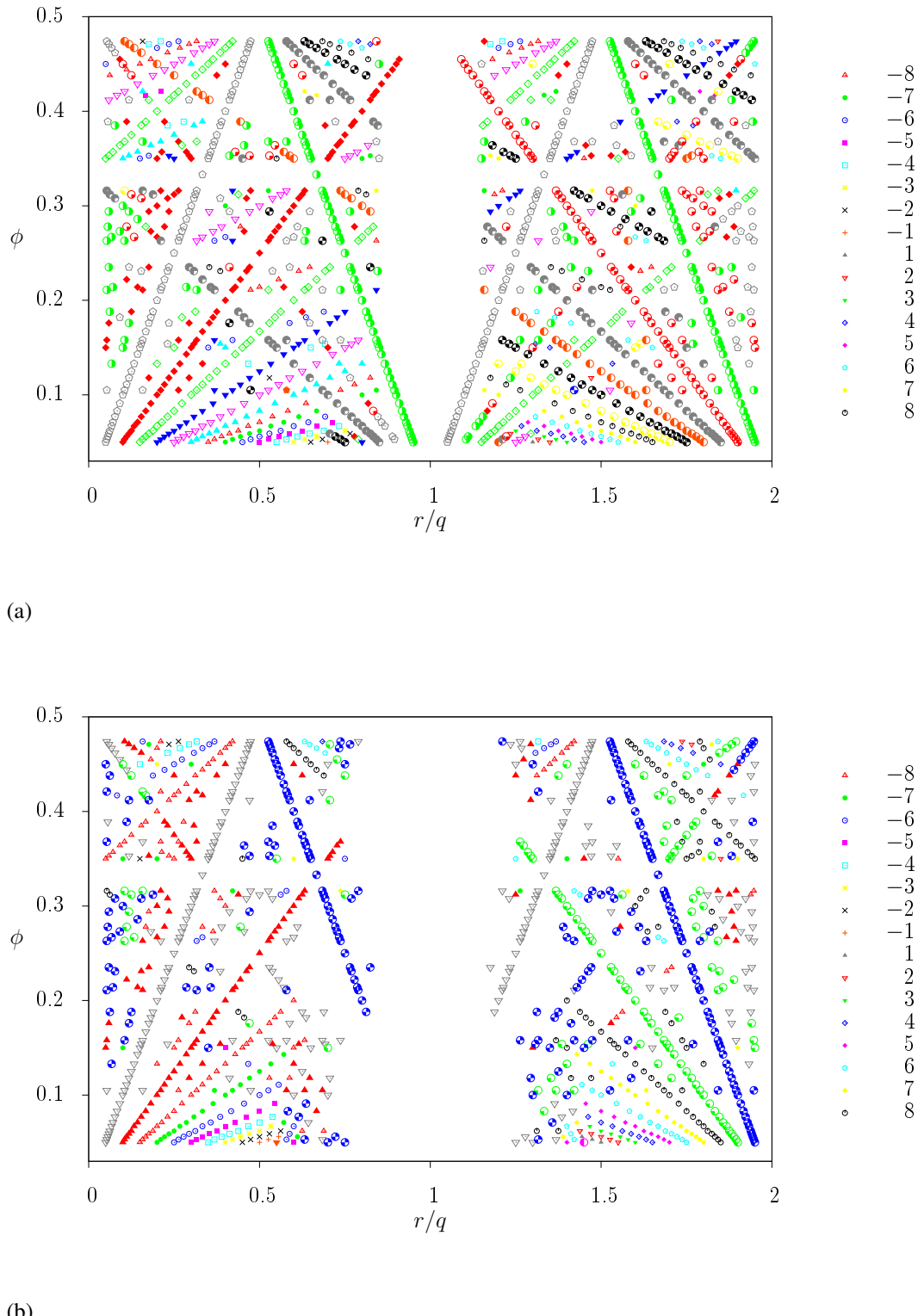
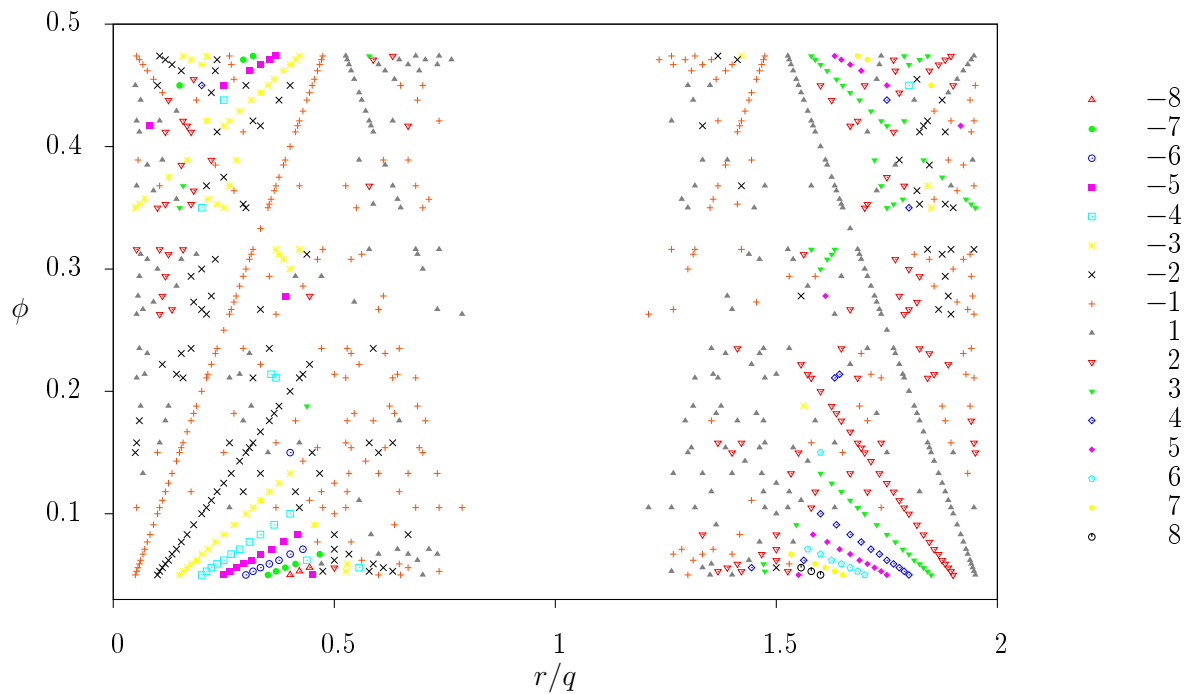


Figure 4.8: Landau fan diagram in the presence of interaction after removing the points where the Hall conductivity is zero for interaction strength (a) $V = 1$, (b) $V = 2$ and (c) $V = 4$.



(c)

Figure 4.8: Landau fan diagram in the presence of interaction after removing the points where the Hall conductivity is zero for interaction strength (a) $V = 1$, (b) $V = 2$ and (c) $V = 4$.

Chapter 5

Signal of Pancharatnam Berry curvature: Rotating condensates

In this Chapter we propose a method of detecting the Pancharatnam Berry (PB) curvature in optical lattice systems using time of flight experiments. Previous works [77–79] have suggested various ways to probe the PB curvature but the method suggested here is different from these works.

The PB curvature characterizes how the phase of the single-particle wave functions twist over the BZ. The semiclassical Sundaram-Niu equations [22, 30] provide a clear physical interpretation of PB curvature as a magnetic field in momentum space. In the presence of an external force, this field induces the so-called anomalous velocity perpendicular to the external force. This leads to a Hall conductance even in the absence of an external magnetic field, a phenomenon dubbed the anomalous Hall effect [21]. The value of the Hall conductance is equal to the PB curvature field integrated over the occupied states.

5.1 Probing the PB curvature

A model Hamiltonian, H , in an optical lattice experiment is given by Eq. (5.1). At time $T = 0$, the model Hamiltonian in the presence of a harmonic trap is given by

$$\mathcal{H}_0 = H + \sum_i (\gamma_x x_i^2 + \gamma_y y_i^2) n_i \quad (5.1)$$

Here γ_x and γ_y are the strengths of the harmonic trap in the \hat{e}_1 and \hat{e}_2 directions (the basis vectors of the lattice), while x_i and y_i represent the spatial coordinates of the i^{th} lattice site which are measured in terms of the lattice parameter a .

Using time of flight experiments which are the standard methods of imaging in optical lattice systems, the density profiles of the atomic cloud is studied. Here, all the external potentials are switched off suddenly following which the atomic cloud is allowed to expand ballistically, the atoms now behaving as free particles. Images of the cloud at various intervals of time show how the density distribution changes as the cloud expands. If the system initially had non-zero PB curvature, then the cloud rotates along with expanding thereby providing a mean to probe the PB curvature. To understand the density profiles we first review the Sundaram-Niu[30] equations (SNE) and then the Thomas-Fermi approximation [6] for a many-fermion system to address the problem of rotating condensates.

The Sundaram-Niu equations [30] govern the classical dynamics of a wave packet restricted to the band with width in momentum space small compared to that of the BZ and width in real space small compared to the applied external field. These wave packets therefore have a width in real space that is large compared to the lattice spacing but small compared to the scale of the variation of the external fields. The equation of motion of

the Bloch electron for two dimensional systems in the absence of a magnetic field are

$$\dot{x}^i = \frac{1}{\hbar} \frac{\partial \epsilon(k)}{\partial k_i} + \mathcal{B}(k) \epsilon^{ij} \dot{k}_j \quad (5.2)$$

$$\hbar \dot{k}_i = - \frac{\partial V(x)}{\partial x^i} \quad (5.3)$$

where $\epsilon(k)$ is the energy in the absence of external fields, $\mathcal{B}(k)$ the PB field, V the external potential and ϵ^{ij} is the Levi civita symbol. Thus $\mathcal{B}(k)$ induces a force-dependent anomalous velocity.

The Sundaram-Niu equations describe the wave-packet dynamics for a single particle. In optical lattice experiments, the many body dynamics of the atoms need to be considered for which we use the Thomas-Fermi approximation. This approximation assumes that the ground state is described by a phase-space particle density that incorporates the Pauli exclusion principle. The number of fermions in a phase-space volume $d^2x d^2p$ around the point (x, p) , $\tilde{\rho}(x, p)$, can be written as

$$\tilde{\rho}(x, p) = \frac{1}{(2\pi\hbar)^2} \Theta(\epsilon_F - h(x, p)) \quad (5.4)$$

where ϵ_F is the Fermi energy level and $h(x, p)$ is the single particle Hamiltonian given by

$$h(x, p) = \epsilon(p) + V(x). \quad (5.5)$$

The initial particle density of the cloud can be calculated from Eq.(5.4). We now allow the cloud to expand freely and by using time of flight experiments the density at various times can be computed using Liouville's theorem.

The Thomas-Fermi approximation can be extended to multiple bands if the bands are well separated and if the applied external potential varies slowly enough to prevent interband transitions. Thus, the total phase space density is the sum of the phase space

densities for first band and second bands. Additionally the Thomas-Fermi approximation fails when there are Dirac points in the system.

The above formalism can be applied to multi-band model where the bands are well separated. Here we consider a model Hamiltonian, Kitaev Hubbard model, and the results are discussed in the following section.

5.2 Kitaev Hubbard Model

The model Hamiltonian [80, 81] is

$$\mathcal{H} = - \sum_{\langle ij \rangle} C_{i\sigma}^\dagger \frac{(tI + t'\sigma^\alpha)_{\sigma\sigma'}}{2} C_{j\sigma'} + h.c. \quad (5.6)$$

describes a system of fermions on the honeycomb lattice. i labels the sites of the honeycomb lattice, σ the spin and α the nearest neighbor link. There is a spin-independent hopping term with strength t and a time-reversal breaking, spin-dependent hopping with strength t' . By diagonalizing the single particle Hamiltonian in the momentum space, we get the energy spectrum shown in Fig. 5.1 for $t' = 0.5t$ and Fig. 5.2 for $t' = t$. These energy bands have non-trivial topology. For well separated bands, the Hall conductivity, σ_H , for the lowest band is $-e^2/h$ and at half filling $\sigma_H = 0$. From particle hole symmetry, the Hall conductivities when three bands are filled is $\sigma_H = -e^2/h$ and when all the bands are filled, $\sigma_H = 0$. The second and third bands touch at the Dirac points. To calculate the Hall conductivities at half filling, we break the inversion symmetry by adding a staggered mass term to open up the gaps at these Dirac points. A scheme to realize the spin-dependent hopping in cold atom systems was proposed by Duan et al [82] by considering ^{40}K atoms to form an atomic cloud in the optical lattice.

The formalism described in the previous section to probe the PB curvature is applied to this model but with broken inversion symmetry to avoid the degeneracy due to Dirac

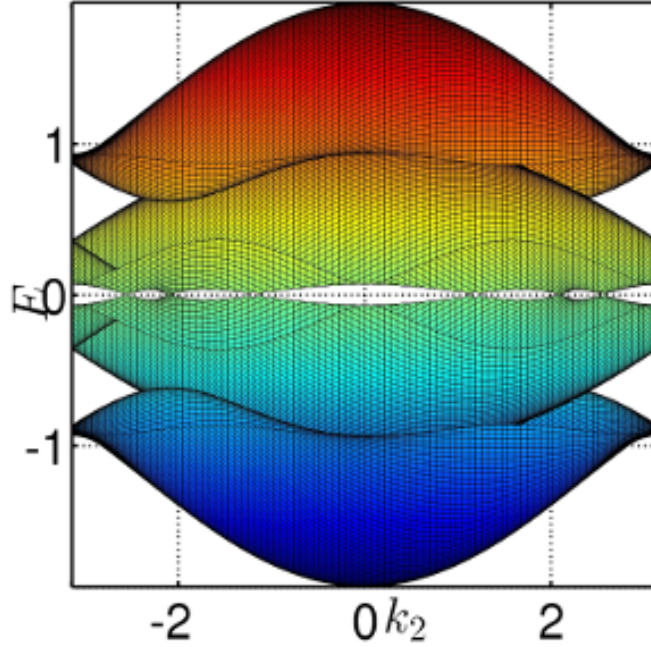


Figure 5.1: Plot for energy $E(k_1, k_2)$ vs k_2 for $t' = 0.5t$.

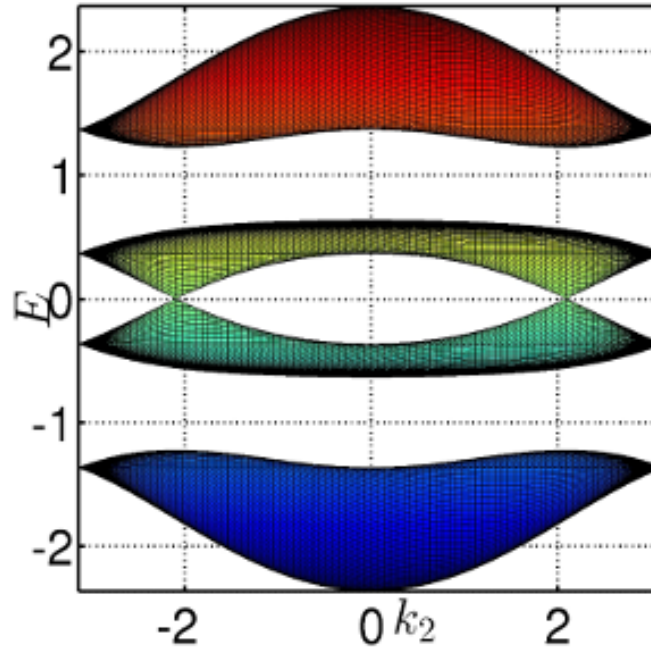


Figure 5.2: Plot for energy $E(k_1, k_2)$ vs k_2 for $t' = t$.

points. A slowly varying external potential is applied. We use the same parameters as in [83]. The system is confined by a rotationally invariant external harmonic potential

$V(R)$, where

$$V(R) = \gamma_x X^2 + \gamma_y Y^2 \quad (5.7)$$

and $\gamma_{x,y} = m\omega_{x,y}^2\lambda^2/6$ and X, Y are the dimensionless spatial coordinates of the lattice sites. Here $\lambda = 1064$ nm is the wavelength of the laser beam, $\omega_x = \omega_y = 40\pi$ rad/s is the trapping frequency of the potential, m is the mass of the ^{40}K atoms and $t/h = 580$ Hz is the nearest neighbour hopping parameter. A staggered mass term $W/h = 0.1$ Hz is added. The Hamiltonian is

$$\begin{aligned} \mathcal{H}_0 = & - \sum_{\langle ij \rangle} C_{i\mu}^\dagger \frac{(tI + t'\sigma^\alpha)_{\mu\nu}}{2} C_{j\nu} + \frac{W}{2} \sum_{i \in A} n_i \\ & - \frac{W}{2} \sum_{i \in B} n_i + \sum_i (\gamma_x x_i^2 + \gamma_y y_i^2) n_i \end{aligned} \quad (5.8)$$

The formalism is applied for $t' = 0.5t$ and $t' = t$.

From Eq. 5.4 and Eq. 5.5, we calculate the number density of the cloud with distance R . Fig. 5.3 shows the variation of the number density of the cloud with distance R for

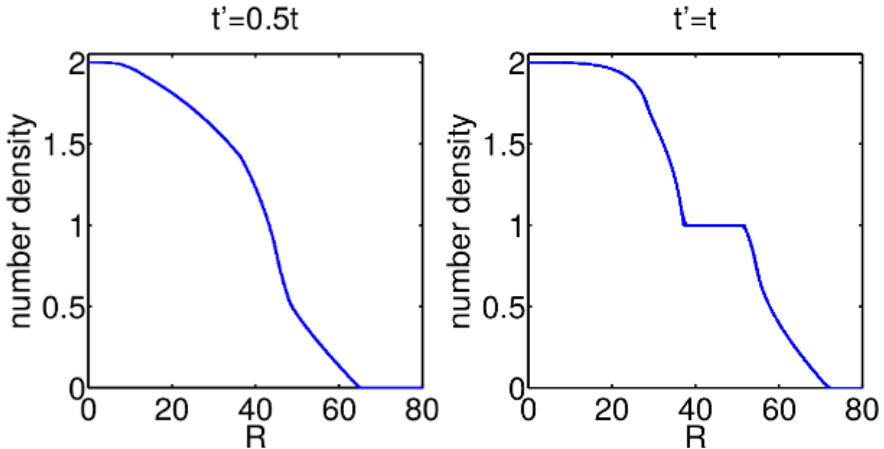


Figure 5.3: Particle density plot as a function of R for $t' = 0.5t$ and $t' = t$.

both $t' = 0.5t$ and $t' = t$. At $R = 0$ it reaches a maximum since the trap potential is zero there. Away from $R = 0$, the total energy of each of the bands increases by

$V(R)$, reducing the number of occupied states lying below $\mu = 0$ and thus decreasing the density. For $t' = t$, there is a plateau where the density has a constant value of 1 as seen in Fig. 5.3. The plateau occurs due to the energy gap between the first and the second band. The size of the plateau decreases depending on the size of the gap between the two bands. Below $t' = 0.717$, the first and the second bands overlap and hence we see a continuous change in the density as seen from the plot for $t' = 0.5t$.

In Fig. 5.4, we see that the PB phase of the occupied bands is zero at the center $R = 0$, since the Chern number of the contributing bands are equal and opposite. Away from the center the trap potential reduces the number of occupied states below $\mu = 0$, decreasing the PB phase as a consequence. A minima is reached when the only contributing band is the lowest band after which the PB phase increases and reaches a value of zero when all the bands are empty. For $t' = t$, the PB phase also shows a plateau similar to that of the density whereas for $t' = 0.5t$ the PB phase changes continuously. For $t' = t$, there are kinks where the PB phase is lesser than -1 and greater than 0 . The kink appears because

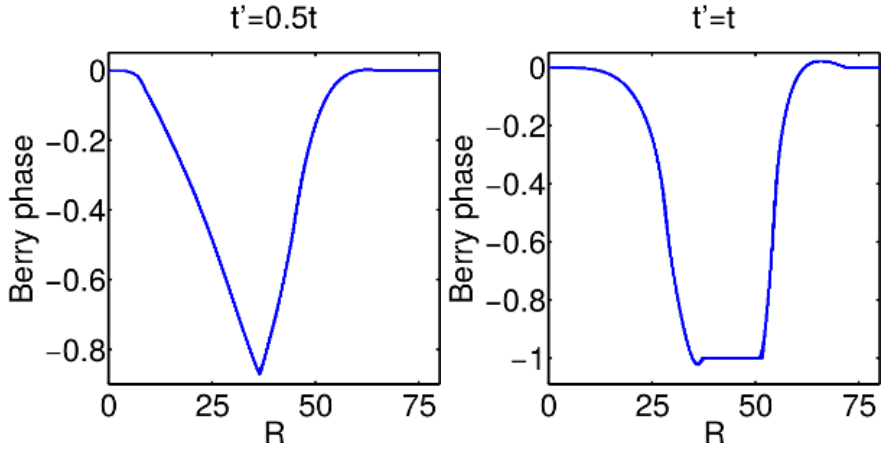


Figure 5.4: (color online) PB phase as a function of R for $t' = 0.5t$ and $t' = t$.

the PB phase of the band is not entirely positive when the Chern number is $+1$ and vice-versa. To illustrate this we plot, in Fig. 5.5, the PB phase of first band as a function of the filling factor.

From the Thomas Fermi approximation, the velocity of the cloud can be computed

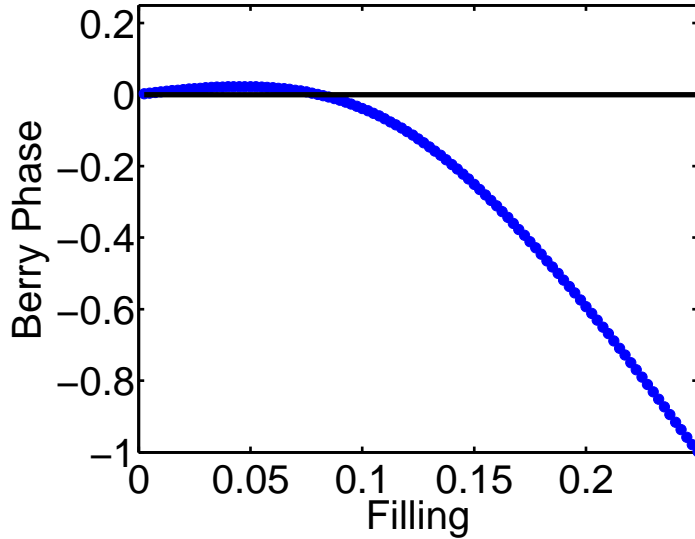


Figure 5.5: PB phase as a function of filling for $t' = 1$. The PB phase is not negative for all values of the filling. For some values it is positive reflecting that the PB curvature of the band takes both positive and negative values.

and is shown in Fig. 5.6. The velocity is zero where the PB phase is zero. The direction of the velocity at the boundary changes due to the change in the sign of the PB phase as shown in Fig. 5.5. From the velocity, the total angular momentum density per particle L

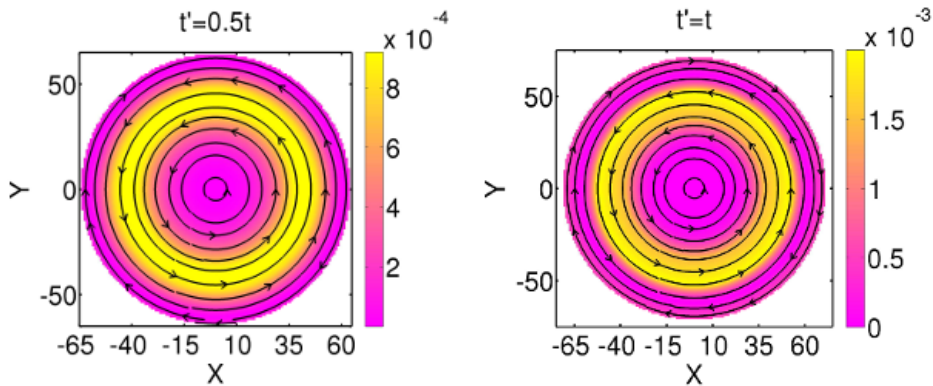


Figure 5.6: Velocity vector measured in m/s as a function of X and Y for $t' = 0.5t$ and $t' = t$.

can be computed and is found to be $\approx 12\hbar$ for $t' = t$ and $\approx 6\hbar$ for $t' = 0.5t$. This value is large compared to the value obtained in bosonic optical lattice experiments [84], and thus should be observable in such experiments.

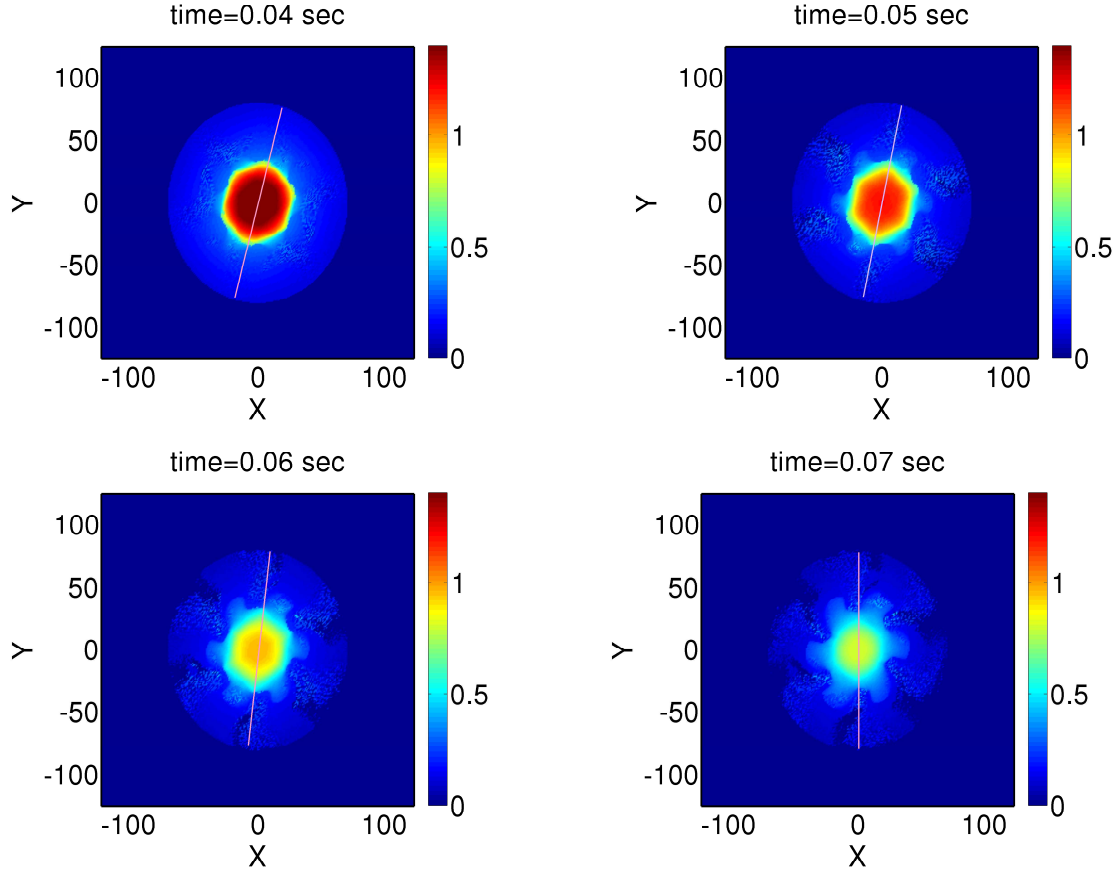


Figure 5.7: Density profiles as a function of X, Y for $t' = t$ at different times. Lines are drawn in the above figures to show the rotation of the cloud as a function of time due to non-zero PB curvatures.

The evolution of the cloud density after the traps have been switched off can be computed using Liouville's theorem. At various times the cloud rotates as it expands as seen in Fig. 5.7. This rotation is a signal of non-zero PB curvature. The cloud also inherits the hexagonal structure of the underlying honeycomb lattice as it expands [81].

Chapter 6

Summary and Conclusion

In this thesis, we have studied the effect of interactions in the Hofstadter regime of the honeycomb lattice. Our results show that interactions induce interesting and complex phases in the Hofstadter regime of the honeycomb lattice. To summarize our results, we show that the nearest neighbor repulsive interaction induces a charge ordering, as we intuitively expect. At strong interactions, translation symmetry broken phases with anisotropic charge distributions become energetically favorable. The anisotropy in the particle density can be characterized by quadrupole and dipole moments.

The first order transition, for filling $m = 1, 2$, from the symmetric to the nematic phase is accompanied with a change of topology which is reflected in the change in the Hall conductivity. Though the Hall conductivity is zero in the nematic phase, for the $m = 2$ filling, the filled bands individually have non-trivial topology with non-zero Chern number. Some insight for the mechanism of this transition comes from examining the magnitudes of the bond order parameters, $\chi_{\langle \alpha a, \beta b \rangle}$. The 2D lattice looks like a set of weakly coupled 1D ribbons or clusters. In the extreme limit of decoupled ribbons, the Chern number is zero and hence will remain so for weak coupling as well. So a Chern number change accompanies the first order nematic transition when the weakening is significant.

Chapter 6. Summary and Conclusion

The anisotropy and the spatial extent of the pair correlations are characterized by the quantum metric averaged over the BZ. Nematic phases in homogeneous quantum Hall systems have previously been theoretically studied [43–46] and experimentally observed [47–49] in fractional quantum Hall systems. Our results show that they occur in the Hofstadter regime also. This motivates us to investigate the structure of the anisotropic phases by studying pair correlations from the point of view of the quantum geometric approach to insulating states [24]. The shape and the extent of the pair correlations can be exactly related to the quantum metric in the momentum space [24], averaged over the Brillouin zone (BZ) [73]. We give an alternate proof of the relation between momentum space quantum metric and the pair correlation function on the lattice system. This result relates the momentum space quantum metric of systems in a periodic potential to the real space metric introduced by Haldane [44] in homogeneous quantum Hall systems.

We have further studied the effect of interactions on the fractal structure of the Hofstadter butterfly which is understood as arising from the interplay between the two independent length scales, the lattice periodicity and the magnetic length. We have shown that the interaction induces charge ordering which breaks the translational symmetry and thus changes the periodicity. The energy-flux plot shows that the fractal structure gets gradually erased out as the interaction strength is increased. This is further confirmed from the Landau fan diagram which is the plot of the Hall conductivity with respect to the flux passing per plaquette and the number of particles per unit cell. In the Landau fan diagram for the non-interacting case, the Hall conductivities with same values can be joined by a straight line which converges to an integer. The slopes of these lines give the topological invariant related to the Hall conductivity and the intercept is the other topological invariant which together satisfy the Diophantine equation. In the presence of interactions, it is not possible to join the points with the same Hall conductivities in a straight line as the Hall conductivities are scattered. Thus, the Landau fan diagram for

Chapter 6. Summary and Conclusion

the interacting case also signals that the fractal structure of the Hofstadter butterfly disintegrates. On using the same Diophantine equation as for the non-interacting case, we see that s_r becomes a fraction. Hence, this Diophantine equation used for the non-interacting case is not valid for the interacting case.

We also propose a method to probe the Berry curvature in the optical lattice system. The confining trap breaks particle-hole symmetry and makes the PB curvatures of the bands observable. We have shown that the effect of this is seen in the rotation of the expanding cloud when the trap is removed. For realistic atomic and trap parameters, we have shown that this provides a clear signal in time-of-flight experiments.

As we always consider filled bands with Fermi energy lying in a gap, hence mean field theory is a good approximation. It will be interesting to see whether the complex phases, we find in presence of interactions, survive if we include mean field fluctuations. Solving this interacting problem by exact diagonalization will be a next step to this problem.

Chapter 6. Summary and Conclusion

Appendix A

Dipole moment and Quadrupole moment under the rotational and inversion operators

Under inversion symmetry transformation

$$\hat{\mathcal{I}}^\dagger \hat{P}^\mu \hat{\mathcal{I}} = -\hat{P}^\mu$$

and

$$\hat{\mathcal{I}}^\dagger \hat{Q}^{\mu\nu} \hat{\mathcal{I}} = \hat{Q}^{\mu\nu}$$

. In the presence of inversion symmetry, $\hat{\mathcal{I}}|\Psi\rangle = |\Psi\rangle$ where $|\Psi\rangle$ is the many body ground state. Hence, $\langle \Psi | \hat{\mathcal{I}}^\dagger \hat{P}^\mu \hat{\mathcal{I}} | \Psi \rangle = -\langle \Psi | \hat{P}^\mu | \Psi \rangle$ and thus, the dipole moment is zero in the presence of inversion symmetry. Similarly, we can see that the quadrupole moment is unaffected by the inversion symmetry transformation since $\langle \Psi | \hat{\mathcal{I}}^\dagger \hat{Q}^{\mu\nu} \hat{\mathcal{I}} | \Psi \rangle = \langle \Psi | \hat{Q}^{\mu\nu} | \Psi \rangle$.

Under the rotational symmetry transformation

$$R_3^\dagger \hat{P}^\mu R_3 = T^{\mu\nu} (2\pi/3) \hat{P}^\nu$$

Chapter A. Dipole moment and Quadrupole moment under the rotational and inversion operators

and

$$R_3^\dagger \hat{Q}^{\mu\nu} R_3 = \hat{T}^{\mu\mu'}(2\pi/3) T^{\nu\nu'}(2\pi/3) Q^{\mu'\nu'}$$

. where $T^{\mu\nu}(2\pi/3)$ are the components of a rotation matrix,

$$T(2\pi/3) = \begin{pmatrix} -1/2 & \sqrt{3}/2 \\ \sqrt{3}/2 & 1/2 \end{pmatrix}.$$

Under preserved 3-fold rotational symmetry, $R_3|\Psi\rangle = |\Psi\rangle$. Hence, in the presence of rotational symmetry, $\langle \Psi | R_3^\dagger \hat{P}^\mu R_3 | \Psi \rangle = T^{\mu\nu}(2\pi/3) \langle \Psi | \hat{P}^\nu | \Psi \rangle$. So,

$$\langle \Psi | R_3^\dagger \hat{P}^x R_3 | \Psi \rangle = \langle \Psi | \left(\frac{-1}{2} \hat{P}^x + \frac{\sqrt{3}}{2} P^y \right) | \Psi \rangle \quad (\text{A.1})$$

$$\langle \Psi | R_3^\dagger \hat{P}^y R_3 | \Psi \rangle = \langle \Psi | \left(\frac{1}{2} \hat{P}^y + \frac{\sqrt{3}}{2} P^x \right) | \Psi \rangle \quad (\text{A.2})$$

Similarly, $\langle \Psi | R_3^\dagger \hat{P}^\mu R_3 | \Psi \rangle = T^{\mu\nu}(4\pi/3) \langle \Psi | \hat{P}^\nu | \Psi \rangle$ and hence,

$$\langle \Psi | R_3^\dagger \hat{P}^x R_3 | \Psi \rangle = \langle \Psi | \left(\frac{-1}{2} \hat{P}^x + \frac{-\sqrt{3}}{2} P^y \right) | \Psi \rangle, \quad (\text{A.3})$$

$$\langle \Psi | R_3^\dagger \hat{P}^y R_3 | \Psi \rangle = \langle \Psi | \left(\frac{1}{2} \hat{P}^y + \frac{-\sqrt{3}}{2} P^x \right) | \Psi \rangle. \quad (\text{A.4})$$

Subtracting Eq. (A.1) and (A.3), we get $\langle \Psi | \hat{P}^x | \Psi \rangle = 0$ and thus from Eq. (A.1) $\langle \Psi | \hat{P}^y | \Psi \rangle = 0$ and thus the dipole moment is zero in the presence of rotational symmetry.

Chapter A. Dipole moment and Quadrupole moment under the rotational and inversion operators

Similarly, in presence of rotational symmetry,

$$\langle \Psi | R_3^\dagger \hat{Q}^{\mu\nu} R_3 | \Psi \rangle = T^{\mu\mu'}(2\pi/3) T^{\nu\nu'}(2\pi/3) \langle \Psi | Q^{\mu'\nu'} | \Psi \rangle, \quad (\text{A.5})$$

$$\langle \Psi | R_3^\dagger \hat{Q}^{\mu\nu} R_3 | \Psi \rangle = T^{\mu\mu'}(4\pi/3) T^{\nu\nu'}(4\pi/3) \langle \Psi | Q^{\mu'\nu'} | \Psi \rangle \quad (\text{A.6})$$

$$\text{and} \langle \Psi | R_3^\dagger \hat{Q}^{\mu\nu} R_3 | \Psi \rangle = T^{\mu\mu'}(4\pi/3) T^{\nu\nu'}(4\pi/3) \langle \Psi | Q^{\mu'\nu'} | \Psi \rangle. \quad (\text{A.7})$$

$$(\text{A.8})$$

From these equations, we can see that $\langle \Psi | \hat{Q}^{xx} | \Psi \rangle = 0 = \langle \Psi | \hat{Q}^{xy} | \Psi \rangle = \langle \Psi | \hat{Q}^{yy} | \Psi \rangle$.

Hence, $Q^{\mu\nu}$ can be non-zero only if the 3-fold rotational symmetry is broken and P^μ can be non-zero only if both, the 3-fold rotational and inversion symmetries are broken.

Chapter A. Dipole moment and Quadrupole moment under the rotational and inversion operators

Appendix B

Proof of relation between quantum metric and pair correlation function

Here we prove the connection between the quantum metric and the pair correlation function given in Eq. (3.13) in previous section.

The quantum metric has been identified with the localization tensor [24, 29, 85] by studying the ground state properties of a system described by an electronic Hamiltonian with an infinitesimal twist or flux term. The metric has been defined as

$$g^{\mu\nu} = \langle \hat{R}^\mu \hat{R}^\nu \rangle - \langle \hat{R}^\mu \rangle \langle \hat{R}^\nu \rangle \quad (\text{B.1})$$

$$\begin{aligned} &= \frac{1}{L^2} \sum_{I,\alpha,a,J,\beta,b} [\langle R_{I\alpha a}^\mu c_{I\alpha a}^\dagger c_{I\alpha a} R_{J\beta b}^\nu c_{J\beta b}^\dagger c_{J\beta b} \rangle \\ &\quad - \langle R_{I\alpha a}^\mu c_{I\alpha a}^\dagger c_{I\alpha a} \rangle \langle R_{J\beta b}^\nu c_{J\beta b}^\dagger c_{J\beta b} \rangle] \end{aligned} \quad (\text{B.2})$$

where $\hat{R}^\mu = \sum_{I,\alpha,a} R_{I\alpha a}^\mu c_{I\alpha a}^\dagger c_{I\alpha a}$. From here onwards, we denote position α, a together as C and β, b together as D for convenience. Let us define the connected part of the

density-density correlation function by $\mathcal{G}_{CD}(\mathbf{R}_I, \mathbf{R}_J)$,

$$\begin{aligned}
 \mathcal{G}_{CD}(\mathbf{R}_I, \mathbf{R}_J) &\equiv \langle \rho_{IC} \rho_{JD} \rangle - \langle \rho_{IC} \rangle \langle \rho_{JD} \rangle \equiv \langle c_{IC}^\dagger c_{IC} c_{JD}^\dagger c_{JD} \rangle - \langle \rho_{IC} \rangle \langle \rho_{JD} \rangle \\
 &\equiv \langle c_{IC}^\dagger c_{JD} \rangle \delta_{CD} \delta(\mathbf{R}_I - \mathbf{R}_J) + \langle c_{IC}^\dagger c_{JD}^\dagger c_{JD} c_{IC} \rangle - \langle \rho_{IC} \rangle \langle \rho_{JD} \rangle \\
 &\equiv \langle c_{IC}^\dagger c_{JD} \rangle \delta_{CD} \delta(\mathbf{R}_I - \mathbf{R}_J) + \Gamma_{CD}(\mathbf{R}_I - \mathbf{R}_J) - \langle \rho_{IC} \rangle \langle \rho_{JD} \rangle \\
 &\equiv \langle c_{IC}^\dagger c_{JD} \rangle \delta_{CD} \delta(\mathbf{R}_I - \mathbf{R}_J) - S_{CD}(\mathbf{R}_I - \mathbf{R}_J). \tag{B.3}
 \end{aligned}$$

The average metric can then be written as

$$\begin{aligned}
 \bar{g}^{\mu\nu} &= \frac{1}{L^2} \sum_{ICJD} R_{IC}^\mu R_{JD}^\nu \mathcal{G}_{CD}(\mathbf{R}_I, \mathbf{R}_J) \tag{B.4} \\
 &= \frac{1}{L^2} \sum_{ICJD} R_{IC}^\mu R_{JD}^\nu \langle c_{IC}^\dagger c_{JD} \rangle \delta_{CD} \delta(\mathbf{R}_I - \mathbf{R}_J) \\
 &\quad - \frac{1}{L^2} \sum_{ICJD} R_{IC}^\mu R_{JD}^\nu S_{CD}(\mathbf{R}_I - \mathbf{R}_J) \\
 &= \frac{1}{L^2} \sum_{IC} R_{IC}^\mu R_{IC}^\nu \rho_{IC} - \frac{1}{L^2} \sum_{ICJD} R_{IC}^\mu R_{JD}^\nu S_{CD}(\mathbf{R}_I - \mathbf{R}_J), \tag{B.5}
 \end{aligned}$$

where ρ_{IC} is the single particle density at position \mathbf{R}_{IC} . Considering second term in Eq. (B.5)

$$\begin{aligned}
 &\sum_{ICJD} R_{IC}^\mu R_{JD}^\nu S_{CD}(\mathbf{R}_I - \mathbf{R}_J) \\
 &= \frac{-1}{2} \sum_{ICJD} (R_{IC}^\mu - R_{JD}^\mu)(R_{IC}^\nu - R_{JD}^\nu) S_{CD}(\mathbf{R}_I - \mathbf{R}_J) \\
 &\quad + \frac{1}{2} \sum_{ICJD} (R_{IC}^\mu R_{IC}^\nu + R_{JD}^\mu R_{JD}^\nu) S_{CD}(\mathbf{R}_I - \mathbf{R}_J). \tag{B.6}
 \end{aligned}$$

Interchanging $I \longleftrightarrow J$ and $C \longleftrightarrow D$ simultaneously in $S_{CD}(\mathbf{R}_I - \mathbf{R}_J)$.

$$S_{DC}(\mathbf{R}_J - \mathbf{R}_I) = S_{CD}(\mathbf{R}_I - \mathbf{R}_J) \tag{B.7}$$

Chapter B. Proof of relation between quantum metric and pair correlation function

So we can write the second term in Eq. (B.6) as

$$\begin{aligned}
& \frac{1}{2} \sum_{ICJD} (R_{IC}^\mu R_{IC}^\nu + R_{JD}^\mu R_{JD}^\nu) S_{CD} (\mathbf{R}_I - \mathbf{R}_J) \\
&= \sum_{ICJD} R_{IC}^\mu R_{IC}^\nu S_{CD} (\mathbf{R}_I - \mathbf{R}_J) \\
&= - \sum_{ICJD} R_{IC}^\mu R_{IC}^\nu [\langle c_{IC}^\dagger c_{JD}^\dagger c_{JD} c_{IC} \rangle - \langle \rho_{IC} \rangle \langle \rho_{JD} \rangle]. \tag{B.8}
\end{aligned}$$

$\sum_{JD} c_{JD}^\dagger c_{JD} = \sum_{JD} \rho_{JD} = \hat{N}$ and $\langle \hat{N} \rangle = N$ where N is the total number of particles on the lattice. Hence,

$$\sum_{JD} \langle c_{IC}^\dagger c_{JD}^\dagger c_{JD} c_{IC} \rangle = \langle c_{IC}^\dagger \hat{N} c_{IC} \rangle = \langle c_{IC}^\dagger [\hat{N}, c_{IC}] \rangle + \langle c_{IC}^\dagger c_{IC} \hat{N} \rangle \tag{B.9}$$

As $[\hat{N}, c_{IC}] = -c_{IC}$, therefore,

$$\sum_{ICJD} \langle c_{IC}^\dagger c_{JD}^\dagger c_{JD} c_{IC} \rangle = - \sum_{IC} \langle c_{IC}^\dagger c_{IC} \rangle + \sum_{ICJD} \langle \rho_{IC} \rangle \langle \rho_{ID} \rangle \tag{B.10}$$

Using Eq. (B.10) in Eq. (B.8),

$$\begin{aligned}
\sum_{ICJD} R_{IC}^\mu R_{IC}^\nu S_{CD} (\mathbf{R}_I - \mathbf{R}_J) &= \sum_{IC} R_{IC}^\mu R_{IC}^\nu \langle c_{IC}^\dagger c_{IC} \rangle \\
&= \sum_{IC} R_{IC}^\mu R_{IC}^\nu \langle \rho_{IC} \rangle \tag{B.11}
\end{aligned}$$

So, using Eq. (B.11) in Eq. (B.6),

$$\begin{aligned}
& \sum_{ICJD} R_{IC}^\mu R_{JD}^\nu S_{CD} (\mathbf{R}_I - \mathbf{R}_J) \\
&= \sum_{ICJD} \frac{-1}{2} (R_{IC}^\mu - R_{JD}^\mu) (R_{IC}^\nu - R_{JD}^\nu) S_{CD} (\mathbf{R}_I - \mathbf{R}_J) + \sum_{IC} R_{IC}^\mu R_{IC}^\nu \rho_{IC}
\end{aligned}$$

and hence Eq. (B.5) is

$$\begin{aligned}\bar{g}^{\mu\nu} &= \frac{1}{L^2} \frac{1}{2} \sum_{ICJD} (R_{IC}^\mu - R_{JD}^\mu)(R_{IC}^\nu - R_{JD}^\nu) S_{CD}(\mathbf{R}_I - \mathbf{R}_J) \\ &= \frac{1}{L^2} \frac{1}{2} \sum_{I\alpha a\beta b} (R_{I\alpha a}^\mu - R_{J\beta b}^\mu)(R_{I\alpha a}^\nu - R_{J\beta b}^\nu) S_{\alpha a, \beta b}(\mathbf{R}_I - \mathbf{R}_J).\end{aligned}\quad (\text{B.12})$$

This relation is exact and not restricted to mean field approximation. Here L^2 gives the area of the system.

Appendix C

Chern numbers at half filling

The single particle mean field hamiltonian for the half filled case describing the CDW state is given in equation (3.10). The eigenvalue equation can be written as,

$$\begin{pmatrix} \Delta & F(\vec{k}) \\ F^\dagger(\vec{k}) & -\Delta \end{pmatrix} \begin{pmatrix} \psi_A(\vec{k}) \\ \psi_B(\vec{k}) \end{pmatrix} = E(\vec{k}) \begin{pmatrix} \psi_A(\vec{k}) \\ \psi_B(\vec{k}) \end{pmatrix} \quad (\text{C.1})$$

where $\psi_{A(B)}(\vec{k})$ are q -component column vectors. They can be constructed in terms of the spectrum of the positive, semi-definite, hermitian matrix, $F(k)F^\dagger(k)$. We denote,

$$F(\vec{k})F^\dagger(\vec{k})\chi^n(\vec{k}) = \epsilon_n^2(\vec{k})\chi^n(\vec{k}) \quad (\text{C.2})$$

where, $n = 1, \dots, q$ and we choose χ^n to be ortho-normalised. The above equation implies that the eigenvalues of $F^\dagger(\vec{k})F(\vec{k})$ are the same, since,

$$F^\dagger(\vec{k})F(\vec{k}) \left(F^\dagger(\vec{k})\chi^n(\vec{k}) \right) = \epsilon_n^2(\vec{k}) \left(F^\dagger(\vec{k})\chi^n(\vec{k}) \right) \quad (\text{C.3})$$

Further, the inversion (two fold rotation) transformation relates $F(\vec{k})$ to $F^\dagger(-\vec{k})$,

$$\mathcal{I}F(\vec{k})\mathcal{I}^\dagger = F^\dagger(-\vec{k}) \quad (\text{C.4})$$

where,

$$\mathcal{I} = \begin{pmatrix} 0 & 0 & 1 \\ 0 & 1 & 0 \\ 1 & 0 & 0 \end{pmatrix} \quad (\text{C.5})$$

consequently, we have $\epsilon_n(\vec{k}) = \epsilon_n(-\vec{k})$ and

$$F^\dagger(\vec{k})F(\vec{k}) \left(\mathcal{I}\chi^n(-\vec{k}) \right) = \epsilon_n^2(\vec{k}) \left(\mathcal{I}\chi^n(-\vec{k}) \right) \quad (\text{C.6})$$

The eigenvectors of $h_{MF}(\vec{k})$, $\psi^{\pm n}(\vec{k})$ corresponding to the eigenvalues $E_{\pm n}(\vec{k}) = \pm\sqrt{\epsilon_n^2(\vec{k}) + \Delta^2}$ are given by,

$$\psi^{+n}(\vec{k}) = \begin{pmatrix} \cos \frac{\theta_n(\vec{k})}{2} \chi^n(\vec{k}) \\ \sin \frac{\theta_n(\vec{k})}{2} \mathcal{I}\chi^n(-\vec{k}) \end{pmatrix} \quad (\text{C.7})$$

$$\psi^{-n}(\vec{k}) = \begin{pmatrix} -\sin \frac{\theta_n(\vec{k})}{2} \chi_n(\vec{k}) \\ \cos \frac{\theta_n(\vec{k})}{2} \mathcal{I}\chi^n(-\vec{k}) \end{pmatrix} \quad (\text{C.8})$$

where,

$$\cos \theta_n(\vec{k}) = \frac{\Delta}{\sqrt{\epsilon_n^2(\vec{k}) + \Delta^2}}, \quad \sin \theta_n(\vec{k}) = \frac{\epsilon_n(\vec{k})}{\sqrt{\epsilon_n^2(\vec{k}) + \Delta^2}} \quad (\text{C.9})$$

Chapter C. Chern numbers at half filling

The Pancharatnam-Berry curvatures of the negative energy bands (occupied at half filling) are given by $\mathcal{B}^{-n}(\vec{k}) = \epsilon_{ij}\partial_i\psi^{-n\dagger}(\vec{k})\partial_j\psi^{-n}(\vec{k})$. The Chern numbers are given by,

$$\begin{aligned} \nu^n &= \int_k \left(\epsilon_{ij} \sin \theta_n \partial_i \theta_n \left(\tilde{\mathcal{A}}_j^n(\vec{k}) + \tilde{\mathcal{A}}_j^n(-\vec{k}) \right) + \right. \\ &\quad \left. \epsilon_{ij} \left(\sin^2 \frac{\theta_n}{2} \tilde{\mathcal{B}}^n(\vec{k}) + \cos^2 \frac{\theta_n}{2} \tilde{\mathcal{B}}^n(-\vec{k}) \right) \right) \end{aligned} \quad (\text{C.10})$$

where the integral is over the reduced Brillouin zone, $\tilde{\mathcal{A}}_i^n(\vec{k}) \equiv -i\chi^{n\dagger}(\vec{k})\partial_i\chi^n(\vec{k})$ and $\tilde{\mathcal{B}}^n(\vec{k}) = \epsilon_{ij}\partial_i\tilde{\mathcal{A}}_j^n(\vec{k})$. Since, $\tilde{\mathcal{A}}_i^n(\vec{k}) = -\tilde{\mathcal{A}}_i^n(-\vec{k})$, $\tilde{\mathcal{B}}^n(\vec{k}) = \tilde{\mathcal{B}}^n(-\vec{k})$ and $\theta_n(\vec{k}) = \theta_n(-\vec{k})$, we get our final result,

$$\nu^n = \int_k \tilde{\mathcal{B}}^n(\vec{k}) \quad (\text{C.11})$$

Thus, since $\chi^n(\vec{k})$ is independent of Δ , so are the Chern numbers.

Chapter C. Chern numbers at half filling

Bibliography

- [1] K. v. Klitzing, G. Dorda, and M. Pepper, “New method for high-accuracy determination of the fine-structure constant based on quantized hall resistance,” *Physical Review Letters*, vol. 45, no. 6, p. 494, 1980.
- [2] D. R. Hofstadter *Physical Review B*, vol. 14, no. 6, p. 2239, 1976.
- [3] L. D. Landau and E. M. Lifshitz, *Quantum mechanics: non-relativistic theory*, vol. 3. Elsevier, 2013.
- [4] F. Bloch, “Über die quantenmechanik der elektronen in kristallgittern,” *Zeitschrift für physik*, vol. 52, no. 7-8, pp. 555–600, 1929.
- [5] C. Kittel, *Introduction to solid state physics*. Wiley, 2005.
- [6] N. W. Ashcroft and N. D. Mermin, “Solid state phys,” *Saunders, Philadelphia*, p. 293, 1976.
- [7] G. Gumbs and P. Fekete *Phys. Rev. B*, vol. 56, p. 3787, 1997.
- [8] T. Schlösser, K. Ensslin, J. Kotthaus, and M. Holland, “Internal structure of a landau band induced by a lateral superlattice: a glimpse of hofstadter’s butterfly,” *EPL (Europhysics Letters)*, vol. 33, no. 9, p. 683, 1996.
- [9] C. Albrecht, J. Smet, K. Von Klitzing, D. Weiss, V. Umansky, and H. Schweizer, “Evidence of hofstadter’s fractal energy spectrum in the quantized hall conduct-

- tance,” *Physica E: Low-dimensional Systems and Nanostructures*, vol. 20, no. 1, pp. 143–148, 2003.
- [10] M. Geisler, J. Smet, V. Umansky, K. Von Klitzing, B. Naundorf, R. Ketzmerick, and H. Schweizer, “Detection of landau band coupling induced rearrangement of the hofstadter butterfly,” *Physica E: Low-dimensional Systems and Nanostructures*, vol. 25, no. 2, pp. 227–232, 2004.
- [11] C. Dean, L. Wang, P. Maher, C. Forsythe, F. Ghahari, Y. Gao, J. Katoch, M. Ishigami, P. Moon, M. Koshino, *et al.* *Nature*, vol. 497, no. 7451, p. 598, 2013.
- [12] L. Ponomarenko, R. Gorbachev, G. Yu, D. Elias, R. Jalil, A. Patel, A. Mishchenko, A. Mayorov, C. Woods, J. Wallbank, *et al.* *Nature*, vol. 497, no. 7451, p. 594, 2013.
- [13] B. Hunt, J. Sanchez-Yamagishi, A. Young, M. Yankowitz, B. J. LeRoy, K. Watanabe, T. Taniguchi, P. Moon, M. Koshino, P. Jarillo-Herrero, *et al.* *Science*, vol. 340, no. 6139, p. 1427, 2013.
- [14] G. Yu, R. Gorbachev, J. Tu, A. Kretinin, Y. Cao, R. Jalil, F. Withers, L. Ponomarenko, B. Piot, M. Potemski, *et al.* *Nature Physics*, vol. 10, p. 784, 2014.
- [15] M. Aidelsburger, M. Atala, M. Lohse, J. Barreiro, B. Paredes, and I. Bloch *Physical Review Letters*, vol. 111, no. 18, p. 185301, 2013.
- [16] H. Miyake, G. A. Siviloglou, C. J. Kennedy, W. C. Burton, and W. Ketterle *Physical Review Letters*, vol. 111, no. 18, p. 185302, 2013.
- [17] D. Smith and C. Mailhot, “Theory of semiconductor superlattice electronic structure,” *Reviews of Modern Physics*, vol. 62, no. 1, p. 173, 1990.

- [18] G. Yu, R. Gorbachev, J. Tu, A. Kretinin, Y. Cao, R. Jalil, F. Withers, L. Ponomarenko, B. Piot, M. Potemski, *et al.*, “Hierarchy of hofstadter states and replica quantum hall ferromagnetism in graphene superlattices,” *Nature physics*, 2014.
- [19] E. V. Castro, A. G. Grushin, B. Valenzuela, M. A. Vozmediano, A. Cortijo, and F. de Juan, “Topological fermi liquids from coulomb interactions in the doped honeycomb lattice,” *Physical review letters*, vol. 107, no. 10, p. 106402, 2011.
- [20] A. G. Grushin, E. V. Castro, A. Cortijo, F. de Juan, M. A. Vozmediano, and B. Valenzuela *Physical Review B*, vol. 87, no. 8, p. 085136, 2013.
- [21] F. D. M. Haldane, “Model for a quantum hall effect without landau levels: Condensed-matter realization of the "parity anomaly",” *Phys. Rev. Lett.*, vol. 61, pp. 2015–2018, Oct 1988.
- [22] F. Haldane *Physical Review Letters*, vol. 93, no. 20, p. 206602, 2004.
- [23] F. D. M. Haldane, “Topology and geometry in quantum condensed matter,” 2012. PCCM/PCTS Summer School, July 23-26,2012.
- [24] R. Resta *The European Physical Journal B-Condensed Matter and Complex Systems*, vol. 79, no. 2, p. 121, 2011.
- [25] N. Mukunda and R. Simon *Annals of Physics*, vol. 228, no. 2, p. 205, 1993.
- [26] V. Bargmann, “Note on wigner’s theorem on symmetry operations,” *Journal of Mathematical Physics*, vol. 5, no. 7, pp. 862–868, 1964.
- [27] F. D. M. Haldane, “Quantum geometry in conducting systems,” 2006. Slides of a talk given at the PITP-Les Houches Summer School, Quantum Magnetism, June 6-23, 2006.

BIBLIOGRAPHY

BIBLIOGRAPHY

- [28] F. D. M. Haldane, "Berry's phase and the quantum geometry of the fermi sea," 2005. Slides of a talk given at the joint session of the "Showcase" conference and "Emergence" workshop at the Pacific Institute for Theoretical Physics, University of British Columbia, Vancouver, Canada, May 11-16 and May 15-18, 2005.
- [29] R. Resta, "Geometry and topology in electronic structure theory," 2015.
- [30] G. Sundaram and Q. Niu *Physical Review B*, vol. 59, no. 23, p. 14915, 1999.
- [31] D. Thouless, M. Kohmoto, M. Nightingale, and M. Den Nijs *Physical Review Letters*, vol. 49, p. 405, 1982.
- [32] M. Kohmoto *Annals of Physics*, vol. 160, no. 2, p. 343, 1985.
- [33] Q. Niu, D. J. Thouless, and Y.-S. Wu *Physical Review B*, vol. 31, no. 6, p. 3372, 1985.
- [34] R. Roy *Physical Review B*, vol. 79, no. 19, p. 195321, 2009.
- [35] N. Marzari and D. Vanderbilt *Physical Review B*, vol. 56, no. 20, p. 12847, 1997.
- [36] Y.-S. Wu, Y. Hatsugai, and M. Kohmoto, "Gauge invariance of fractionally charged quasiparticles and hidden topological z_n symmetry," *Phys. Rev. Lett.*, vol. 66, pp. 659–662, Feb 1991.
- [37] C. L. Kane and E. J. Mele, "Z₋ {2} topological order and the quantum spin hall effect," *Physical review letters*, vol. 95, no. 14, p. 146802, 2005.
- [38] M. Ezawa, Y. Tanaka, and N. Nagaosa, "Topological phase transition without gap closing," *Scientific reports*, vol. 3, 2013.
- [39] S. Rachel, "Quantum phase transitions of topological insulators with and without gap closing," *arXiv preprint arXiv:1310.3159*, 2013.

- [40] K. Sun, H. Yao, E. Fradkin, and S. A. Kivelson, “Topological insulators and nematic phases from spontaneous symmetry breaking in 2d fermi systems with a quadratic band crossing,” *Physical review letters*, vol. 103, no. 4, p. 046811, 2009.
- [41] A. Amaricci, J. Budich, M. Capone, B. Trauzettel, and G. Sangiovanni, “First-order character and observable signatures of topological quantum phase transitions,” *Physical review letters*, vol. 114, no. 18, p. 185701, 2015.
- [42] A. M. Pruisken, “Field theory, scaling and the localization problem,” in *The Quantum Hall Effect*, pp. 117–173, Springer, 1987.
- [43] A. Koulakov, M. Fogler, and B. Shklovskii, “Charge density wave in two-dimensional electron liquid in weak magnetic field,” *Physical Review Letters*, vol. 76, no. 3, p. 499, 1996.
- [44] F. Haldane, “Geometrical description of the fractional quantum hall effect,” *Physical Review Letters*, vol. 107, no. 11, p. 116801, 2011.
- [45] Y. You, G. Y. Cho, and E. Fradkin, “Theory of nematic fractional quantum hall states,” *Physical Review X*, vol. 4, no. 4, p. 041050, 2014.
- [46] J. Maciejko, B. Hsu, S. Kivelson, Y. Park, and S. Sondhi, “Field theory of the quantum hall nematic transition,” *Physical Review B*, vol. 88, no. 12, p. 125137, 2013.
- [47] M. Lilly, K. Cooper, J. Eisenstein, L. Pfeiffer, and K. West, “Evidence for an anisotropic state of two-dimensional electrons in high landau levels,” *Physical Review Letters*, vol. 82, no. 2, p. 394, 1999.
- [48] J. Xia, J. Eisenstein, L. Pfeiffer, and K. West, “Evidence for a fractionally quantized hall state with anisotropic longitudinal transport,” *Nature Physics*, vol. 7, no. 11, pp. 845–848, 2011.

BIBLIOGRAPHY

BIBLIOGRAPHY

- [49] Y. Liu, S. Hasdemir, M. Shayegan, L. Pfeiffer, K. West, and K. Baldwin, “Evidence for a $\nu = 5/2$ fractional quantum hall nematic state in parallel magnetic fields,” *Physical Review B*, vol. 88, no. 3, p. 035307, 2013.
- [50] M. Fogler, A. Koulakov, and B. Shklovskii, “Ground state of a two-dimensional electron liquid in a weak magnetic field,” *Physical Review B*, vol. 54, no. 3, p. 1853, 1996.
- [51] E. Fradkin and S. A. Kivelson, “Liquid-crystal phases of quantum hall systems,” *Physical Review B*, vol. 59, no. 12, p. 8065, 1999.
- [52] R. Moessner and J. Chalker, “Exact results for interacting electrons in high landau levels,” *Physical Review B*, vol. 54, no. 7, p. 5006, 1996.
- [53] E. Fradkin, S. A. Kivelson, M. J. Lawler, J. P. Eisenstein, and A. P. Mackenzie, “Nematic fermi fluids in condensed matter physics,” *arXiv preprint arXiv:0910.4166*, 2009.
- [54] C. Weeks and M. Franz, “Interaction-driven instabilities of a dirac semimetal,” *Physical Review B*, vol. 81, no. 8, p. 085105, 2010.
- [55] V. Gudmundsson and R. R. Gerhardts, “Effects of screening on the hofstadter butterfly,” *Physical Review B*, vol. 52, no. 23, p. 16744, 1995.
- [56] H. Doh and S.-H. S. Salk, “Effects of electron correlations on the hofstadter spectrum,” *Physical Review B*, vol. 57, pp. 1312–1315, Jan 1998.
- [57] K. Czajka, A. Gorczyca, M. M. Maśka, and M. Mierzejewski, “Hofstadter butterfly for a finite correlated system,” *Physical Review B*, vol. 74, no. 12, p. 125116, 2006.
- [58] I. F. Herbut, “Theory of integer quantum hall effect in graphene,” *Physical Review B*, vol. 75, no. 16, p. 165411, 2007.

- [59] B. Roy and I. F. Herbut, “Inhomogeneous magnetic catalysis on graphene’s hon-eycomb lattice,” *Physical Review B*, vol. 83, no. 19, p. 195422, 2011.
- [60] T. Chakraborty and V. M. Apalkov, “Traits and characteristics of interacting dirac fermions in monolayer and bilayer graphene,” *Solid State Communications*, vol. 175, pp. 123–131, 2013.
- [61] V. M. Apalkov and T. Chakraborty, “Gap structure of the hofstadter system of interacting dirac fermions in graphene,” *Physical Review Letters*, vol. 112, no. 17, p. 176401, 2014.
- [62] F. H. Claro and G. H. Wannier *Phys. Rev. B*, vol. 19, p. 6068, 1979.
- [63] Y. Hasegawa, Y. Hatsugai, M. Kohmoto, and G. Montambaux *Phys. Rev. B*, vol. 41, p. 9174, 1990.
- [64] Y. Hatsugai, T. Fukui, and H. Aoki *Phys. Rev. B*, vol. 74, p. 205414, 2006.
- [65] J. Zak, “Magnetic translation group,” *Physical Review*, vol. 134, no. 6A, p. A1602, 1964.
- [66] J.-W. Rhim and K. Park, “Self-similar occurrence of massless dirac particles in graphene under a magnetic field,” *Physical Review B*, vol. 86, no. 23, p. 235411, 2012.
- [67] H. Aoki and T. Ando, “Effect of localization on the hall conductivity in the two-dimensional system in strong magnetic fields,” *Solid State Communications*, vol. 38, no. 11, pp. 1079–1082, 1981.
- [68] P. Streda, “Theory of quantised hall conductivity in two dimensions,” *Journal of Physics C: Solid State Physics*, vol. 15, no. 22, p. L717, 1982.

BIBLIOGRAPHY

BIBLIOGRAPHY

- [69] D. Xiao, M.-C. Chang, and Q. Niu, “Berry phase effects on electronic properties,” *Reviews of modern physics*, vol. 82, no. 3, p. 1959, 2010.
- [70] S. Pancharatnam, “Generalized theory of interference and its applications,” in *Proceedings of the Indian Academy of Sciences-Section A*, vol. 44, pp. 398–417, Springer, 1956.
- [71] M. V. Berry, “Quantal phase factors accompanying adiabatic changes,” in *Proceedings of the Royal Society of London A: Mathematical, Physical and Engineering Sciences*, vol. 392, pp. 45–57, The Royal Society, 1984.
- [72] T. Fukui, Y. Hatsugai, and H. Suzuki, “Chern numbers in discretized brillouin zone: Efficient method of computing (spin) hall conductances,” *Journal of the Physical Society of Japan*, vol. 74, no. 6, pp. 1674–1677, 2005.
- [73] R. Resta, “Polarization fluctuations in insulators and metals: new and old theories merge,” *Physical review letters*, vol. 96, no. 13, p. 137601, 2006.
- [74] N. Goldman, “Characterizing the hofstadter butterfly’s outline with chern numbers,” *Journal of Physics B: Atomic, Molecular and Optical Physics*, vol. 42, no. 5, p. 055302, 2009.
- [75] A. Agazzi, J.-P. Eckmann, and G. M. Graf, “The colored hofstadter butterfly for the honeycomb lattice,” *Journal of Statistical Physics*, vol. 156, no. 3, pp. 417–426, 2014.
- [76] A. H. MacDonald, “Landau-level subband structure of electrons on a square lattice,” *Physical Review B*, vol. 28, pp. 6713–6717, Dec 1983.
- [77] H. M. Price and N. R. Cooper, “Mapping the berry curvature from semiclassical dynamics in optical lattices,” *Phys. Rev. A*, vol. 85, no. 3, p. 033620, 2012.

- [78] M. Atala, M. Aidelsburger, J. T. Barreiro, D. Abanin, T. Kitagawa, E. Demler, and I. Bloch, “Direct measurement of the zak phase in topological bloch bands,” *Nature Physics*, vol. 9, no. 12, pp. 795–800, 2013.
- [79] L. Wang, A. A. Soluyanov, and M. Troyer, “Proposal for direct measurement of topological invariants in optical lattices,” *Physical review letters*, vol. 110, no. 16, p. 166802, 2013.
- [80] S. Hassan, P. Sriluckshmy, S. K. Goyal, R. Shankar, and D. Sénéchal, “Stable algebraic spin liquid in a hubbard model,” *Physical review letters*, vol. 110, no. 3, p. 037201, 2013.
- [81] P. Sriluckshmy, A. Mishra, S. Hassan, and R. Shankar *Physical Review B*, vol. 89, no. 4, p. 045105, 2014.
- [82] L. M. Duan, E. Demler, and M. D. Lukin, “Controlling spin exchange interactions of ultracold atoms in optical lattices,” *Phys. Rev. Lett.*, vol. 91, no. 9, p. 090402, 2003.
- [83] T. Uehlinger, D. Greif, G. Jotzu, L. Tarruell, T. Esslinger, L. Wang, and M. Troyer, “Double transfer through dirac points in a tunable honeycomb optical lattice,” *The European Physical Journal Special Topics*, vol. 217, no. 1, pp. 121–133, 2013.
- [84] F. Chevy, K. W. Madison, and J. Dalibard, “Measurement of the angular momentum of a rotating bose-einstein condensate,” *Phys. Rev. Lett.*, vol. 85, no. 11, pp. 2223–2227, 2000.
- [85] R. Resta and S. Sorella, “Electron localization in the insulating state,” *Physical Review Letters*, vol. 82, no. 2, p. 370, 1999.